GANIL

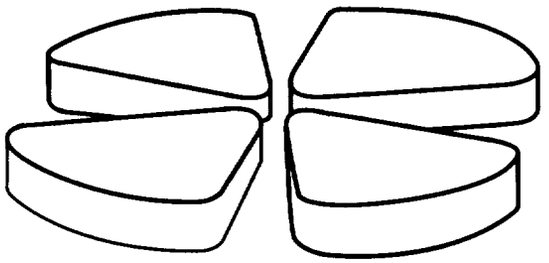

HARD PHOTONS AND NEUTRAL PIONS AS PROBES OF HOT AND DENSE NUCLEAR MATTER

Y. Schutz [a], G. Martínez [a], F.M. Marqués [a,2], A. Marín [b], T. Matulewicz [a,3], R.W. Ostendorf [c], P. Bożek [a,4], H. Delagrange [a], J. Díaz [b], M. Franke [d], K.K. Gudima [a,5], S. Hlaváč [e,6], R. Holzmann [e], P. Lautridou [a,7], F. Lefèvre [a,7], H. Löhner [c], W. Mittig [a], M. Płoszajczak [a], J.H.G. van Pol [c,8], J. Québert [f], P. Roussel-Chomaz [a], A. Schubert [e,9], R.H. Siemssen [c], R.S. Simon [e], Z. Sujkowski [g], V.D. Toneev [a,10], V. Wagner [h], H.W. Wilschut [c], and Gy. Wolf [e]

[a] *Grand Accélérateur National d'Ions Lourds, BP 5027, 14021 Caen, France*

[b] *Instituto de Física Corpuscular (CSIC - Universidad de Valencia), 46100 Burjassot, Spain*

[c] *Kernfysisch Versneller Instituut, 9747 AA Groningen, The Netherlands*

[d] *II Physikalisches Institut Universität Gießen, D-35392 Gießen, Germany*

[e] *Gesellschaft für Schwerionenforschung, D-64291 Darmstadt, Germany*

[f] *Centre d'Etudes Nucléaires de Bordeaux-Gradignan, 33175 Gradignan, France*

[g] *Soltan Institute for Nuclear Studies, 05-400 Swierk, Poland*

[h] *Nuclear Physics Institute, 250 68 Řež, Czech Republic*

GANIL P 97 15

Accepté pour publication dans Nuclear Physics A

HARD PHOTONS AND NEUTRAL PIONS AS PROBES OF HOT AND DENSE NUCLEAR MATTER

Y. Schutz [a], G. Martínez [a], F.M. Marqués [a,2], A. Marín [b], T. Matulewicz [a,3], R.W. Ostendorf [c], P. Bożek [a,4], H. Delagrange [a], J. Díaz [b], M. Franke [d], K.K. Gudima [a,5], S. Hlaváč [e,6], R. Holzmann [e], P. Lautridou [a,7], F. Lefèvre [a,7], H. Löhner [c], W. Mittig [a], M. Płoszajczak [a], J.H.G. van Pol [c,8], J. Québert [f], P. Roussel-Chomaz [a], A. Schubert [e,9], R.H. Siemssen [c], R.S. Simon [e], Z. Sujkowski [g], V.D. Toneev [a,10], V. Wagner [h], H.W. Wilschut [c], and Gy. Wolf [e]

[a] *Grand Accélérateur National d'Ions Lourds, BP 5027, 14021 Caen, France*

[b] *Instituto de Física Corpuscular (CSIC - Universidad de Valencia), 46100 Burjassot, Spain*

[c] *Kernfysisch Versneller Instituut, 9747 AA Groningen, The Netherlands*

[d] *II Physikalisches Institut Universität Gießen, D-35392 Gießen, Germany*

[e] *Gesellschaft für Schwerionenforschung, D-64291 Darmstadt, Germany*

[f] *Centre d'Etudes Nucléaires de Bordeaux-Gradignan, 33175 Gradignan, France*

[g] *Soltan Institute for Nuclear Studies, 05-400 Swierk, Poland*

[h] *Nuclear Physics Institute, 250 68 Řež, Czech Republic*

Abstract

The dynamics of heavy-ion collisions is studied in an energy domain in the vicinity of the Fermi energy. The early history of the collision is analyzed from the theoretical and experimentally point of view in which the message conveyed by bremsstrahlung photons and neutral pions is exploited. The Boltzmann-Uehling-Uhlenbeck model and the Dubna-Cascade-Model, both based on similar principles but each adopting different computation technics, are briefly described and their respective predictions are discussed. In particular the emission pattern of bremsstrahlung photons is discussed. The photon production has been measured in the systems ^{86}Kr + ^{58}Ni at 60A MeV, ^{181}Ta + ^{197}Au at 40A MeV and ^{208}Pb + ^{197}Au at 30A MeV and energy spectra, angular distributions and two-photon correlations have been analyzed. We find that bremsstrahlung photons are emitted from two distinct sources that can be correlated with nuclear-matter density oscillations. The properties of photon emission are discussed in terms of collective properties of nuclear matter. The high energy tail of the photon spectrum is interpreted by π^0 and Δ decay but predominantly by radiative capture of pions. The π^0 absorption in the nuclear medium is further analyzed by examining their emission pattern.

Contents

[1] Experiments performed with TAPS at the GANIL facility, Caen, France.
[2] Present address: Laboratoire de Physique Corpusculaire, F-14050 Caen, France.
[3] Permanent address: Warsaw University, PL-00-681, Warszawa, Poland.
[4] Permanent address : Institute of Nuclear Physics, Kraków, Poland.
[5] Permanent address : Institute of Applied Physics, Kishinev, Moldavie.
[6] Permanent address: Slovak Academy of Sciences, Bratislava, Slovakia.
[7] Permanent address: SUBATECH, F-44070, Nantes, France.
[8] Present address: KPN Research, Leidschendam, The Netherlands
[9] Permanent address: Institute for Transuranium Elements, D-76125 Karlsruhe, Germany.
[10] Permanent address : Bogoliubov Laboratory of Theoretical Physics, Dubna, Russia.

1 INTRODUCTION

The derivation of the Equation-of-State (EOS) of nuclear matter is one of the foremost challenges of modern heavy-ion physics. Since heavy-ion collisions provide up to now the only means to form and investigate hot and dense nuclear matter in the laboratory, much experimental and theoretical effort is being directed towards their study [1]. In the course of the collision nuclear matter passes through a succession of fleetingly short-lived states of nuclear matter and therefore heavy-ion collisions offer the promise to sample *dynamically* the nuclear-matter phase-diagram. Changing the projectile kinetic energy modifies the domain of the phase-diagram that is explored and thus, in principle, permits one to select the specific properties one wishes to study, as for example the possible liquid- (normal nuclear matter) gas phase transition or the transition from hadronic matter towards a quark-gluon plasma. However, the dynamic aspects of the collisions also introduce a major complication of such studies as these will not only reflect the properties of nuclear matter but also the dynamic features of the reactions. The analysis will therefore be model dependent.

Because of their relatively high emission rates, nucleons, mesons (at energies above threshold), light ions and intermediate mass fragments, produced and emitted in the reactions, are conveniently used to obtain information on the reaction dynamics at intermediate and relativistic energies. Any of the mentioned probes faces, however, the drawback that its production source cannot be well localized in space and time since the emission can take place throughout the collision. Moreover, these particles interact strongly with the nuclear medium such that the information they convey only provides a blurred image of their source. In order to be able to extract any information on the properties of nuclear matter it is therefore mandatory to separate effects related to the collision dynamics from those linked to the EOS. Sophisticated theoretical models are hence required [2]. In these, however, uncertainties in ill–defined quantities, as e.g. the in-medium nucleon-nucleon cross section, can lead to effects of the same magnitude as those expected from the thermodynamic properties of nuclear matter.

Energetic photons offer an attractive alternative to the hadronic probes. Photons interacting only weakly through the electromagnetic force with the nuclear medium are not subjected to distortions by the final state interactions. They therefore deliver an undistorted picture of the emitting source. At intermediate bombarding energies hard photons, conventionally defined as γ–rays with energies above 20–30 MeV, are mainly produced via the bremsstrahlung mechanism in individual proton-neutron collisions [3,4]. Moreover, they are produced at an early stage of the heavy-ion reaction in first chance collisions when the nuclear density is the highest [4]. They thus provide an undisturbed

snapshot of the initial stage of the reaction.

It was the main motivation for the construction of new detectors with unprecedented performance to be able to fully exploit the richness of information carried by photons. The *Two Arm Photon Spectrometer*, abbreviated TAPS, is such a detector for hard photons. It was designed and constructed, and is presently operated by an European collaboration of laboratories from France (GANIL), Germany (GSI, University of Gießen), The Netherlands (KVI), Spain (University of Valencia) and the Czech Republic (NPI, Řež). In addition, groups from many other institutes joined the collaboration for specific experiments or programs. Because of its modularity, TAPS is particularly adapted to be moved from one laboratory to the other. This has made a rich, diverse and complementary research program possible that covers many different facets of nuclear physics [5].

We report in the present article on experiments performed at the GANIL facility in 1992. The main goal was to investigate the details of bremsstrahlung photon emission in heavy-ion collisions. We have studied the systems ^{86}Kr + ^{58}Ni at 60A MeV, ^{181}Ta + ^{197}Au at 40A MeV and ^{208}Pb + ^{197}Au at 30A MeV. Partial results have already been published [6–12].

The article is organized as follows. In § 2 we consider the theoretical aspects of heavy-ion collisions in general, and the associated photon production in particular. Two models based on the Boltzmann transport equation, in light of which we will discuss the experimental results, are briefly presented in the appendix (§ 12). Predictions on collision dynamics and photon production are presented and discussed in terms of collective properties of nuclear matter. In § 3 the experimental arrangement is presented with a description of the three detector components: TAPS, the magnetic spectrometer SPEG, and the charged particle hodoscope KVI-FW. The data analysis and the identification of photons, neutral pions, charged particles and projectile-like fragments are discussed in § 4. The event identification as a function of impact parameter is then presented in § 5. In § 6 we discuss the origin of photons in different energy domains: soft photons, below 20 MeV energy, identified as statistical emission of excited fragments and hard photons, above 20 MeV energy, identified as bremsstrahlung photons. In § 7 we present the first measurements of second order interference between nuclear photons. All the results obtained for bremsstrahlung photons are discussed and an interpretation of the data in terms of thermodynamics quantities is given in § 8. In § 9 the properties of neutral pions produced in the reactions below the free nucleon-nucleon threshold are presented and finally in § 10 we discuss the origin of the most energetic photons, with energies above the pion mass, in terms of pion radiative capture.

2 MODEL CALCULATIONS OF HEAVY-ION COLLISIONS

To theoretically describe the dynamics of heavy-ion collisions, one considers a system of interacting nucleons which experience two- (or more) body collisions, that are moving in a mean field, and which are subject to the Pauli exclusion principle. This problem can be described by the semiclassical transport equation, or Boltzmann equation, which is often simulated by using the pseudo-particle concept [2] (see appendix). There exist several models sharing these concepts and providing similar predictions on the gross properties of heavy-ion collisions. We have selected two models that we considered the best adapted to the production of particles (photons and mesons) at intermediate bombarding energies. First the Boltzmann-Uehling-Uhlenbeck (BUU) model of Cassing *et al.* [4] that includes the appropriate time evolution of the mean field and that is well suited to describe the bremsstrahlung-photon production and its dependence upon the parameters of the mean field.

The second is the Dubna Cascade Model (DCM) [10,13] which by its computational method is better suited for the description of rare events, like Deep Subthreshold Particle (DSP) production. At variance with the BUU model the time evolution of the mean field is simplified in this model. However, this has no effect on DSP production which takes place in the early phase of the heavy-ion collision before variations in the mean field start to play a role. Both models are presented in detail in the appendix.

2.1 Heavy-ion collision dynamics

Since only BUU incorporates the local mean-field dynamics, we will use it for the prediction of the heavy-ion collision dynamics, while the DCM code will be used to calculate the DSP production and to study their propagation through nuclear matter. We use the version [14,15] of the BUU code originally developed by the theory group of the University of Gießen [4].

Two possible scenarios emerge for central heavy-ion collisions for symmetric nucleus–nucleus systems, depending on the bombarding energy [8]. At bombarding energies above about $50A$ MeV, the two colliding nuclei strongly overlap to form a di-nuclear system of dense nuclear matter that subsequently expands violently and ultimately breaks up into many fragments, a process known as multifragmentation. Such an evolution is seen in the central collision of the Kr+Ni system at $100A$ MeV (Fig. 1). At bombarding energies below $50A$ MeV again a dense di-nuclear system is formed with a density 40% larger than the saturation density [16]. In contrast to the scenario at higher incident energies the attractive nuclear force is now strong enough to counterbalance

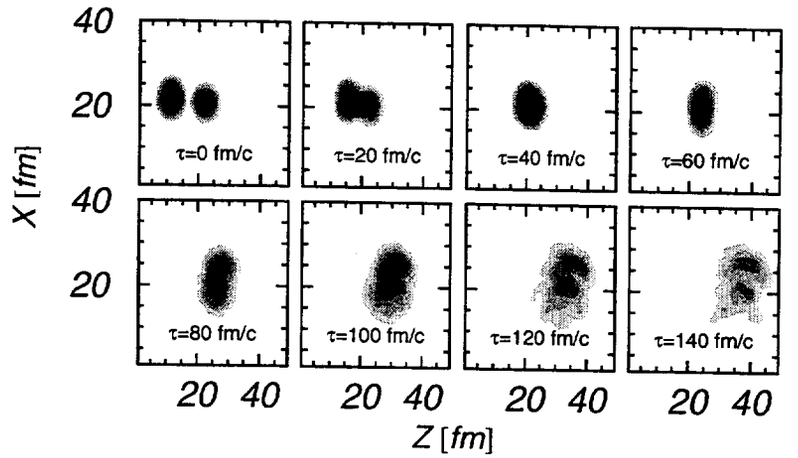

Fig. 1. *Time evolution, calculated with BUU, of a central (b=1 fm) collision Kr+Ni at 100A MeV shown as the density distribution of nucleons projected into the XZ coordinate plane. The beam axis is along Z.*

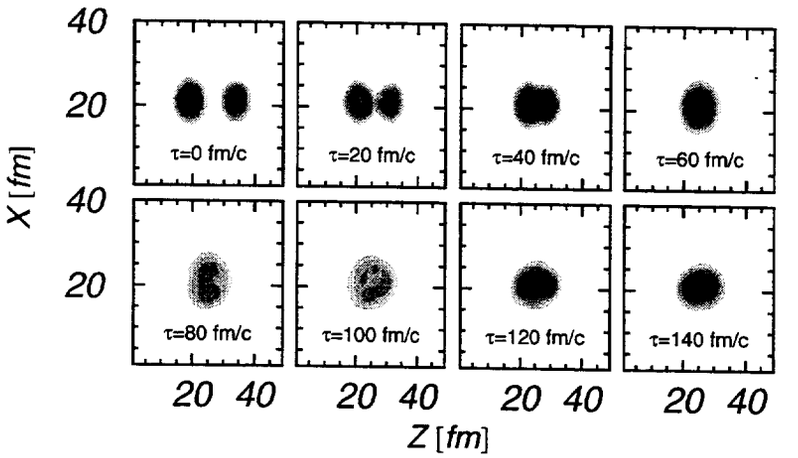

Fig. 2. *Same as Fig. 1 for 30A MeV.*

the initial expansion and to initiate a second compression phase of the system. The di-nuclear system subsequently undergoes density oscillations around the saturation density. Ultimately the system might partially fuse to form a hot nucleus. Such a scenario is evidenced for the reaction Kr+Ni at 30A MeV (Fig. 2). Viewing the same collision in momentum coordinates (Fig. 3), at the beginning of the collision the two Fermi spheres separated by the relative beam momentum are well identified. Later ($\tau > 80$ fm/c) during the second compression the momentum distribution is isotropic which indicates that the di-nuclear system is thermalizing.

The two presented scenarios are idealized. To be more realistic, it is necessary

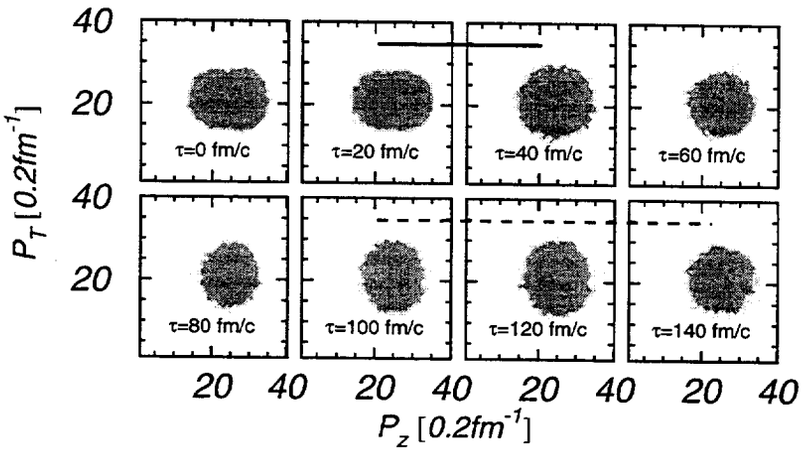

Fig. 3. *Time evolution, calculated with BUU, of a central collision Kr+Ni at 30A MeV shown as the density distribution of nucleons projected in the transverse-longitudinal momentum plane.The solid (dashed) horizontal line marks the emission time of direct (thermal) bremsstrahlung photons.*

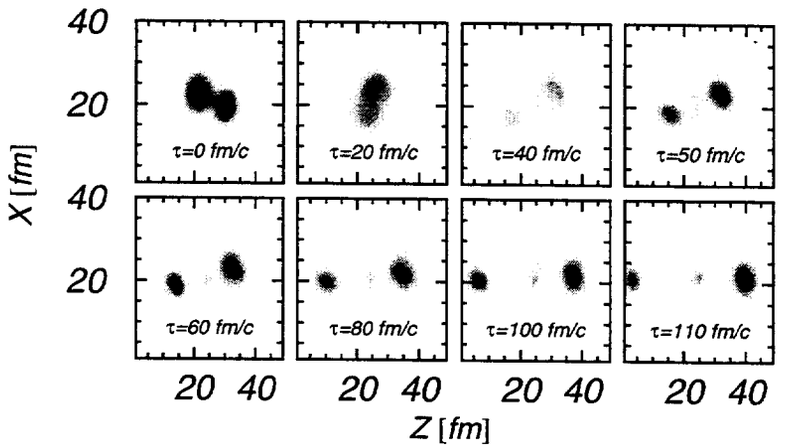

Fig. 4. *Same as Fig. 1 for the collision Kr+Ni at 60A MeV at b=3 fm.*

to average the collisions over impact parameter. On the other hand it was found that by selecting reactions in which hard photons are emitted, mainly central collisions are involved. We have experimentally determined that e.g. in the reaction Kr+Ni at 60A MeV the average impact parameter is 3 fm corresponding to 8% of the total reaction cross-section. During the time evolution (Fig. 4) calculated for an impact parameter of $b = 3$ fm, heavy fragments are formed after the first compression. Each of these fragments experiences density oscillations of the type discussed previously for the central collisions. The space-time structure of such dynamics can be analyzed by bremsstrahlung-photon interferometry (see discussion in § 7).

2.2 Bremsstrahlung dynamics

The photon emission is found to be intimately related to the dynamics of the heavy-ion collision. This is confirmed by the calculations of their production rates as a function of time, performed for central Ta+Au collisions at three bombarding energies $40A$, $60A$, $95A$ MeV and for three photon energy thresholds, 30, 80, 130 MeV. At all bombarding energies photon emission starts immediately at the beginning of the collision but lasts only for a short period. This photon flash coincides with the initial compression phase of the collision (Fig. 1). We denote these photons direct bremsstrahlung photons as they are produced in first chance NN collisions. At the lowest bombarding energy the flash of direct photons is followed by a second flash of NN bremsstrahlung photons emitted at a later stage of the heavy-ion collision during the second compression phase (Fig. 2), from subsequent NN collisions. During this later phase the di-nuclear system is thermalizing (the intrinsic momentum distribution becomes isotropic as seen in Fig. 3). Therefore we call these photons emitted in the second flash thermal bremsstrahlung photons.

As pointed out by several authors (e.g., Ref. [17]), spurious collisions do occur at the momentum-space surface due to an imperfect treatment of the Pauli blocking. As a consequence a low-energy photon contribution is artificially generated by the calculations. In such circumstances the intensity of this contribution cannot be exactly calculated and introduces a relative uncertainty on the intensity of the photon sources which might be particularly significant for the second and weaker one.

From the foregoing model calculations several conclusions can be drawn. Firstly, the bremsstrahlung-photon emission is well localized in space and time, the overlap zone of projectile and target (see Fig. 5). Secondly, the thermodynamic state of the photon sources appears to be well determined. The early source is dense but not yet thermalized, while the second can be considered to have already reached local thermal equilibrium. The properties of the photon emission from each of the two sources can be analyzed to extract thermodynamic properties of the hot and dense nuclear matter formed during the various stages of the heavy-ion collision:

- **Density:** since the direct-photon spectrum reflects the phase-space occupancy of the participating nucleons, its slope is a measure of the momentum distribution of nucleons forming the photon source, i.e., of the nuclear matter during the early stage of the heavy-ion collision. The density is deduced in the following way [16]. From systematic studies we find a dependence (see § 6.2, Eq. (40)) of the slope E_0^{incl} ("incl" stands for inclusive) of the photon spectrum as a function of the beam momentum (the empirical shape is of

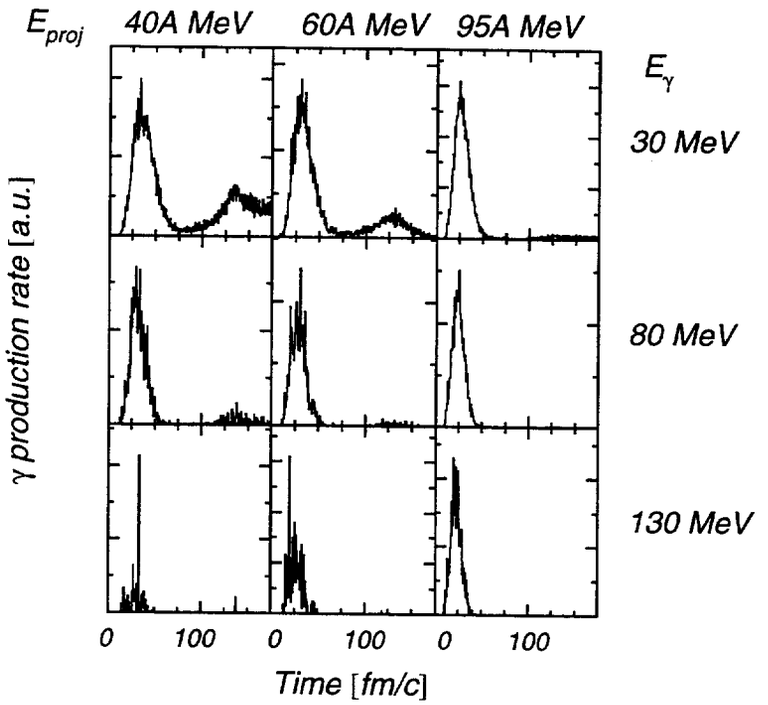

Fig. 5. *Bremsstrahlung-photon production rate calculated at three bombarding energies, 40, 60 and 95A MeV, and for three photon energy thresholds, 30, 80 and 130 MeV, as a function of the collision time. The system is Ta+Au at b=0 fm and* $K_\infty = 240$ *MeV.*

the form: $dN_\gamma/dE_\gamma \propto \exp(-E_\gamma/E_0)$):

$$E_0^{\text{incl}} = A\left(\frac{p_{\text{lab}}}{p_0}\right)^B, \tag{1}$$

with the values of the constants: $p_0 = 1$ fm^{-1}, $A = 8.43$ MeV·fm, and $B = 1.65$. Intuitively we can write that the variations of $\sqrt{s}$, the total energy available in a NN collision – $p_1 + p_2$, $p_1 = p_i + p_{\text{lab}}$, $p_2 = p_i$ –, with the intrinsic momentum p_i and the beam momentum p_{lab} are related by:

$$\frac{d\sqrt{s}}{dp_i} = 2 \times \frac{d\sqrt{s}}{dp_{\text{lab}}}. \tag{2}$$

By changing the impact parameter, b, the slope variation associated to the resulting exclusive photon spectra is related to a modification of the average intrinsic momentum:

$$E_0\left(p_{\text{lab}}, b\right) = f\left(p_{\text{lab}} + 2p_i(b)\right), \tag{3}$$

and the variation of the slope with b at a fixed bombarding energy:

$$\Delta E_0(b) = \left(\frac{df}{dp_i}\right) \Delta p_i(b). \tag{4}$$

Following the local density Thomas-Fermi approximation ($\hbar = c = 1$):

$$\rho(b) = \frac{2p_i^3(b)}{3\pi^2}, \tag{5}$$

one can convert the change in slope into a change in density:

$$\rho(b) = \rho_0 + \frac{2\left(p_F + \Delta p_i\right)^3}{3\pi^2}, \tag{6}$$

where we have further assumed that at saturation density, ρ_0, the intrinsic momentum is equal to the Fermi momentum, p_F.

- **Temperature:** since thermal photons are emitted from a hot and thermalizing source, the slope parameter E_0 should reflect the local temperature at the time of emission. However, since photons are not in thermal equilibrium with the nuclear medium E_0 and temperature are not equivalent. To evaluate the temperature we follow the kinetic photon production prescription proposed in Ref. [18] in which the system emitting thermal photons is assumed to be static during the photon emission. This is justified by the short emission time compared to the collision time (see Fig. 5). The photon emission rate is then only determined by the local conditions of the participant region. The photon emission rate is calculated by associating with each point in space a local density and temperature and by evaluating subsequently the collision rate:

$$\frac{dN}{d^4x dk d\Omega} = \frac{8}{4\pi} \int \frac{d\vec{p}_{1i}}{(2\pi)^3} \frac{d\vec{p}_{2i}}{(2\pi)^3} f(\vec{p}_{1i}) f(\vec{p}_{2i}) \| v_{12} \| \frac{d\sigma}{dk}, \tag{7}$$

where $\| v_{12} \| \frac{d\sigma}{dk}$ is the bremsstrahlung photon production rate (see Appendix) modified for the Pauli blocking (see Appendix), p the momenta of the colliding nucleons and $f(\vec{p})$ the single-particle momentum distribution sampled according to the Fermi-Dirac equilibrium distribution:

$$f(\mathbf{r}, p) = \frac{1}{1 + \exp\left(\frac{\sqrt{p^2 + M_N^2} + E_F(\rho)}{T}\right)}, \tag{8}$$

where M_N is the nucleon mass, E_F the density dependent Fermi energy and T the temperature. The results of these calculations (Fig. 6) indicate a net correlation between the nuclear temperature and the slope of the photon spectrum defined between 20 and 40 MeV photon energies.

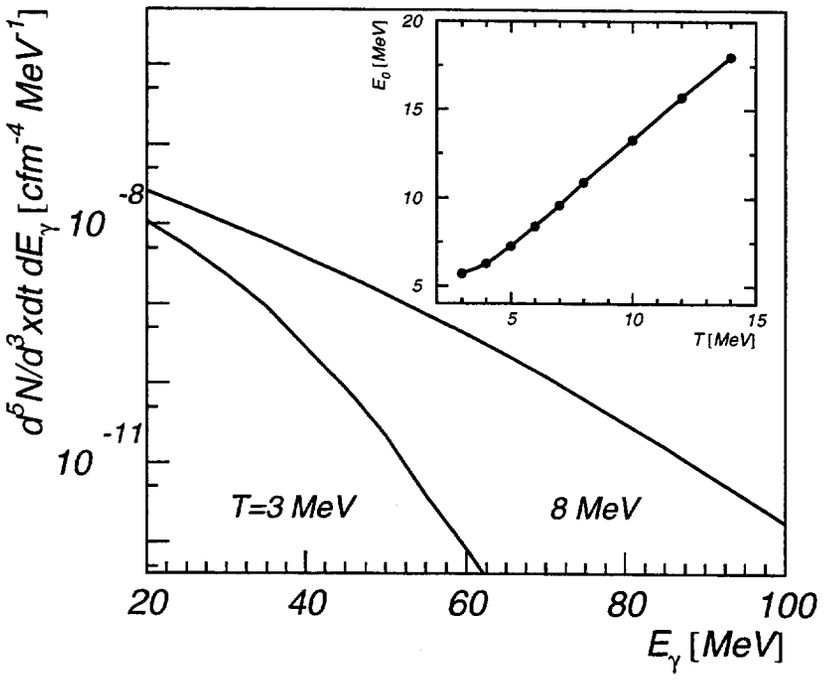

Fig. 6. *Photon emission rates from nuclear matter in thermal equilibrium at saturation density calculated for temperatures of 3 and 8 MeV. The inset displays the slope parameter E_0 obtained by an exponential fit to the calculated spectrum (between E_γ = 25 and 65 MeV) as a function of the temperature.*

- **Incompressibility modulus:** since the strength of the restoring force depends on the incompressibility of nuclear matter the second compression produces higher densities for larger K_∞. Hence the production rate of thermal photons is also sensitive to this parameter. This is demonstrated by the BUU calculations (Fig. 7). The emission rate of direct photons does not depend on K_∞, but the emission rate of thermal photons shows a strong dependence on this parameter. The calculations predict three times more thermal photons for a hard EOS than for a soft one. Therefore the relative intensity of the thermal photon source may provide a new and sensitive measure of K_∞.

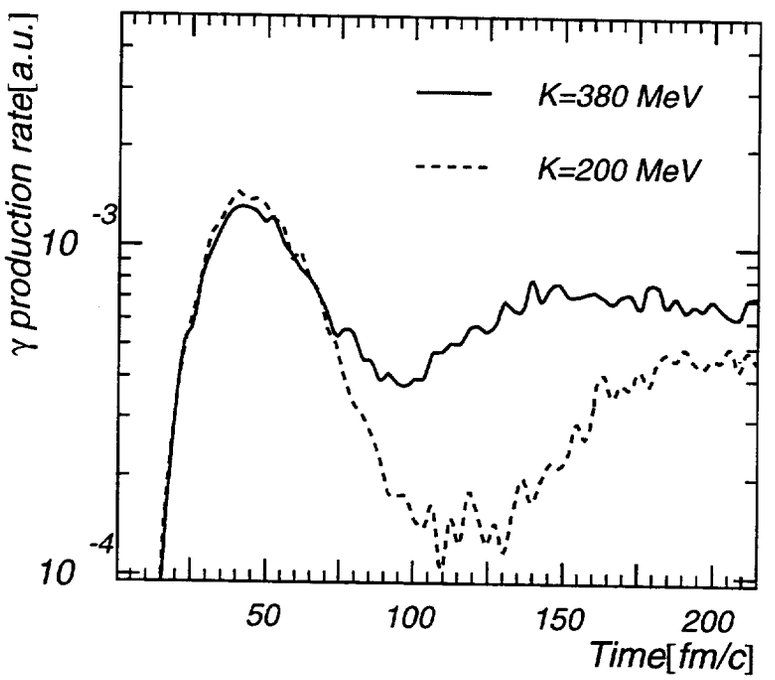

Fig. 7. *Production rate of bremsstrahlung photons ($E_\gamma \geq 30$ MeV) calculated with BUU as a function of time assuming a soft EOS with $K_\infty = 200$ MeV (dashed line) and a hard one with $K_\infty = 380$ MeV (solid line). The system is Ta+Au at 40A MeV and b=0 fm.*

3 THE EXPERIMENTAL SETUP

3.1 Detector lay-out

The experiments were performed at the GANIL facility in Caen, France. The detector system consisted of the photon spectrometer TAPS [19], the KVI Forward Wall FW [20] and the magnetic spectrometer SPEG [21]. The general lay-out of the three detection systems at the G3 beam line of GANIL is sketched in Fig. 8. The target was located in a cylindric vacuum chamber made of 3 mm thick PVC (0.018 radiation length) which minimizes the photon conversion. The 1 m long beam pipe upstream of the target was made of the same material. The cylindric part of the chamber was extended by a 1 mm thick aluminum cone which housed the Forward Wall.

3.1.1 The photon spectrometer TAPS

The "**T**wo **A**rms **P**hoton **S**pectrometer" [19,22] is designed to detect and identify photons from a few hundred keV up to a few GeV. It is a modular detector system consisting presently of 384 BaF_2 scintillation crystals. Each crystal is a 25 cm long (12 radiation lengths) prism of hexagonal cross section, the diameter of the inner circle being 5.9 cm (69% of the Molière radius). A 4 mm (0.0097 radiation length) thick NE102A plastic scintillator of hexagonal shape is positioned in front of each BaF_2 crystal. The plastic scintillator, called **C**harged **P**article **V**eto detector (CPV) [23,24], constitutes together with the BaF_2 crystal one TAPS module. The 384 modules can be assembled in various geometric configurations to fulfill the specific needs of a given experiment. The choice is always guided by a compromise between the optimization of electromagnetic-shower collection and solid-angle coverage. For the experiments discussed in this article, the modules were assembled to form blocks of 8×8 modules each. This configuration enables an optimum shower collection but with a limited solid-angle coverage. At the time of these experiments only 320 modules were available, i.e., five blocks. The blocks were positioned around the target at an average distance of 62 cm and covered an almost continuous polar angle θ range from 35° to 165° with respect to the beam direction. The positions of the centers of the five blocks are reported in Tab. 1. The total solid angle covered was equal to 17% of 4π.

3.1.2 The charged particle hodoscope FW

The KVI "**F**orward **W**all" [20] consisted of 60 phoswich detectors assembled as a wall positioned inside the vacuum chamber at 50 cm downstream of the target. The active surface of the 32 inner detectors was 3.25×3.25 cm^2 and

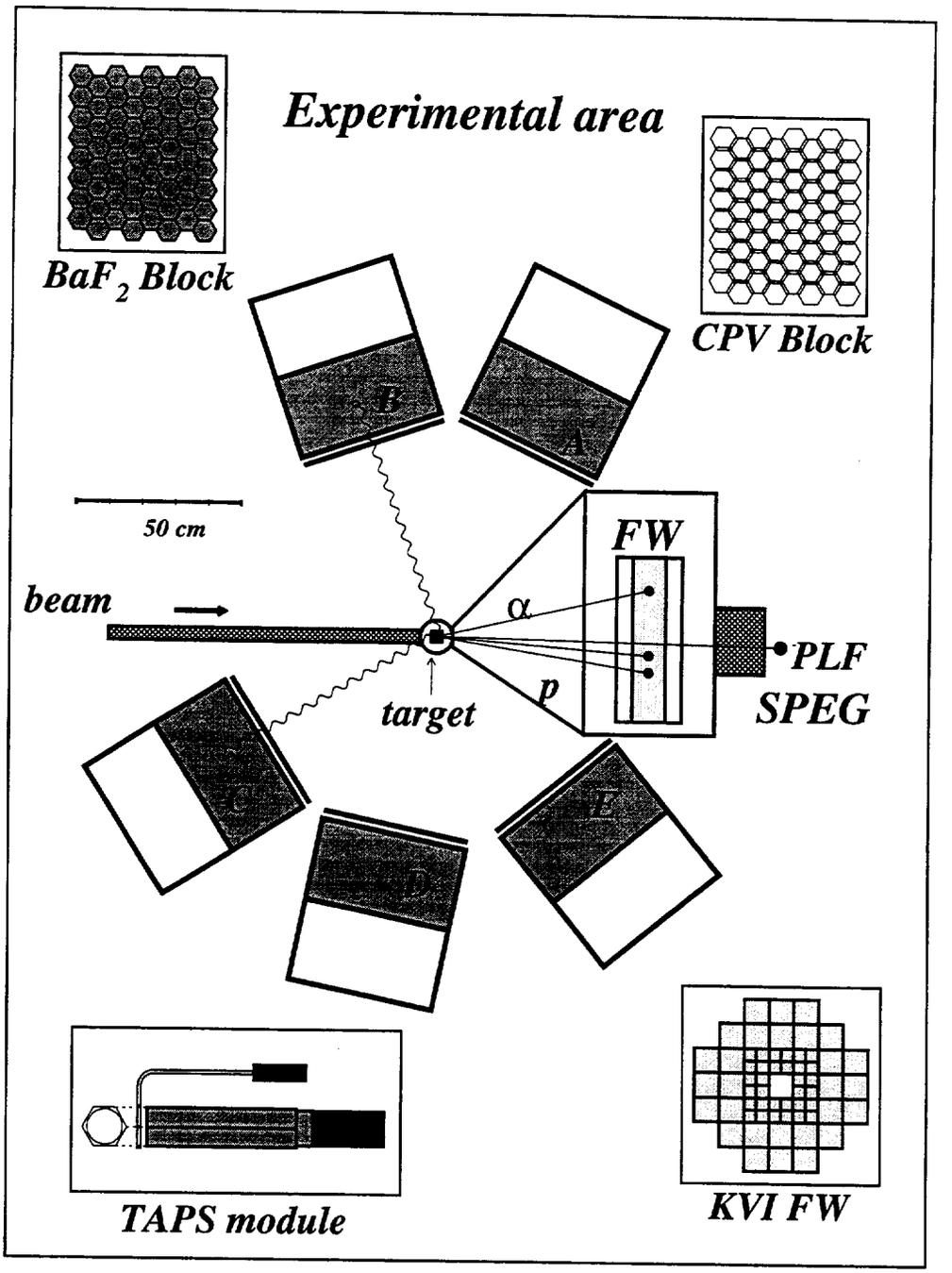

Fig. 8. *General view of the detection systems TAPS, FW and SPEG located at the G3 beam line of GANIL. The inserts (starting from the upper left corner and clockwise) show the front face of one BaF_2 block, the front face of one CPV block, the front face of FW, and one TAPS module.*

	A	B	C	D	E
d [cm]	65.2	64.5	62.1	61.3	60.0
θ [°]	64.6	108.6	147.9	101.8	50.9
Φ [°]	0.0	0.0	180.0	180.0	180.0

Table 1
Position of the central detector in the 5 blocks of TAPS (A-E): D is the distance to the target, θ the polar angle with respect to the beam direction and Φ the azimuth angle; $\Phi = 0°$ means the detector stands in the horizontal plane containing the beam axis and on the right-hand side of the beam axis when looking downstream and $\Phi = 180°$ on the left-hand side.

6.5×6.5 cm^2 for the 28 outer ones. The front layer of each detector consisted of a 1 mm fast scintillator NE102A backed by a 50 mm slow scintillator NE115. The light output of both scintillators was detected by a single photomultiplier. The detectors covered polar and azimuthal angles from 3.7° to 24.5° with respect to the beam direction. They were shielded with 100 μm Nickel foils to stop the intense flux of electrons and X-rays, and in the most forward region an additional 2 mm thick Aluminum foil was used to stop elastically scattered particles.

3.1.3 The magnetic spectrometer SPEG

The "**S**pectrometre à **P**erte d'**E**nergie du **G**anil" [21] is a high-resolution energy-loss magnetic spectrometer with the focal plane at a distance of 1450 cm from the target. It consists of two dipoles: the first one, called the *analyzer*, disperses the incoming beam in momentum and allows through horizontal slits to improve the energy resolution of the beam on the target located in its focal plane. The second dipole, called the *spectrometer*, consists of two distinct magnets and disperses the reaction products in momentum. Quadrupole magnets upstream of the target allow one to focus the beam on the target and to control the beam dispersion in angle and position. Others downstream from the target allow one to focus the reaction products in the plane containing the optical axis of the dipole and perpendicular to the direction of the magnetic field. A set of detectors is located in the vicinity of the focal plane of the spectrometer. It consisted of four 2 cm deep drift chambers (DC) with an active area of 80×12 cm^2 and filled with isobutane at an average pressure of 15 mbar. They provided at four different z positions the x and y coordinates of the reaction products with a position resolution of about 0.8 mm. This information is used to reconstruct the trajectory of the particles. The DC's were located 1404, 1424, 1491, 1511 cm from the target. A NE110 plastic scintillator (PL) at 1680 cm with the same active area as the DC provided the *stop* signals for the time-of-flight measurement of the particles. An ionisation

name	type	active area [cm^2]	thickness [cm]	z [cm]	material (pressure [mbar])
DCi	drift chamber	80×12	2	1404 1424 1491 1511	isobutane ($\sim$ 15)
IC	ionisation chamber	70×12	60	1568	isobutane (500 - 1500)
PL	plastic scintillator	120×15	2	1680	NE110

Table 2
Characteristics of the SPEG detection system and position of the elements along the optical axis z with respect to the target position.

chamber (IC) at 1568 cm from the target measured the energy loss of the reaction products. The pressure of the isobutane gas could be varied between 500 and 1500 mbar to match the range of the incoming particles. The active area of this detector was 70×12 cm^2. The positions and characteristics of the detectors are summarized in Tab. 2.

The data from SPEG were collected only during the Kr+Ni experiment. The spectrometer was positioned at 0° with respect to the beam direction and its magnetic field was set at two values to select projectile-like fragments (PLF) moving at 85% and 90% of the beam velocity. The momentum acceptance was $\Delta p/p = 7\%$ and the angular acceptance was ± 15 mrad in the horizontal and vertical directions.

3.2 Data acquisition

The electric signals delivered by the various detectors were shaped and digitized by standard NIM and CAMAC electronics partly developed at GANIL and GSI. High-voltage units and discriminators for TAPS were located in the experiment hall, the trigger electronics and the digitizing modules for TAPS in a first counting room, and the electronics for SPEG and FW in a second counting room distant by 50 m from the first one. The set-up parameters (high-voltage values, thresholds, gates widths and delays) of the CAMAC modules

were controlled by a VME processor through a VSB bus. A second VME processor controlled the read-out of the CAMAC modules through a VME bus and built the event. A third VME processor handled the data to construct histograms of raw parameters. A last VME processor controlled through a VME global memory the communications between the various VME processors and between the VME crate and a VAX station 3200. The communication between the VME processors located in the TAPS counting room, and those located in the SPEG/FW counting room and the target area was established through a VIC link. High level on-line analysis was performed by 3 work stations VAX 4000/60 receiving the data from the acquisition system through ETHERnet and the Transport Manager of GOOSY [25], a data analysis environment developed at GSI. A dedicated software package was developed [26] exploiting the PAW, KUIP and HBOOK package from the CERN software library [27]. It was used for the on-line data analysis as well as for the off-line analysis. The various parameters for each detection system were recorded on magnetic tapes (EXABYTE format) on an event-by-event basis.

3.2.1 TAPS

The acquisition system recognized a hit in any BaF_2 detector when the recorded energy surpassed a threshold of 1.5 MeV photon equivalent. For CPV the threshold was 500 keV. Hit patterns, H_{BaF_2} and H_{CPV} are constructed and the hit multiplicity M_{hit1} is calculated. For each hit module the following parameters are stored:

- the identification number *Id* of the module;
- the total energy E_w (w stands for **w**ide gate) obtained by charge integration over 2 μs of the signal delivered by the photomultiplier;
- the partial energy E_n (n stands for **n**arrow gate) obtained by charge integration over the first 30 ns of the signal delivered by the photomultiplier;
- the time-of-flight T measured with respect to the radio frequency (RF) signal delivered by the cyclotron and signaling the impact of a beam burst on the target.

In parallel, the total number of modules $M_{neutral}$ and the number of modules in each block M_{block}, with an energy deposit in BaF_2 surpassing a second threshold of 20 MeV and **no** signal in CPV were stored to be used for definition of various trigger modes. These events were attributed to neutral particles, photon and neutron. The number of modules M_{hit2} which fired above the 10 MeV threshold irrespective of the status of CPV was also stored.

3.2.2 FW

As for TAPS, two energies and a time were recorded per module of the Forward Wall to enable the identification of the detected particles. However, in the present experiments, only the number of detected particles per event M_{FW} was considered, i.e., the multiplicity of charged particles irrespective of the nature of the particle. This information entered also the trigger definition.

3.2.3 SPEG

The SPEG detection system provided for each detected reaction product the following parameters:

- the $(x_i,y_i)_{i=1,4}$ coordinates from the DC detectors which define the trajectory of the particle;
- the time between the RF signal and the PL time, T_{PL};
- the energy loss inside the ionisation chamber, ΔE_{IC};
- the total energy deposited by the fragments stopped in the plastic scintillator, E_{PL}.

The PL time entered the definition of the triggers.

3.2.4 Trigger definition

Various trigger configurations were defined using the trigger signals delivered by the three detector systems and mixed in standard NIM logic electronics. Each trigger favored a given type of events and could be scaled-down if necessary to balance their counting rates. The various triggers exploited in the present analysis are described in Tab. 3.

The first four triggers are the minimum bias triggers for the three detectors systems. The triggers "γspeg" and "γfw" select neutral particles in coincidence with PLF detected in SPEG and charged particles detected in FW. They are used to analyze the properties of the bremsstrahlung-photon emission as a function of the impact parameter deduced from the mass of the PLF and/or the multiplicity of charged particles. Triggers "$\gamma\gamma$" and "2γ" will be used to analyze the photon-photon correlations and to identify the π^0 decay. The "$\gamma\gamma$" trigger requires that the two neutral particles have hit a single block. It selects photon-photon coincidences with small relative momenta or very energetic photon which develop large showers. The "2γ" trigger selects photon-photon coincidences with large relative momenta, i.e, mainly π^0. Both triggers were defined in coincidence with a valid trigger from FW to sign the occurrence of a nuclear reaction. It has been verified that this additional condition does not introduce a bias on the event selection but helps to reduce false events due

name	event	definition	scale-down		
			Kr+Ni	Ta+Au	Pb+Au
taps low	single photon	$M_{\text{hit1}} \geq 1$	2^{15}	-	-
taps high	single photon	$M_{\text{hit2}} \geq 1$	2^{9}	-	-
γ	single neutral	$M_{\text{neutral}} \geq 1$	2^{10}	-	-
speg	single PLF	$T_{\text{PL}} \geq 0$	2^{10}	-	-
fw	single particles	$M_{\text{FW}} \geq 1$	2^{14}	2^{15}	-
γspeg	photon-PLF coincidences	$M_{\text{neutral}} \geq 1$ && $T_{\text{PL}} \geq 0$	2^{3}	-	-
γfw	photon-particle coincidences	$M_{\text{neutral}} \geq 1$ && $M_{\text{FW}} \geq 3$	2^{8}	2^{6}	2^{4}
$\gamma\gamma$	photon-photon coincidences	$M_{\text{neutral}} \geq 2$ && $M_{\text{block}} = 1$ && $M_{\text{FW}} \geq 3$	1	1	-
2γ	photon-photon coincidences and π^0	$M_{\text{neutral}} \geq 2$ && $M_{\text{block}} \geq 2$ && $M_{\text{FW}} \geq 3$	1	1	1
highγ	high energy photon	$M_{\text{neutral}} \geq 2$ && $M_{\text{block}} = 1$	1	1	-

Table 3
Trigger definitions used in the analysis of the present experiments. A dash in the scale-down column indicates that this trigger was not in use for the specified experiment.

to cosmic rays which can fire in TAPS simultaneously several modules or even several blocks.

Several other triggers were defined to control the operation of the detector system during the experiment but were not used during the off-line analysis.

A last trigger selecting charged particles identified in TAPS by requiring a coincidence between BaF_2 and CPV was defined to select electron pairs [28], but because of the low counting rate it only provided data with marginal statistics.

3.3 Systems studied

Data for the three systems reported in Tab. 4 were collected. These systems were ^{86}Kr + ^{nat}Ni at 60A MeV, ^{181}Ta + ^{197}Au at 40A MeV and ^{208}Pb + ^{197}Au at 30A MeV. The beams were delivered by the GANIL facility. The thickness of the targets and the effective beam time are also reported in Tab. 4. The longest beam time was devoted to the Kr+Ni system. The main goal was to measure with high statistics the correlation between hard photons and to search for the existence of an intensity interference effect. Enough data were collected to study as a byproduct the properties of the bremsstrahlung-photon emission as a function of the impact parameter. In the Ta+Au system data were collected to measure the photon-photon correlation. SPEG being switched off during this experiment to reduce the dead-time introduced by the read-out of the SPEG parameters, no data on photon-PLF correlation are available. Only 32 hours were allocated to the last measurement in the system Pb+Au, therefore only data for single bremsstrahlung-photon emission could be collected with reasonable statistics.

projectile	time [hours]	energy [A MeV]	average intensity [10^9particles/s]	target	thickness [mg/cm^2]
^{86}Kr	200	60	1.8	^{nat}Ni	11.9
^{181}Ta	80	40	0.9	^{197}Au	11.2
^{208}Pb	32	30	0.8	^{197}Au	11.2

Table 4
Nuclear collision systems studied.

4 PARTICLE IDENTIFICATION

As already mentioned, we did not identify in the present analysis the charged particles detected in the FW and we have extracted only the multiplicity of firing detectors M_{CP}, that is the multiplicity of mainly proton and light ions. Particles detected with TAPS were identified as either photons, electrons, neutrons or ions with Z$\geq$ 1 (mainly protons). Events detected in TAPS were

further identified as single photons, photon pairs, neutral pions, electron pairs or cosmic-muon induced showers. The reaction products analyzed by SPEG were identified in mass, charge and momentum.

4.1 TAPS

The four parameters H_{CPV}, E_w, E_n, T recorded for every hit TAPS module provide all the information for a redundant particle identification using time-of-flight, CPV response and pulse-shape.

4.1.1 Time-of-flight

The flight path between the target and the front face of the BaF_2 detectors was on average 62 cm. Owing to the excellent timing properties of the fast component of the BaF_2 light output this distance is sufficient at the bombarding energies of the present experiments to discriminate between electromagnetic particles (photons and electrons) and massive particles (mainly neutrons and protons). However to achieve an optimal time resolution several corrections, which rectify imperfections in the electronics and the instability of the RF signal, were applied to the measured time. Beforehand, all T's were aligned to have the prompt peak at the same position defined as time zero, T_0.

Walk correction

The time signal for the BaF_2 scintillators is delivered by 8 fold CAMAC constant-fraction-discriminators FCC8 [29] that provide an automatic walk correction. However, in the off-line analysis we observed a residual dependence of the time on the amplitude of the signal. Between 1 and 8 MeV variations of up to 400 ps were measured. This dependence was determined through an automatic procedure which calculates for 7 amplitude intervals the shift of the prompt time-peak position with respect to a fixed reference. The intervals were 1 MeV wide and covered the range between 1 and 8 MeV.

RF drift correction

Drifts in the RF time signal were observed during the experiments. They occur when the accelerator parameters which modify the trajectory of the beam and hence its time-of-flight are changed. The drift of the order of 100 ps per hour was rather smooth. Nevertheless after a shut-down of the accelerating system we observed sudden variations as large as 1 ns. The drift was continuously monitored by accumulating all 320 BaF_2 times in a single histogram. Every

10,000 events, which correspond to roughly 10 minutes, the shift of the prompt peak with respect to a fixed reference was calculated and stored for later use.

Cross-talk correction

The timing signals were transported through 8 fold ECL cables and digitized in the 8 fold CAMAC TDC1612F [29]. The cross talk induced in the cables and in the TDC caused time shifts of the order of 1 ns depending on the hit pattern at the entry of the TDC. Systematic measurements demonstrated [30] that the shifts are additive so that, for example, $S^1_{23} = S^1_2 + S^1_3$ where S^i_{jk} denotes the shift in channel i when channels i, j, k are hit. It was therefore only necessary to determine the 8×8 $S^{i=1,8}_{i,j=1,8}$ values for each TDC which correspond to the shift induced in the presence of 2 hits at the input.

4.1.2 Time calibration

The time spectra were calibrated using the time structure of the pulsed beam. For the Kr+Ni experiment, for example, the time difference between two beam bursts was 90 ns. The range of the TDC was set to 200 ns so that 3 beam bursts were observed in the time spectra.

In the resulting time spectrum (Fig. 9) the prompt peak, due to photons and electrons travelling at the velocity of light, has a full width at half maximum of 600 ps reflecting mainly the width of the beam burst on average equal to 500 ps. The broad bump observed at larger time-of-flight corresponds to massive particles, mainly neutrons and protons. The flat background under these structures is due to cosmic ray induced events in random coincidence with the RF time signal. The time-of-flight provides thus a first discrimination between electromagnetic particles and hadrons. Setting a gate width of 1.8 ns on the prompt peak the massive particles are almost totally eliminated except for those having the largest velocities. The two next criteria will help to eliminate totally this contribution.

4.1.3 CPV bit set

Charged particles deposit energy in the thin plastic scintillator CPV and are stopped in the BaF_2, whereas the CPV is transparent to photons and neutrons. As described in Tab. 3, only neutral events entered the trigger definition, but once a trigger condition was satisfied all hit detectors were recorded irrespective of the status of the corresponding CPV. Using the information stored in the veto-bit H_{CPV} we have a criterion to discriminate between charged and neutral particles.

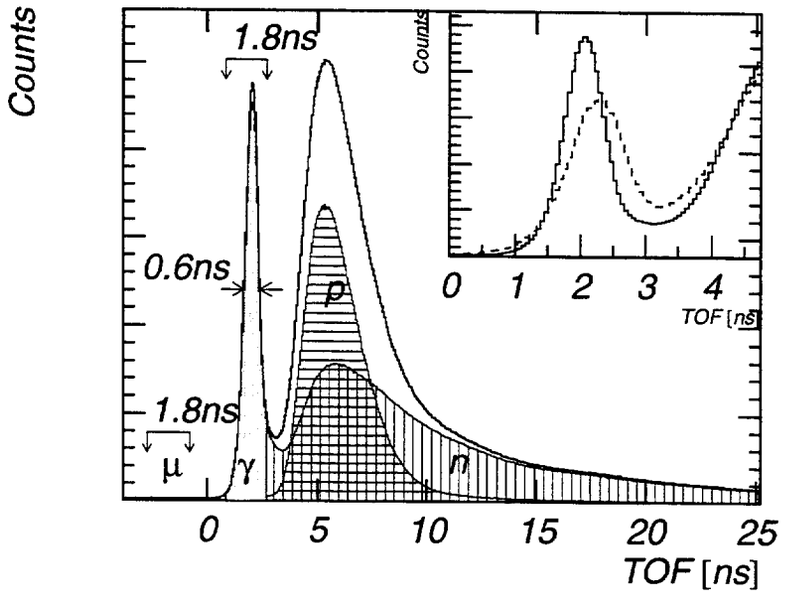

Fig. 9. *Time-of-flight spectrum obtained in the reaction* ^{86}Kr + ^{nat}Ni *at 60A MeV. The 320 individual time-of-flight spectra have been aligned with respect to a fixed reference and corrected as described in the text. The inset shows the spectrum before (dashed line) and after (continuous line) the corrections.*

The efficiency of CPV to detect protons with energies larger than 100 MeV was estimated by comparing the pulse shape and the CPV information [22] to be 80 %. Less energetic protons are slowed down or stopped in the wall of the scattering chamber, the air and CPV itself. They deposit therefore a small amount of energy, if any and are thus not detected. The remaining 20% of particles identified as protons in BaF_2 but not in the CPV (see next section) are most likely induced by (n,p) reactions in the scintillator.

The efficiency of CPV to detect an electron was estimated to be 90 % [22].

4.1.4 Pulse-shape discrimination

The response of a BaF_2 scintillator is different when the incident particle is an electromagnetic particle or a neutron on one hand and a proton or a light particle on the other hand [31]. The pulse-shape thus provides a discrimination criterion best observed in a map of E_w versus E_n (Fig. 10). The upper branch corresponds to the detection of photons, electrons or neutrons and the lower one to protons and light particles. Charged pions would be intermediate [32] and show up in between the two branches. This third branch is however not clearly seen in the spectrum because of the weak π-production cross section.

The discrimination was performed by an automatic search of the minimum

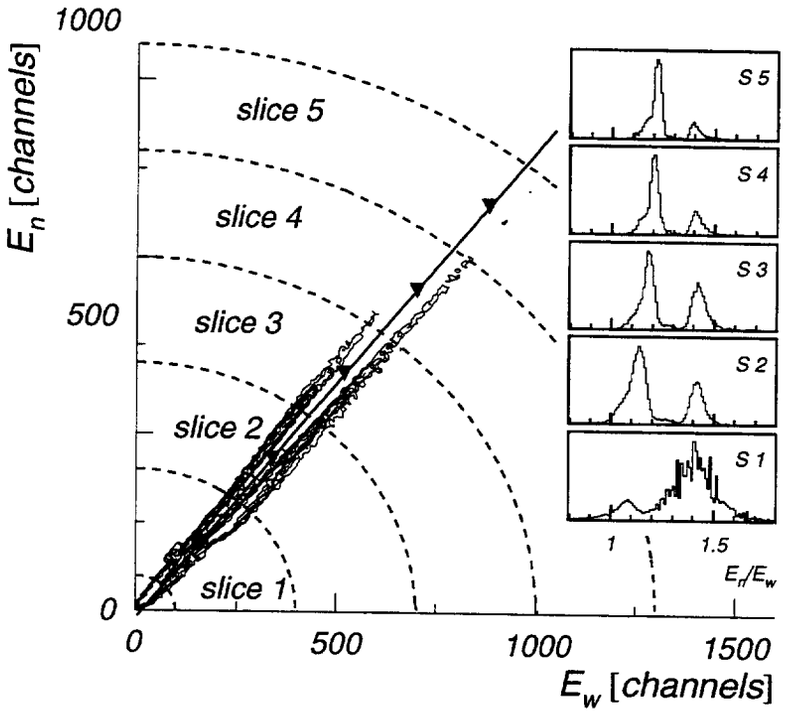

Fig. 10. *E_w versus E_n measured in a single TAPS BaF_2 detector for the reaction $^{86}Kr + ^{nat}Ni$ at 60A MeV. The upper branch corresponds to the detection of photons, electrons or neutrons and the lower one to protons and light particles. The inserts display projections on E_n/E_w for selected slices defined in the main figure.*

of the valley between the two main branches. The E_w versus E_n map was therefore divided into 5 concentric energy bins (Fig. 10). The positions of the minimum in each bin were then fitted to a linear function, E_w vs E_n, which defined the discrimination line. It was checked that during the experiments the parameters of the function remained constant.

4.1.5 Energy calibration

Because of the light output properties of BaF_2 scintillators [33], the energy calibration is only valid for electromagnetic particles and thus provides an approximate energy calibration for neutrons and protons or light ions. The following calibration points were used:

- the charge to digital converter pedestal provides the intercept at E_γ=0 and corresponds to the output of the QDC1612F [29] in the absence of a signal at the input.
- The energies of radioactive sources:
  · ^{88}Y, E_γ=0.898 MeV and 1.836 MeV;
  · AmBe, E_γ=4.43 MeV.

- Minimum ionising muons from the cosmic radiation deposit an energy proportional to the distance traveled through the scintillator. With the present TAPS geometry the average energy deposit estimated from GEANT [34] simulations was 38.5 MeV.

To obtain an absolute energy calibration, it is still necessary to correct for i) differences in the light production efficiency for photons and muons, ii) the amount of shower energy which escapes out of the detector in the longitudinal directions and iii) the energy thresholds in the constant-fraction discriminator. A global correction factor was calculated by adjusting in the invariant-mass spectrum the π^0 peak to M_{π^0}=134.9 MeV. The factor was found to be equal to 1.11.

4.1.6 Shower analysis

At this stage of the analysis a particle detected by TAPS is characterized by three parameters which are concatenated in a 3-bit word, PVT. It is defined in the following way:

P (most significant bit) = 1 if the particle is identified as an electromagnetic particle or a neutron by the pulse-shape analysis;
V (bit 1) = 1 if the particle is identified as a charged particle by CPV;
T (least significant bit) = 1 if the particle is identified as a prompt particle by the time-of-flight analysis.

With this notation a photon will be marked by PVT=$(101)_{\text{binary}}$=$(5)_{\text{decimal}}$, an electron by PVT=$(111)_{\text{binary}}$=$(7)_{\text{decimal}}$, a neutron by PVT=$(100)_{\text{binary}}$=$(4)_{\text{decimal}}$ and a proton or a light ion by PVT=$(010)_{\text{binary}}$ =$(2)_{\text{decimal}}$.

A high energy photon entering a BaF_2 detector will form an electromagnetic shower which lateral development can fire several neighbouring detectors. In our analysis a cluster was defined as a continuous ensemble of hit detectors. We have distinguished three kinds of clusters:

type 1 all the modules belonging to the cluster have PVT=5;
type 2 all the modules belonging to the cluster have PVT=5 except for one having PVT=7;
type 3 all the modules belonging to the cluster have PVT=5 except for a few having PVT=1 or PVT=2

Type 1 clusters are identified as a single photon, type 2 as a single electron and type 3 are single photons contaminated by one or more charged particle. We have estimated that only 6% of the photons develop this latter type of cluster and we have excluded it from our analysis.

If the position of module i in the laboratory coordinate is denoted by r_i and if E_i is the corresponding measured energy then the total energy E of the incident particle can be calculated by summing all energies in the cluster [35]:

$$E = \sum_i E_i, \tag{9}$$

and its position r as:

$$r = \frac{\sum_i W_i r_i}{\sum_i W_i}, \tag{10}$$

where

$$W_i = MAX\left\{0, W_0 + \ln\frac{E_i}{E}\right\}. \tag{11}$$

The value of the constant $W_0 = 4$ in Eq. (11) was obtained from GEANT simulations. To achieve a better determination of the incident particle direction, we had to take into account that the shower develops after having traveled inside the detector an average distance Z:

$$Z = MAX\left\{0, \left(\ln\frac{E}{E_c} + 1.2\right) X_0\right\}, \tag{12}$$

where E_c is the critical energy equal to 12.78 MeV for BaF_2 and X_0 is its radiation length. This results in a correction on the polar angle of the incident particle which amounts on average to 3% for a photon with an energy between 25 and 100 MeV.

This shower reconstruction technique allows the determination of the direction and the energy of the incident particle with an energy resolution estimated from GEANT simulations to be 5% for a 70 MeV photon and a precision on the direction of 1°.

4.1.7 π^0 identification

Because of their short life time π^0 disintegrate before reaching the detector by the back to back emission of two photons (branching ratio equal to 98.8%) distributed isotropically in the π^0 rest frame. In the laboratory, due to the Lorentz boost the two photons are emitted with a relative angle smaller than 180°. For a $60A$ MeV incident beam energy, the average opening angle is $\theta_{\gamma\gamma} = 160°$, if we assume that the pion is created in the NN center-of-mass. To identify neutral pions, the modulus of the relative four-momentum, Lorentz

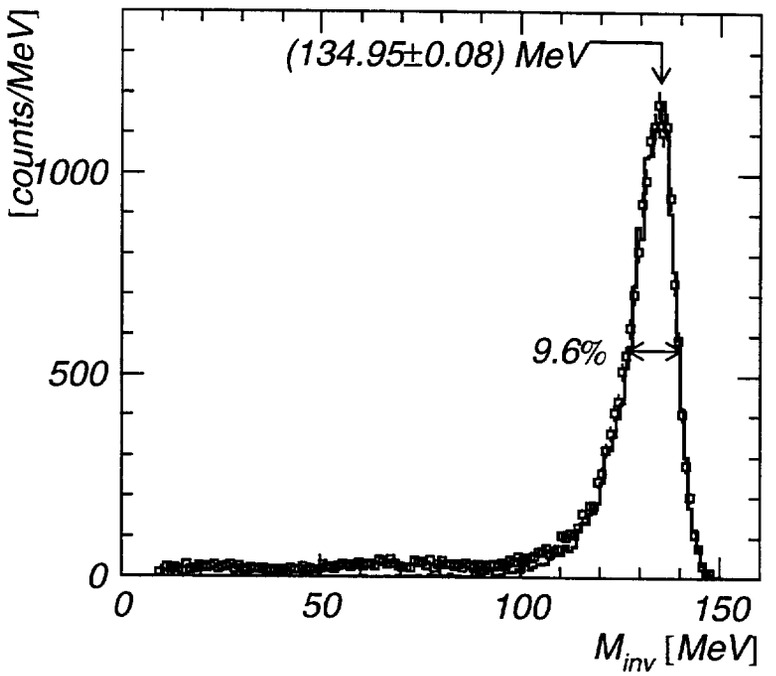

Fig. 11. *Invariant-mass spectrum measured in the reaction* ^{86}Kr + ^{nat}Ni *at 60A MeV. The resolution of the* π^0 *peak is 9.6%. The solid line represents the spectrum calculated with GEANT.*

invariant, which for photons is equal to the invariant mass $M_{\rm inv}$ is calculated taking all combinations of pairs of photons detected in one event.

$$Q_{\rm inv} = \sqrt{q^2 - q_0^2} = \sqrt{2E_{\gamma_1}E_{\gamma_2}(1-\cos\theta_{\gamma\gamma})} = M_{\rm inv}, \tag{13}$$

where q and q_0 are the relative momentum and energy respectively. In the invariant mass spectrum measured in the reaction Kr + Ni at 60A MeV (Fig. 11), the π^0 peak is clearly seen at its rest mass. The resolution (full width half maximum) was equal to 9.6%.

4.1.8 Cosmic-ray identification

Whereas cosmic muons are useful to calibrate TAPS BaF_2 detectors, they constitute a noise on top of rare events like subthreshold pion emission or 2-photon events. It is therefore essential to identify them with extremely high accuracy. We have used the following characteristics of cosmic-ray induced events:

- the particles of the hard component of the cosmic-ray spectrum cross the TAPS blocks along a nearly linear trajectory;

- those of the soft component are stopped in the surface detectors of the block;
- cosmic rays inducing showers in the concrete roof of the experimental area generate events with unusual high multiplicity.

The photon showers (type 1) were therefore characterized by three additional parameters:

(i) $\mathcal{M}$, the multiplicity of the shower, i.e., the number of modules forming the cluster;

(ii) $\mathcal{L}$, the linearity coefficient of the shower defined as:

$$\mathcal{L} = \frac{\lambda_1 - \lambda_2}{\lambda_1 + \lambda_2}, \tag{14}$$

where λ_i are the eigenvalues of the sphericity tensor:

$$(S) = \begin{pmatrix} S_{xx} & S_{xy} \\ S_{yx} & S_{yy} \end{pmatrix}, \tag{15}$$

with the following definitions:

$$\begin{aligned} S_{xx} &= \sum_i E_i x_i^2, \\ S_{xy} &= S_{yx} = \sum_i E_i x_i y_i, \\ S_{yy} &= \sum_i E_i y_i^2, \end{aligned} \tag{16}$$

where x_i, y_i are the coordinates of the modules in the block reference frame;

(iii) $\mathcal{S}$, the surface energy which represents the amount of the shower energy deposited in modules on the surface of a block:

$$\mathcal{S} = \frac{\sum_{i \in \text{surface}} E_i}{\sum_i E_i}. \tag{17}$$

From the analysis of simulated events for photons and cosmic–ray events we have established several criteria combining the three parameters previously defined. The result was that almost all the cosmic-rays induced events could be eliminated while the same criteria rejected at most 10% of the photon events of interest. A detailed description of the cosmic–ray rejection method can be found in Ref. [22,36].

4.2 SPEG

The identification in mass A, charge Z and momentum p, of the PLF detected in SPEG was performed in three steps. First the trajectory of the particle was determined, then its velocity was calculated, and finally its mass and charge were deduced.

4.2.1 Trajectory reconstruction

The trajectory of the particle inside SPEG was reconstructed using the four horizontal positions x_i measured with the drift chambers (see § 3.2.3). The detectors were first calibrated using beam particles of known energy and by varying the value of the field in the spectrometer dipole. A variation in magnetic rigidity $B\rho$ of 1% corresponds to a displacement in the focal plane of 10.4 cm. We have then adjusted to the four measured points a first order polynomial of the form:

$$x = x_0 + \tan\theta_{\text{foc}} \cdot z, \tag{18}$$

z denotes the position of the drift chamber on the optical axis; θ_{foc} is the angle in the focal plane between the trajectory of the particle and the optical axis from which the position X_{foc} of the particle in the focal plane is deduced. The magnetic rigidity of the particle is then calculated as follows:

$$B\rho = \left(1 + \frac{X_{\text{foc}}}{10.4\text{cm}}\right)(B\rho)_0, \tag{19}$$

where $(B\rho)_0$ is the reference rigidity at which the particle travels along the optical axis.

4.2.2 Velocity calculation

The velocity of the particle is calculated from the length l_{flight} of its trajectory and from the measured time-of-flight:

$$l_{\text{flight}} = l_0\,(1 + aX_{\text{foc}} + b\theta_{\text{foc}})\,, \tag{20}$$

where l_0 is the length of the trajectory along the optical axis from the target to the PL detector ($l_0 = 1680$ cm):

$$v_{\text{PLF}} = \frac{l_{\text{flight}}}{t_{\text{flight}}}, \tag{21}$$

and t_{flight} is derived from the time information delivered by the PS detector. The parameters a and b are evaluated by measuring the time of flight for particles of known velocity like, for example, the elastically scattered beam particles.

4.2.3 Mass and charge calculation

Using the values for v_{PLF} [Eq. (21)] and for $B\rho$ [Eq. (19)], the mass over charge ratio A/Q of the detected particles is calculated using the following relations:

$$B\rho = \frac{AM_N}{Qe} v_{\text{PLF}}, \tag{22}$$

$$\frac{A}{Q} = \frac{e}{M_N}(B\rho)_0 \left(1 + \frac{X_{\text{foc}}}{10.4\text{cm}}\right) \frac{l_{\text{flight}}}{t_{\text{flight}}}, \tag{23}$$

where M_N is the mass of the nucleon and e the elementary electric charge. The experiment including SPEG used a ^{86}Kr beam in the 34^+ charge state and the projectile was fully stripped after passing the target. Therefore the charge of the produced PLF is equal to its atomic number: $Q = Z$.

The charge of the particle is calculated from the energy loss measured in the IC detector using the Bethe formula and the velocity calculated from Eq. (21):

$$Z^2_{\text{PLF}} \propto \frac{E \cdot \Delta E}{A} = \frac{1}{2} v^2_{\text{PLF}} \Delta E, \tag{24}$$

$$Z_{\text{PLF}} \propto \frac{\Delta E^{\alpha}}{v_{\text{PLF}}}, \tag{25}$$

where α was adjusted to achieve the best resolution. We found $\alpha = 0.496$. The y positions of the particles in the IC detector were used to correct for recombination losses of electrons during their drift towards the anode. Finally the gain drift of the IC was monitored and corrected. The final resolution on Z was then equal to 1.1% which permitted the identification of all elements (Fig. 12) from the projectile Kr (Z=36) down to B (Z=5).

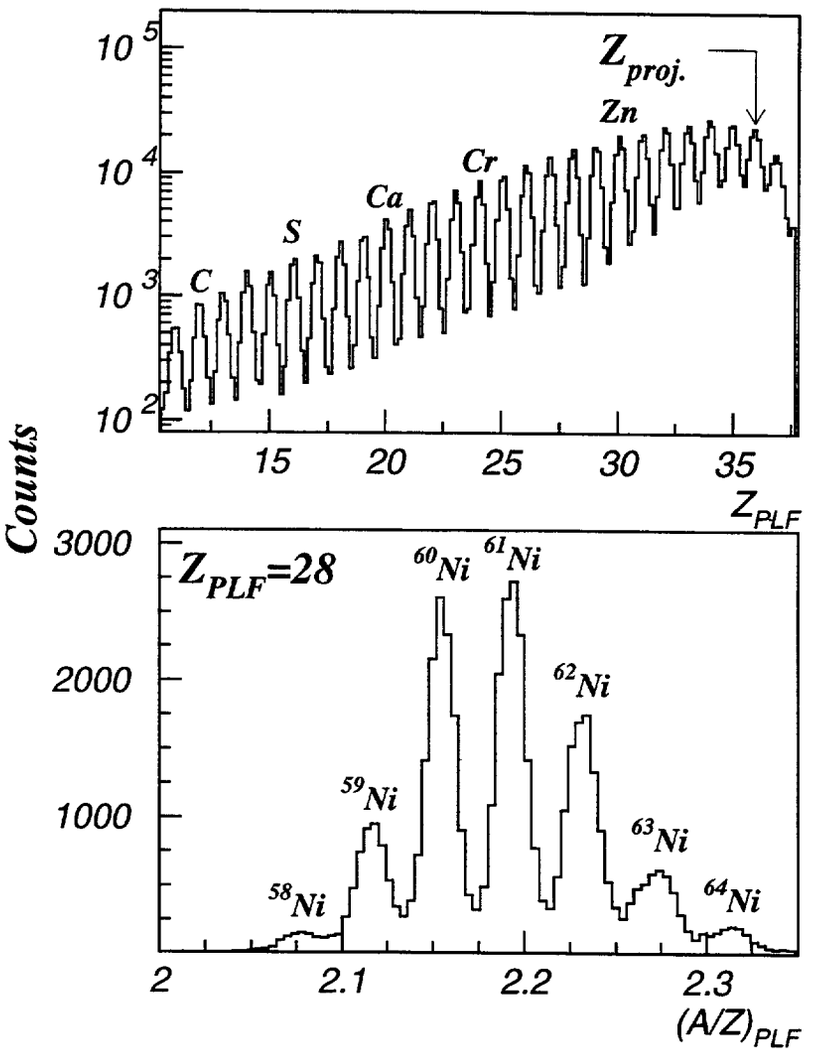

Fig. 12. *Z distribution of the PLF detected in SPEG, set at* $B\rho = 0.85(B\rho)_{\text{beam}}$, *and produced in the reaction* $^{86}Kr + ^{\text{nat}}Ni$ *at 60A MeV. The lower panel shows the distribution of the nickel isotopes.*

5 EVENT CHARACTERIZATION

The charged particle multiplicity, M_{CP}, measured with FW and/or the mass and the velocity of the projectile-like fragment, A_{PLF} and v_{PLF}, measured with SPEG were used to classify reactions according to their impact parameter b. The absolute value of b was calculated [16] following the procedure suggested in Ref. [37] which incorporates the associated bremsstrahlung-photon multiplicity, M_γ, and the geometrical model of Ref. [38].

The experimental photon multiplicity associated with a reaction channel ν is defined as the ratio between the number of events of reaction channel ν in coincidence with a photon and the total number of events associated with the reaction channel:

$$M_\gamma^\nu = \frac{N_\gamma^\nu}{N_R^\nu}. \tag{26}$$

In the variation of M_γ^ν (Fig. 13) with M_{CP} and A_{PLF}, the strong correlation indicates that the highest photon multiplicity is obtained for the largest charged-particle multiplicity and for the largest loss of projectile mass. This is an expected behavior since, on one hand, M_{CP} is a rough measure of the centrality of the collision, mainly selecting intermediate to small impact parameters, and on the other hand the mass transfer, that can be linked intuitively to

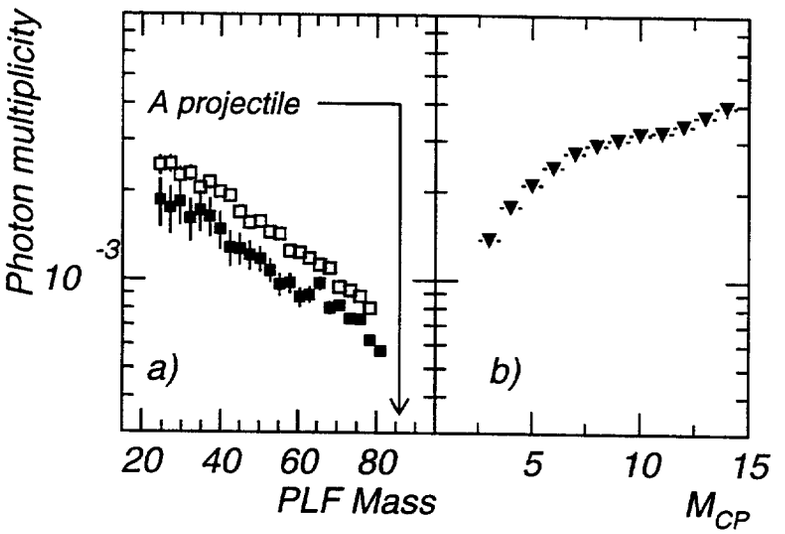

Fig. 13. *Dependence of the bremsstrahlung-photon multiplicity on a) the mass of the projectile like fragment with 90% (full squares) and 85% (open square) of the projectile velocity measured in the system $^{86}Kr+^{nat}Ni$ at 60A MeV and b) the charged-particle (proton and light ions) multiplicity.*

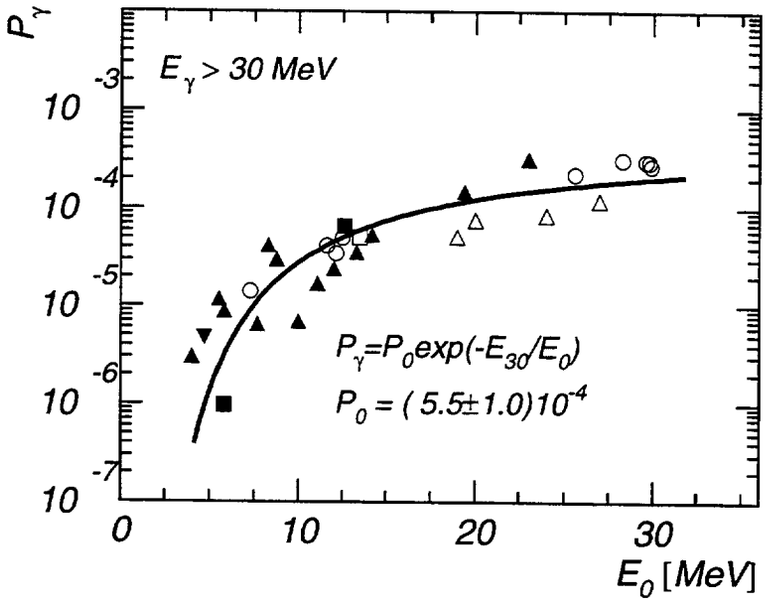

Fig. 14. *Variation of the bremsstrahlung-photon production probability with the slope of the photon spectrum measured for various systems and bombarding energies. Data are adapted from the systematics established in Ref. [4].*

the overlap of projectile and target, selects peripheral collisions. Based on the analysis of the systematics of bremsstrahlung-photon production [4], the cross section can be reduced to a single parameter, the probability P_γ to produce a bremsstrahlung photon per pn collision. This quantity only depends on the bombarding energy E_L:

$$\langle M_\gamma \rangle = \frac{\sigma_\gamma}{\sigma_R} = P_\gamma (E_L) \times \langle N_{pn} \rangle_b, \tag{27}$$

where σ_R is the total reaction cross section and $\langle N_{pn} \rangle_b$ the number of pn collisions averaged over the impact parameter. This number can be calculated with a geometric model [38] as the number of pn pairs present in the region of overlap between target and projectile nucleus. Since the slope E_0 of the photon spectrum is correlated with the bombarding energy (Fig. 21, Eq. (40)), we can replace the bombarding energy dependence of P_γ by its dependence on E_0 (Fig. 14). This dependence can be parametrized as:

$$P_\gamma (E_L) = P_0 \exp\left(-\frac{E_{30}}{E_0 (E_L)}\right), \tag{28}$$

where $E_{30} = 30$ MeV corresponds to the often used threshold for bremsstrahlung photons. At a fixed bombarding energy, E_0 varies with the impact parameter [39–43]. Assuming that the bremsstrahlung-photon production mechanism

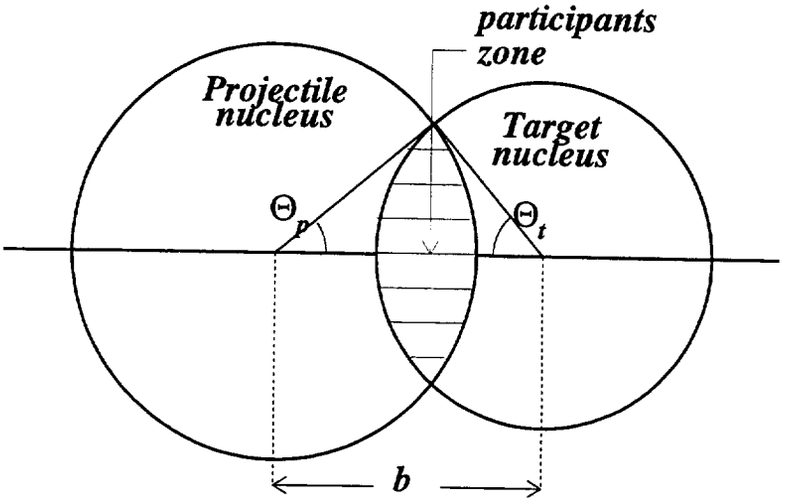

Fig. 15. *Definitions of the parameters used in the geometrical model.*

only reflects an energy dependence, P_γ reads:

$$P_\gamma\left(E_0\right) \equiv P_\gamma\left(b\right) = P_0 \exp\left(-\frac{E_{30}}{E_0\left(b\right)}\right). \tag{29}$$

Using Eq. (28) we calculate P_0 from the inclusive values E_0^{incl} and P_γ^{incl} measured at E_L. The dependence of P_γ on b, at a given bombarding energy E_L, can then be written as:

$$P_\gamma\left(b\right) = P_\gamma^{\text{incl}} \times \exp\left(\frac{E_{30}}{E_0^{\text{incl}}}\right) \times \exp\left(-\frac{E_{30}}{E_0\left(b\right)}\right), \tag{30}$$

where E_0^{incl} and $E_0\left(b\right)$ are experimental values. Similarly to Eq. (27) we can write the dependence of the photon multiplicity on b as:

$$M_\gamma(b) = P_\gamma\left(b\right) \times N_{pn}(b). \tag{31}$$

$N_{pn}(b)$ is calculated using the geometrical model (Fig. 15). In this approximation target and projectile nucleus are treated as homogeneous spheres so that the number of participants $A_f(b)$ for a given impact parameter scales as the volume at maximal geometric overlap. For a projectile nucleus (A_p, Z_p) bombarding a target nucleus (A_t, Z_t) at impact parameter b, the number of pn collisions (Fig. 16) is given by:

$$N_{pn}(b) = \frac{A_f(b)}{A_p A_t}\left(Z_p N_t + Z_t N_p\right), \tag{32}$$

$$A_f(b) = \frac{1}{4}A_p\left(2 - 3\cos\theta_p + \cos^3\theta_p\right) + \frac{1}{4}A_t\left(2 - 3\cos\theta_t + \cos^3\theta_t\right),$$

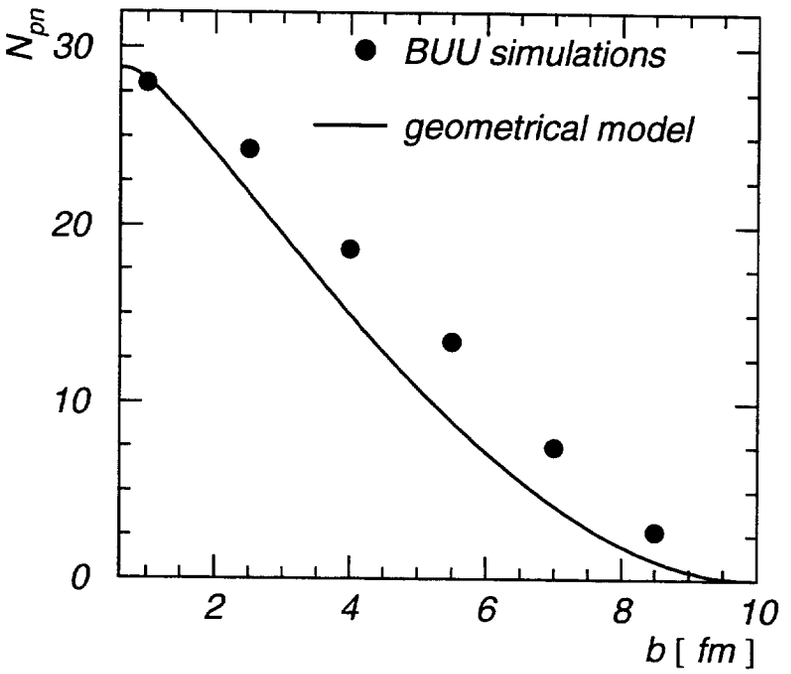

Fig. 16. *Variation of the number of pn collisions with the impact parameter b calculated using Eq. (32). Dots represent the number of first chance pn collisions calculated with BUU and downscaled by a factor 1.07 to normalize the result to the result of the geometrical model at b=1 fm. The system is* $^{86}Kr+^{58}Ni$.

$$\cos\theta_{p,t} = \frac{b^2 + R_{p,t}^2 - R_{t,p}^2}{2bR_{p,t}},$$

with $R_{p(t)}$ and $A_{p(t)}$ being the radius and the mass of the projectile (target) nucleus. The procedure to calculate the impact parameter is then the following:

(i) We select a class of events ν according to their charged-particle multiplicity (proton and light ions) or to the mass of the PLF or a combination of both and measure the number of events N_R^ν.

(ii) We measure the number of events of event class ν, N_γ^ν, in coincidence with hard photons extrapolated to 4π photon detection and the slope E_0^ν of the photon spectrum.

(iii) From the previous two values we calculate the number of *pn* collisions using Eq. (31,30):

$$N_{pn}^\nu = \frac{1}{P_\gamma^{\rm incl}} \frac{N_\gamma^\nu}{N_R^\nu} \times \exp\left(\frac{E_{30}}{E_0^\nu}\right) \times \exp\left(-\frac{E_{30}}{E_0^{\rm incl}}\right), \qquad (33)$$

(iv) We then deduce (Fig. 16) the impact parameter b corresponding to N_{pn}.

In Tab. 5 we list the various parameters that characterize the classes of events

A_{PLF}	M_{CP}	$M_\gamma \cdot 10^{-3}$	$E_0(MeV)$	N_{pn}	b(fm)
-	10	3.18 ± 0.12	17.5 ± 0.7	28.0 ± 1.0	1.0 ± 1.3
-	9	3.03 ± 0.10	18.4 ± 0.7	25.0 ± 1.0	2.0 ± 1.2
-	8	2.91 ± 0.10	18.2 ± 0.7	25.0 ± 1.0	2.1 ± 1.2
-	7	2.73 ± 0.09	18.7 ± 0.8	22.0 ± 1.0	2.7 ± 1.0
-	6	2.44 ± 0.08	18.7 ± 0.5	20.0 ± 1.0	3.3 ± 1.0
-	5	2.12 ± 0.07	18.2 ± 0.4	18.0 ± 0.7	3.8 ± 1.0
-	4	1.79 ± 0.06	17.3 ± 0.4	16.5 ± 0.6	4.1 ± 1.0
-	3	1.37 ± 0.04	17.6 ± 0.5	12.3 ± 0.4	5.3 ± 1.0
$20 < A_1 < 40$	-	2.24 ± 0.06	17.6 ± 0.8	20.0 ± 1.0	3.3 ± 0.8
$40 < A_1 < 60$	-	1.57 ± 0.03	17.2 ± 0.5	14.6 ± 0.6	4.6 ± 0.8
$60 < A_1 < 70$	-	1.19 ± 0.03	16.6 ± 0.7	11.8 ± 0.6	5.4 ± 0.8
$70 < A_1 < 80$	-	0.94 ± 0.02	16.9 ± 0.4	9.3 ± 0.4	6.2 ± 0.8
$60 < A_1 < 90$	0	0.53 ± 0.02	15.6 ± 0.7	5.8 ± 0.2	7.3 ± 0.8
$60 < A_1 < 90$	1	0.67 ± 0.02	15.5 ± 0.6	7.5 ± 0.2	6.7 ± 0.8
$60 < A_1 < 90$	2	0.86 ± 0.02	15.4 ± 0.5	9.7 ± 0.2	6.0 ± 0.8
$60 < A_1 < 90$	3	1.06 ± 0.03	16.7 ± 0.7	10.4 ± 0.4	5.8 ± 0.8
$60 < A_2 < 70$	-	0.87 ± 0.02	16.5 ± 0.3	8.7 ± 0.3	6.3 ± 0.8
$70 < A_2 < 80$	-	0.69 ± 0.02	16.0 ± 0.3	7.3 ± 0.3	6.8 ± 0.8
$80 < A_2 < 90$	-	0.58 ± 0.02	16.0 ± 0.7	6.1 ± 0.3	7.2 ± 0.8
$60 < A_2 < 90$	0	0.28 ± 0.02	13.5 ± 0.7	4.1 ± 0.2	8.0 ± 0.8
$60 < A_2 < 90$	1	0.44 ± 0.02	14.2 ± 0.7	5.8 ± 0.2	7.3 ± 0.8

Table 5

Conditions on the projectile like-fragment masses (the indices A_i with i = 1,2 correspond to the two different magnet settings $B\rho = 0.9$ and $0.85(B\rho)_{\text{beam}}$ of SPEG) and on the charged-particle multiplicities M_{CP} (proton and light ions) to select classes of exclusive events and the associated characteristics of the photon spectrum from which the impact parameter was deduced. The data were obtained for the system $^{86}Kr + {}^{\text{nat}}Ni$ at 60A MeV.

we have selected.

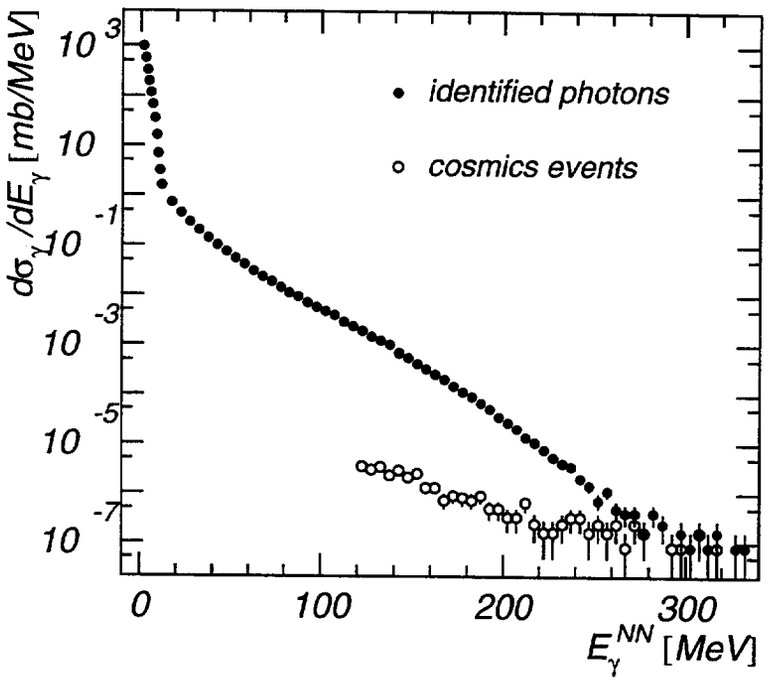

Fig. 17. *Photon spectrum measured with TAPS for the reaction* ^{86}Kr + ^{nat}Ni *at 60A MeV obtained by combining three spectra measured with three different trigger conditions (see text). Open circles represent cosmic-ray events not identified in the event-by-event analysis. Closed circles represent the photon spectrum with the contributions from cosmic-rays subtracted. The photon energy is calculated in the NN center-of-mass.*

6 INCLUSIVE PHOTONS

The photon spectrum, measured for the system Kr + Ni at 60A MeV (Fig. 17), covers the most extensive energy range ever obtained in this bombarding energy domain, from $E_\gamma^{NN} = 5$ up to 300 MeV, where E_γ^{NN} represents the photon energy calculated in the NN center-of-mass. The highest photon energy measured in this experiment is 10 times the energy available in a single NN collision and 15% of the total energy available in the AA center-of-mass. The cross section extends over 10 orders of magnitude which demonstrates the remarkable sensitivity of the experiment exploiting the performance of TAPS. This spectrum combines data measured with different trigger conditions. The low energy region ($E_\gamma < 50$ MeV) was obtained from data collected with the trigger "taps low" (see Tab. 3), the intermediate energy region (20 – 150 MeV) was associated with the trigger "γ", and finally the high energy part above 120 MeV was obtained with the trigger "highγ".

About 99% of all events induced by cosmic–rays were identified and rejected on an event-by-event basis (see § 4.1.8). A full analysis of events appearing in

the time-of-flight spectrum earlier than the prompt photon peak (see Fig. 9) removed the remaining 1%. The resulting spectrum (open circles in Fig. 17) was then subtracted from the photon spectrum.

Considering their origin, the spectrum of photons emitted in heavy-ion collisions can be sub-divided into three energy regions. For each of these regions different production mechanisms, which occur at different times of the collision, are dominant. The exponential distribution of low energy photons ($E_\gamma \leq$ 15 MeV), usually referred to as statistical photons, results from the final steps of the statistical deexcitation of the hot fragments formed in the reaction. It includes the γ-deexcitation of giant resonances, i.e. mainly the giant dipole resonance (GDR). Above the giant resonance domain, at about 20 MeV for the present system, hard photons constitute the high energy exponential distribution of bremsstrahlung photons. This part of the spectrum also includes photons originating from the decay of neutral pions. This last contribution to the hard photon spectrum is, however, weak at the bombarding energies under consideration, which are well below the threshold energy of 280 MeV for the pion production in free NN collisions.

Hard photons have their origin in the bremsstrahlung radiated in individual *pn* collisions. The bremsstrahlung spectrum exploits the energy available in each *pn* collision and builds up by adding to the beam momentum p_L the intrinsic nucleon momenta p_F due to the Fermi motion. An upper limit of the bremsstrahlung energy can therefore be calculated assuming a head-on, first chance *pn* collision, with the partners having the maximum intrinsic momentum of the Fermi-Dirac distribution, $p_F = 270$ MeV/c. The maximum energy available in the collision is then:

$$s_{\max} = 2\frac{[E_F(M_N + E_L) + p_F p_L]^2}{M_N(M_N + E_L)}, \tag{34}$$

where $E_F = \sqrt{M_N^2 + p_F^2}$, $E_L = \sqrt{M_N^2 + p_L^2} = T_L + M_N$, and T_L is the kinetic energy of the projectile. The highest photon energy which can be produced is given by:

$$E_\gamma^{\max} = \frac{s_{\max} - 4M_N^2}{2\sqrt{s_{\max}}}. \tag{35}$$

For the Kr+Ni system at 60A MeV this energy, which we shall call the kinematic limit, is equal to 194 MeV. The measured photon spectrum (Fig. 17) extends well beyond this limit. These very energetic photons can have several origins which will be discussed in details further on.

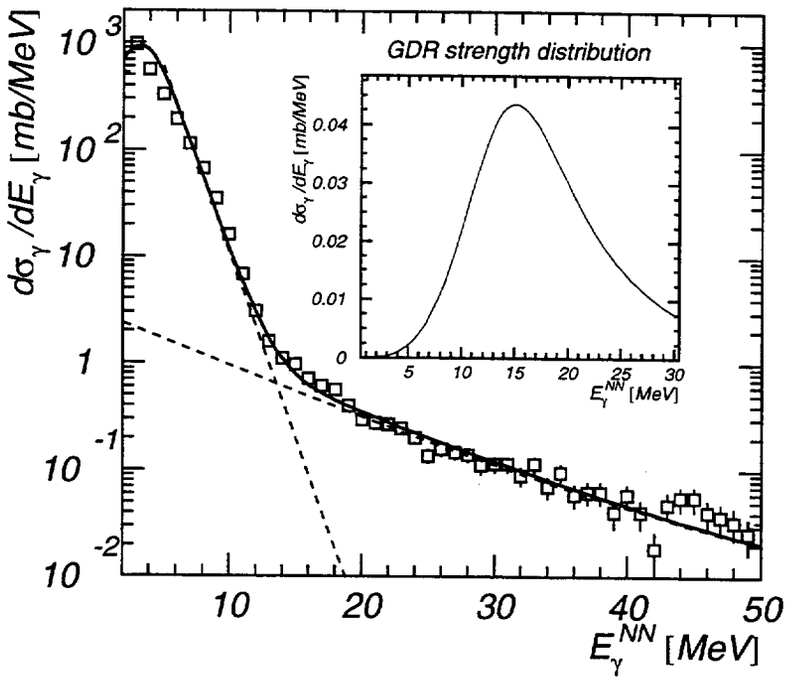

Fig. 18. *Photon spectrum measured with TAPS for the reaction* $^{86}Kr + {}^{nat}Ni$ *at 60A MeV and accumulated with the scaled-down "taps low" trigger. The solid line represents a parametrization according to Eq. (36) to the data. The dashed lines represent the statistical- and bremsstrahlung-photon spectra. The inset represents the estimated GDR strength distribution. The photon energy is calculated in the NN center-of-mass.*

6.1 Statistical photons

Since the primary goal of the experiments discussed in the present article was aimed at a detailed understanding of the origin of hard photons, the experimental parameters were tuned to optimize the detection of photons with energies above 20 MeV. Less energetic photons were, however, collected simultaneously but with moderate statistics (the corresponding trigger "taps low" was drastically scaled down).

The photon spectrum (Fig. 18) exhibits the exponential behavior of statistical photons from the lowest energy up to about 15 MeV. Above this energy the photon spectrum is dominated by the contribution from hard photons which can be mainly attributed to bremsstrahlung processes.

To describe the statistical distribution, the hard photon contribution was subtracted from the spectrum assuming a distribution in form of the sum of two exponentials. We shall see later that this shape describes best the hard photon spectrum. The remaining photons originate entirely from statistical decay of

A [MeV]	B [mb/MeV]	D [mb/MeV]	T_1 [MeV]	T_2 [MeV]	C [MeV]	G [MeV]
1.8	$8.9 \cdot 10^6$	0.37	1.25	8.3	15	15

Table 6
Parameters of Eq.(36) describing the statistical photon spectrum measured in the system ^{86}Kr+^{nat}Ni at 60A MeV.

excited fragments including the GDR strength. We have attempted to describe the spectrum by the empirical function established in Ref. [44]:

$$\frac{d\sigma}{dE_\gamma} = \left(\frac{E_\gamma - A}{E_\gamma}\right) B \exp\left(-\frac{E_\gamma}{T_1}\right) + \frac{E_\gamma^4 G^2}{\left(E_\gamma^2 - C^2\right)^2 + E_\gamma^2 G^2} D \exp\left(-\frac{E_\gamma}{T_2}\right), \tag{36}$$

where A, B, C, D, G, T_1, and T_2 are free parameters. This function describes the two physical processes playing the dominant role in the statistical decay. The first term represents the statistical decay of particle-bound states and the second term represents the decay of states at higher excitation energies including the decay of GDR states. The comparison of Eq. (36) with CASCADE [45] calculated spectra for bombarding energies below $20A$ MeV indicates that the parameters C and G are only an approximation within 5-10% of the shape parameters, energy and width, of the GDR. Obviously, in view of the limited resolution of our data set, it was not possible to fit with a χ^2 method Eq. (36) to the measured spectrum (Fig. 18). First we subtracted the bremsstrahlung part form the raw spectrum. The adjustment was then performed considering the two terms of Eq. (36) separately, fitting first the low energy part and then the GDR part to the difference between the raw spectrum and the estimated low energy exponential. Therefore the extracted values are given (Tab. 6) without uncertainty and should be considered only as indicative. We find that the GDR strength is much weaker than the bremsstrahlung photon cross-section and would correspond, according to CASCADE calculations, to rather low excitation energies (about $1A$ MeV). This weak strength and its distribution, broader than the natural width of the GDR, could also be explained by the excitation of GDR in several hot fragments, with a broad distribution of masses [46], associated with a possible quenching of the GDR strength, as it was observed at high excitation energies [47].

6.2 Bremsstrahlung photons

At intermediate bombarding energies hard photons defined as photons with energies above the Giant Dipole Resonance domain, i.e. above approximately 20-30 MeV, originate exclusively from bremsstrahlung emitted in individual *pn* collisions, and from the two-photon decay of neutral pions. This is true only up to the kinematic limit defined by Eq. (35) above which new mechanisms producing photons start to play the dominant role. At the bombarding energies under consideration (below $60A$ MeV) the π^0 contribution to the single-photon spectrum can be safely neglected. We determined it to be less than 3% at $60A$ MeV and 0.02% at $40A$ MeV.

BUU-calculations presented in (§ 2) predict for the reactions studied that the bremsstrahlung photons are emitted from two distinct sources. The first and dominant one is associated with the initial phase of the heavy-ion reaction as a result of first-chance *pn* collisions. The second one originates from the second compression phase in a later stage of the reaction when the di-nuclear system is thermalizing and it results from secondary *pn* collisions. The existence of these two distinct sources can be identified taking advantage of the expected differences in their emission pattern.

6.2.1 Energy spectrum

From the BUU predictions direct and thermal photons should exhibit different spectral shapes: thermal photons give rise to a softer energy spectrum than direct ones. Folding the elementary cross section (Fig. 40) with the intrinsic momentum distribution of participant nucleons leads in the NN system to a distribution close to exponential with a cutoff in the vicinity of the kinematic limit [Eq. (35)]. It can be described by the function:

$$\frac{d\sigma}{dE_\gamma} = K \exp\left(-\frac{E_\gamma}{E_0}\right). \tag{37}$$

The slope parameter E_0 depends on the bombarding energy and on the average intrinsic momentum of the participant nucleons. As less energy is available on average in second chance *pn* collisions than in first-chance collisions because most of the projectile kinetic energy is damped, the thermal-photon spectrum is softer. In presence of an emission from two sources with the characteristics predicted by BUU calculations, we expect an empirical photon spectrum of the form:

$$\frac{d\sigma}{dE_\gamma} = K_d \exp\left(-\frac{E_\gamma}{E_0^d}\right) + K_t \exp\left(-\frac{E_\gamma}{E_0^t}\right), \tag{38}$$

with the constant K defined by:

$$I_{d,t} = K_{d,t} \int_{E_{30}}^{\infty} \exp\left(-\frac{E_\gamma}{E_0^{d,t}}\right) dE_\gamma = K_{d,t} E_0^{d,t} \exp\left(-\frac{E_{30}}{E_0^{d,t}}\right), \tag{39}$$

$I_{d,t}$ represents the intensity of each photon source, d stands for direct and t for thermal. So far the presence in the photon spectrum of two exponential distributions was overlooked because of experimental limitations which restricted the measurement of photon spectra only to a too narrow energy domain. To our knowledge there are two exceptions where the photon spectrum was measured up to rather high energies: 120 MeV at a bombarding energy of $40A$ MeV [48] and 160 MeV at $35A$ MeV [49]. In both measurements, the two exponential components are clearly visible. In the first experiment, data were compared to calculations considering *pn* bremsstrahlung from a thermal source. These calculations correctly reproduce the low energy part of the spectrum (where we locate thermal photons) but underpredicts the high energy part. We attribute the excess to direct photons. Reversely, in the second experiment an extended version of the nucleon exchange transport model [50] was used to calculate the photon spectrum. This model includes only direct photons and reproduces the high energy part of the photon spectrum but fails to reproduce the photon yield below 50 MeV. The excess production of photons in this energy range was tentatively attributed to statistical photons.

For all three systems we have studied photon spectra measured over the energy range where bremsstrahlung photons dominate (Fig. 19) and corresponding to the "γ" trigger selection (see Tab. 3). Fitting a single exponential function to the data gives a good description of the high energy part of the spectrum only. As a matter of fact a strong excess with an exponential slope is observed below 50 MeV. This excess cannot be attributed to the tail of the GDR strength distribution because it would imply a much too large cross section and temperature in contradiction with our analysis of statistical GDR photons and with the observation of the GDR quenching observed at lower bombarding energies [47]. Fitting the two component function [Eq. (38)] to the data provides a better description. The fit parameters are reported in Tab. 7.

A different way to identify the presence of two slopes is provided by the local slope analysis. The local slope is deduced from a fit performed over a constant energy range and by moving the centroid along the spectrum. Assuming a purely exponential spectrum, the slope parameter obtained in any local fit equals the global slope. In the case of two exponential components having different slopes E_1 and E_2, the local fit performed in the low energy part of the spectrum yields a value intermediate between E_1 and E_2. Moving to higher energies results in an increase of the slope value up to a maximum value equal to E_2. However, if the process related to the second slope is constrained by

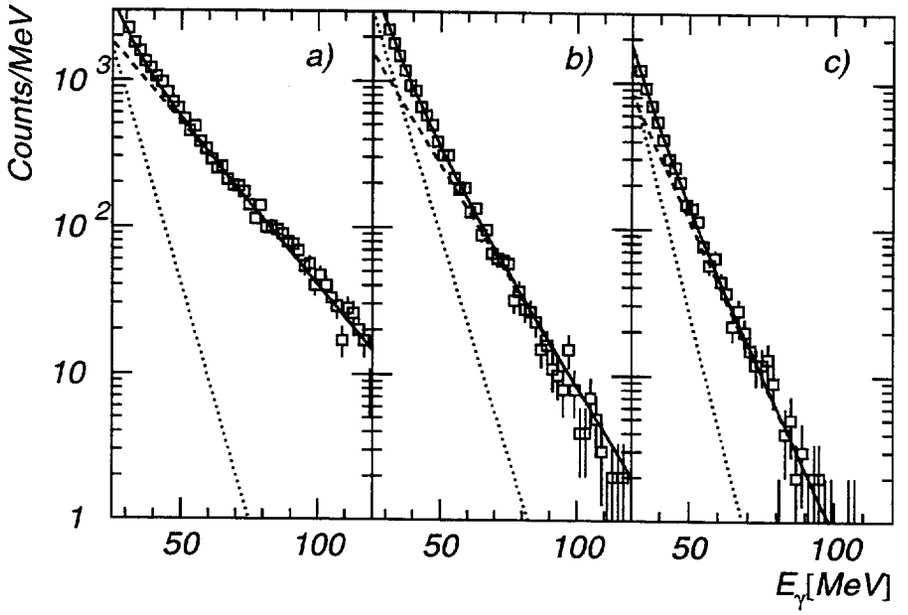

Fig. 19. *Photon spectra measured at $\theta = 90^0$ for the reactions a) $^{86}Kr + {}^{nat}Ni$ at 60A MeV b) $^{181}Ta + {}^{197}Au$ at 40A MeV and c) $^{208}Pb + {}^{nat}Au$ at 30A MeV. Solid lines represent the fit of Eq. (38), dashed lines the direct photon component and dotted lines the thermal photon one.*

system	I_d/I_t	E_0^d (MeV)	E_0^t (MeV)
Kr+Ni 60A MeV	3.0 ± 0.5	20.2 ± 0.4	8.5 ± 0.8
Ta+Au 40A MeV	2.0 ± 0.6	13.4 ± 0.8	6.9 ± 0.6
Pb+Au 30A MeV	1.6 ± 0.5	10.1 ± 0.4	5.5 ± 0.6

Table 7
Parameters for the fit of Eq. (38) to the double differential cross section of hard photons ($E_\gamma \geq 30$ MeV, $\theta = 90^0$) measured in the three systems studied.

energy limitations, like the kinematic limit, its yield close to this threshold is significantly reduced. In this case the local slope will drop when approaching the threshold. We have analyzed with this method the spectra measured for the Kr+Ni and Ta+Au systems (Fig. 20). In both cases the local slopes increase and reach an almost constant value indicating the presence of two components. At higher energies, specifically in the case of Kr+Ni, the local slope values fall quite rapidly, indicating the influence of the kinematical limit. This measured evolution can quite well be described (Fig. 20) by assuming two-component exponential spectra with slopes and intensities from Tab. 7 and by applying a simple reduction of the high energy yield.

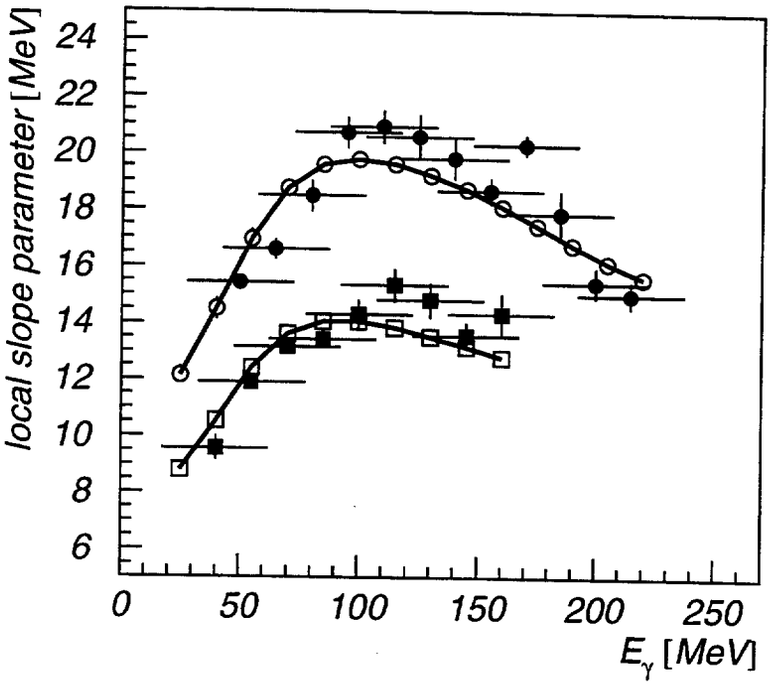

Fig. 20. *Local slope parameters for the experimental photon spectra for the Kr+Ni reaction at 60A MeV (full circles) and for Ta+Au at 40A MeV (full squares). The horizontal bars indicate the fitting range. The open symbols were obtained for two-component spectra with slopes and intensities reported in Tab. 7 together with the yield reduction close to the kinematical threshold.*

As a first conclusion we find that the hardest spectral distribution is characterized by a slope parameter (E_0^d) which follows the trend (Fig. 21) of the variation of E_0 with the reduced bombarding energy ($E_{cc} = E_L - V_c/A_p$ with E_L the bombarding energy, V_c the Coulomb barrier and A_p the projectile mass). The average dependence is described by:

$$E_0 = 0.68 \cdot E_{cc}^{0.83}. \tag{40}$$

The ratio between the value of the two slopes equals 2, a value similar to what BUU calculations predict (Fig. 22). The second conclusion concerns the relative intensities measured for the three systems. The direct photon source is by a factor 3 more intense than the thermal one in the Kr+Ni system measured at 60A MeV. This is at variance with the systems measured at lower bombarding energies for which this factor drops to two or even less. This change is well explained by the BUU calculations as the force driving the second compression is progressively counterbalanced by the expansion force with increasing bombarding energy. A change in the relative intensity of thermal and direct photons should also be observed when varying the impact parameter. One expects relatively more thermal photons in central than peripheral collisions

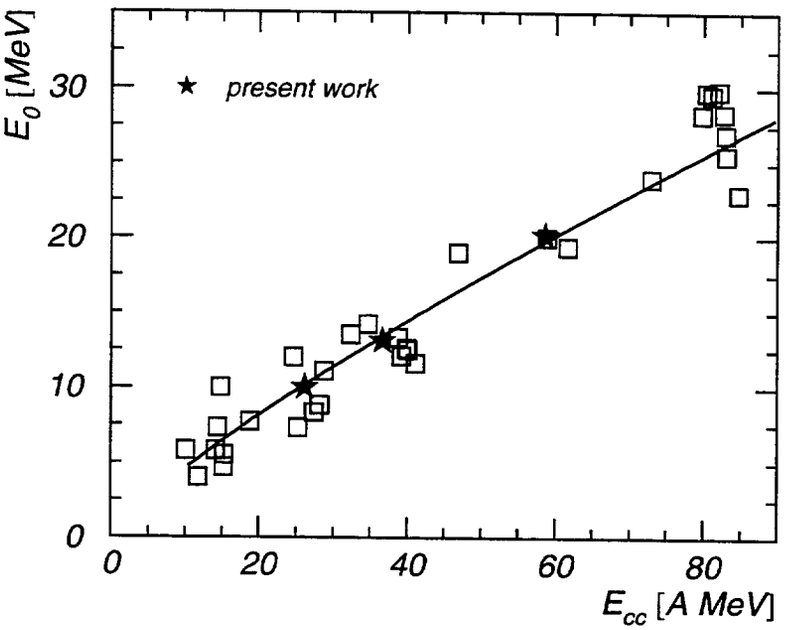

Fig. 21. *Compilation of measured slope parameters, taken from Ref. [4], plotted as a function of the bombarding energy minus the Coulomb barrier energy. Our data (inclusive E_0^d) are represented by the symbol ⋆. The solid line represents a fit of Eq.(40) to the data.*

impact parameter	I_d/I_t	E_0^d (MeV)	E_0^t (MeV)
inclusive	3.0 ± 0.5	20.2 ± 0.4	8.5 ± 0.8
peripheral $b > 5$fm	3.0 ± 0.6	18.7 ± 0.9	7.3 ± 1.5
central $b < 5$fm	2.1 ± 0.5	22.7 ± 0.9	9.8 ± 1.0

Table 8
Parameters for the fit of Eq. (38) to the double differential cross section of hard photons ($E_\gamma \geq 30$ MeV, $\theta = 90^0$) measured in inclusive, peripheral and central reactions of the system ^{86}Kr+$^{\text{nat}}Ni$ at 60A MeV.

reflecting the higher densities reached in central collisions. We have therefore constructed two exclusive photon spectra (Fig. 22) measured in the reaction Kr+Ni at 60A MeV and associated with different impact parameters (see § 5). The first one corresponds to central collisions with $b < 5$ fm, and the second one to peripheral collisions with $b > 5$ fm. Eq. (38) was fitted to these spectra and the resulting parameters are reported in Tab. 8. We observe that the slope parameters are modified so that the softer spectra are obtained in peripheral collisions. This behavior was already well established [39–43] and its origin results from changes of the phase-space population. The relative intensities of

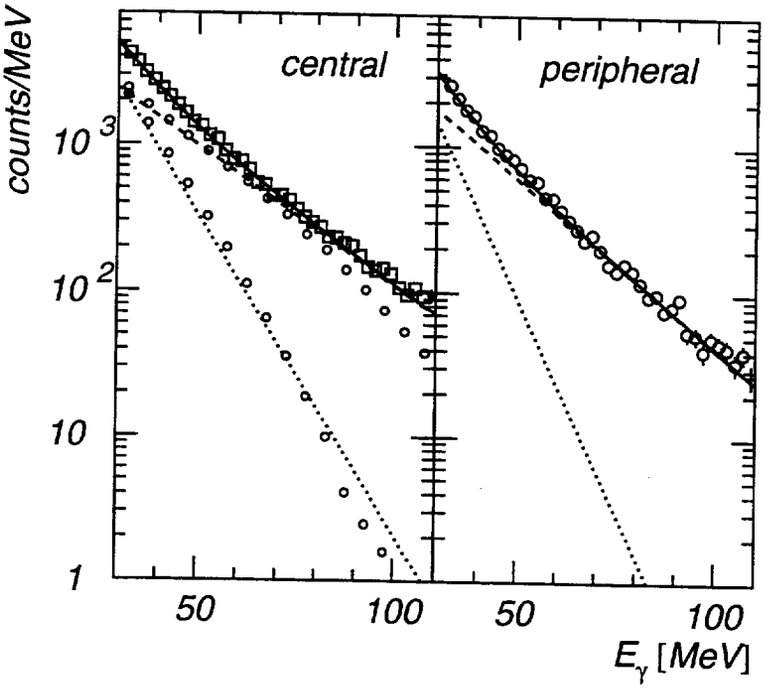

Fig. 22. *Hard-photon energy spectra measured for the reaction* $^{86}Kr + {}^{nat}Ni$ *at 60A MeV for central collisions* $b < 5$ *fm and peripheral collisions* $b > 5$ *fm. The solid line is the result of the fit of Eq. (38). The dotted and dashed lines represent the two components of Eq. (38). The circles represent the result of a BUU calculation at b=0 fm.*

the two exponential distributions follow the expectation that relatively more thermal photons are produced in central collisions.

6.2.2 *Angular distributions*

Direct photons, originating from first-chance *pn* collisions have a characteristic angular distribution that due to the Doppler shift is peaked in the laboratory in the direction of the projectile. The Doppler effect can be exploited to measure the photon-source velocity. If the picture of the first chance *pn* collisions is valid this velocity should be equal to the NN center-of-mass velocity, $\beta_{\mathrm{NN}} = \beta_{\mathrm{proj}}/2$. Because of the nature of the elementary process producing bremsstrahlung in the *pn* rest frame, the angular distribution partly has a dipole character and partly an isotropic component. The dipole component is emitted when the proton is slowed down before scattering on the neutron and the isotropic emission takes place when the proton is re-accelerated after being scattered in a random direction. The double differential cross-section, $d^2\sigma/dEd\Omega$, can thus be written in the source frame [51] as:

$$\frac{d^2\sigma}{dE_s d\Omega_s} = \frac{K}{Z}\left(1 - \alpha\cos^2\theta_s\right)\exp\left(-\frac{E_s}{E_0}\right), \tag{41}$$

where θ_s and E_s are the polar angle and the energy of the photon in the source frame. Denoting β_s the source velocity and γ_s the related Lorentz factor, in the laboratory frame the Lorentz-boosted photon angular distribution is:

$$\frac{d^2\sigma}{dE_L d\Omega_L} = \frac{K}{Z}\left(1 - \alpha + \alpha\frac{\sin^2\theta_L}{Z^2}\right)\exp\left(-\frac{ZE_L}{E_0}\right), \tag{42}$$
$$Z = \gamma_s\left(1 - \beta_s\cos\theta_L\right).$$

where θ_L and E_L are respectively the measured polar angle and energy of the photon in the laboratory.

To construct the angular distributions, the angular acceptance of TAPS was calculated from GEANT simulations. The simulations were performed by generating hard photons with the experimentally determined energy and angular distribution. The energy deposited in each module, calculated by GEANT, was then analyzed with the same algorithm that was used for the data. From the simulated polar-angle distribution we deduced the acceptance used to correct the experimental angular distribution. Eq. (42) was fitted to the angular distributions (Fig. 23), measured for photons with energy above 30 MeV, with K, E_0, β_s, and α as free parameters and which values are listed in Tab. 9. We find back the slope parameters reported in Tab. 7 and extracted from the photon spectra measured at $\theta_{\mathrm{lab}} = 90^0$. The source velocity, β_s, is compatible with the NN center-of-mass velocity for the three systems, although the AA center-of-mass velocity is not that different in these almost symmetric systems. These two parameters indicate that photons beyond 30 MeV originate predominantly from bremsstrahlung in first-chance *pn* collisions. The photon

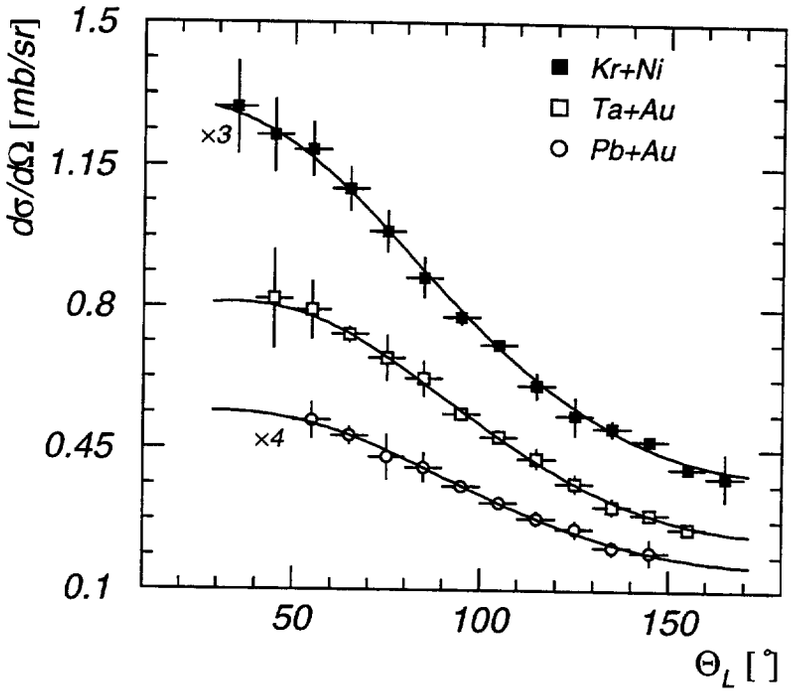

Fig. 23. *Angular distribution measured in the laboratory frame for photons above 50 MeV emitted in the reaction ^{86}Kr + ^{nat}Ni at 60A MeV, ^{181}Ta + ^{197}Au at 40A MeV and ^{208}Pb + ^{197}Au at 30A MeV. Solid lines represent the fit of Eq. (42) to the data.*

parameter	system		
	Kr+Ni 60A MeV	Ta+Au 40A MeV	Pb+Au 30A MeV
K [mb/sr/MeV]	0.065 ± 0.007	0.46 ± 0.05	0.2 ± 0.02
E_0 [MeV]	20.2 ± 0.3	13.1 ± 0.4	10.0 ± 0.5
β_s	0.174 ± 0.009	0.140 ± 0.009	0.12 ± 0.01
α	0.18 ± 0.04	0.27 ± 0.05	0.24 ± 0.12
β_{NN}	0.177	0.144	0.125
β_{AA}	0.209	0.138	0.129
σ_γ [mb]	3.5 ± 0.4	6.9 ± 0.7	1.14 ± 0.11
$\langle N_{pn} \rangle_b$	7	18	19
$P_\gamma (\times 10^5)$	11.5 ± 1.2	5.4 ± 0.5	0.82 ± 0.08

Table 9
Parameters characterizing the photon production in the three systems studied.

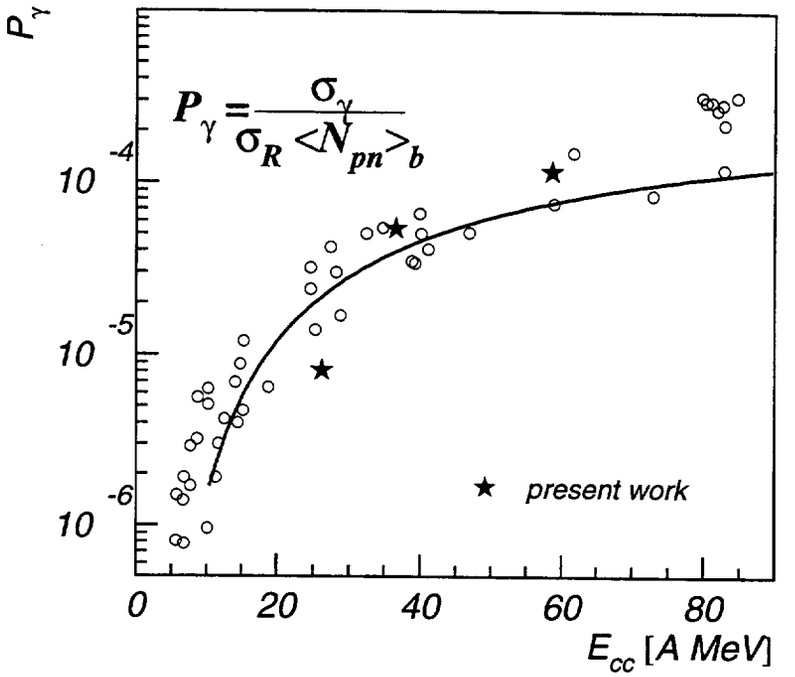

Fig. 24. *Systematics of measured photon emission probability per pn collision adapted from Ref. [4], as a function of the bombarding energy minus the Coulomb barrier energy. Our data are represented by stars. Solid line represents Eq. (44).*

emission probability per *pn* collision is calculated [Eq. (27)] with the following parametrization of the total reaction cross-section [4]:

$$\sigma_R[mb] = 10\pi \left\{1.16 \left(A_p^{1/3} + A_t^{1/3} + 2.0\right)\right\}^2 \left(1 - \frac{V_c}{E_L}\right). \tag{43}$$

The number of *pn* collisions in the heavy-ion reaction is calculated using the geometrical equal-participant model [38] (see § 5) and is reported in Tab. 9. From σ_γ (obtained by integrating Eq. (41) over the photon energy above 30 MeV and over the solid angle) we have calculated the values of P_γ also reported in Tab. 9. Its dependence on the reduced bombarding energy E_{cc} (Fig. 24) can be parametrized by the function:

$$P_\gamma = 5 \cdot 10^{-4} \cdot \exp\left(-\frac{E_{30}}{E_0}\right), \tag{44}$$

where the E_0 dependence with E_{cc} is given by Eq. (40). We observe a noticeable dispersion, somewhat smoothed out by the logarithmic representation, in the values measured at the same energy, which might be attributed to changes in the reaction dynamics when the entrance channel system changes. It might also be linked to the fact that P_γ does not scale exactly with the number of

pn collisions as was established recently [52]. Different scalings consequently have been proposed [53].

The angular distribution for thermal photons should exhibit a behavior different from the one for direct photons. First it should tend towards an isotropic angular distribution ($\alpha \rightarrow 0$) as thermal photons are emitted in second chance *pn* collisions when the memory of the initial direction of the projectile is lost. Second, since thermal photons are emitted from an almost equilibrated dinuclear system, the source velocity should be equal to the AA center-of-mass velocity of this system. A first attempt to measure the angular distribution as a function of the centrality of the collision was performed [54] for the system ^{36}Ar + ^{197}Au at 95A MeV. The hard-photon source velocity was indeed found to be sizably smaller than the NN velocity, except for very peripheral collisions. This is the first indication that photon emission is not solely dominated by first-chance *pn* collisions, but carries also information on the later, stopping phase of the reaction.

Because the three systems we have measured are nearly symmetric, the two velocities β_{NN} and β_{AA} are almost equal (see Tab. 9) and cannot be resolved experimentally. The situation becomes even more complicated as between 20 and 50 MeV at most 50% of the total amount of photons have thermal origin. We therefore considered to search for a change by analyzing the ratio of angular distributions integrated over two different energy domains, N_γ^1 and N_γ^2, where the thermal versus direct photon composition is also different:

$$
\begin{aligned}
N_\gamma^1 &= \int_{E_3}^{E_4} \frac{d\sigma}{d\Omega_{\mathrm{NN}}} dE, \\
N_\gamma^2 &= \int_{E_1}^{E_2} \frac{d\sigma}{d\Omega_{\mathrm{NN}}} dE, \\
\frac{N_\gamma^1}{N_\gamma^2} &= \frac{d\sigma_t/d\Omega_{\mathrm{NN}} + d\sigma_d/d\Omega_{\mathrm{NN}}}{d\sigma_d/d\Omega_{\mathrm{NN}}}.
\end{aligned}
\tag{45}
$$

In the numerator we consider to have a mixed contribution and in the denominator we have only direct photons. The angular distribution of direct photons in the NN center-of-mass [Eq. (41)] and integrated between E_1 and E_2 reads:

$$
\begin{aligned}
\frac{d\sigma_d}{d\Omega_{\mathrm{NN}}} &= I_d \left(1 + \alpha \sin^2\theta\right), \\
I_d &= K_d E_0^d \left[\exp\left(-\frac{E_1}{E_0^d}\right) - \exp\left(-\frac{E_2}{E_0^d}\right)\right].
\end{aligned}
\tag{46}
$$

In its center-of-mass frame the thermal emission is isotropic:

$$\frac{d^2\sigma_t}{dE_\gamma d\Omega_{\rm CM}} = K_t \exp\left(-\frac{E_\gamma}{E_0^t}\right), \tag{47}$$

which when integrated between E_3 and E_4 in the NN reference results in:

$$\frac{d\sigma_t}{d\Omega_{\rm NN}} = \frac{K_t E_0^t}{Z^2}\left[\exp\left(-\frac{ZE_3}{E_0^t}\right) - \exp\left(-\frac{ZE_4}{E_0^t}\right)\right], \tag{48}$$
$$Z = \gamma_{\rm rel}\left(1 - \beta_{\rm rel}\cos\theta_{\rm NN}\right),$$

where $\beta_{\rm rel}$ is the relative velocity between the direct-photon source and the thermal-photon source.

The ratio (Fig. 25) was constructed for the system Kr+Ni at 60A MeV only because the entrance channel asymmetry should provide the largest value for $\beta_{\rm rel}$. The denominator of Eq. (45) was obtained by integrating between 40 MeV and 80 MeV. In the upper panel of Fig. 25 the numerator was obtained by integrating between 20 MeV and 40 MeV and in the lower panel between 80 MeV and 120 MeV. As expected we find that the ratio is constant when direct photons build up both numerator and denominator (bottom of Fig. 25) but rises at small angles when the denominator contains also thermal photons (top of Fig. 25). The shape is compatible with a relative velocity equal to $\beta_{\rm rel} = 0.04$ which corresponds to the velocity of the AA center-of-mass seen from the NN center-of-mass, $\beta_{\rm rel} \sim \beta_{\rm AA} - \beta_{\rm NN}$. This observation indicates that the angular distribution changes when going from high energy photons to low energy photons and the change is compatible if one adds photons emitted from a system moving at the AA center-of-mass velocity. The latter confirms that the low energy part of the hard photon spectrum contains direct and thermal photons.

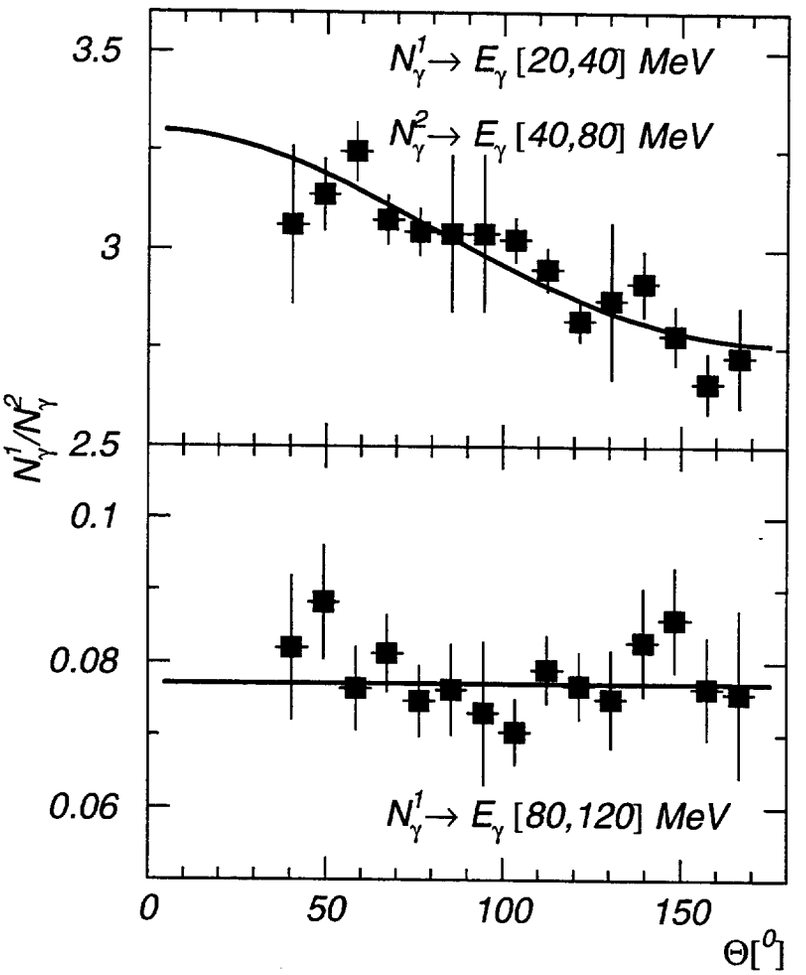

Fig. 25. *Ratio of angular distributions measured for bremsstrahlung-photons in the reaction Kr + Ni at 60A MeV. The denominator is obtained by integrating the double differential cross section [Eq. 45] between 40 MeV and 80 MeV. The angular distribution in the numerator is obtained by integrating between 20 MeV and 40 MeV (top) and between 80 MeV and 120 MeV (bottom). Solid lines represent the fit as described in the text.*

7 HARD PHOTON INTERFEROMETRY

In analogy to the Hanbury-Brown and Twiss (HBT) method [55] in astronomy intensity interferometry between pairs of identical particles is extensively being used to analyze the space-time extent of the particle emitting source. The interference arises from the indistinguishability of the two identical particles and the symmetrization of the two-particle wave function [56]. The method consists in measuring the two-particle coincidence rate to evaluate the relative-momentum correlation revealing the interference pattern. Although widely used in nuclear [57] and particle [58] physics, the HBT method was never applied successfully to photons previous to the present work, mainly because of their extremely weak production rate compared to the overwhelming hadron production. It is, however, well worth the effort since photons are the best suited probe for interference measurements, as photons are not subject to final state interactions, and since they convey the true image of the production source being unaffected by the traversed nuclear medium. Detailed information of two-photon interferometry in nuclear physics can be found in Refs. [59,60].

7.1 Correlation functions

In heavy-ion collisions and at the bombarding energies under consideration, photon pairs are produced via two different mechanisms. The first one is the decay of neutral pions and the second one corresponds to the emission of bremsstrahlung photons from two distinct *pn* collisions. The cross section, $\sigma_{\gamma\gamma}$, for simultaneous but independent emission of two bremsstrahlung photons can be estimated by generalizing the expression for the inclusive cross section [Eq. (27)]:

$$\sigma_{\gamma\gamma} = \sigma_R \langle N_{pn}(N_{pn}-1)\rangle_b P_\gamma^2, \tag{49}$$

where the averaged quantity $\langle N_{pn}(N_{pn}-1)\rangle_b$ is calculated with the geometrical model. Using the value for P_γ obtained from the inclusive photon production (see Tab. 9) we find $\sigma_{\gamma\gamma} = 6 \pm 1$ μb for the Kr+Ni system at $60A$ MeV and 16 ± 3 μb for the Ta+Au system at $40A$ MeV. These numbers have to be compared with the cross-sections that we have measured for neutral pion production, 42 ± 4 and 2.2 ± 0.3 μb respectively (see section 9). Although photon pairs stemming from π^0 decay are expected to be, at $60A$ MeV, about ten times more abundant than bremsstrahlung-photon pairs, they can rather easily be distinguished due to the good momentum resolution of TAPS. This can be visualized in the invariant mass spectrum (Fig. 26) defined by Eq. (13). The invariant mass spectrum was constructed from events containing at least two photons with energy above 25 MeV calculated in the NN center-of-mass sys-

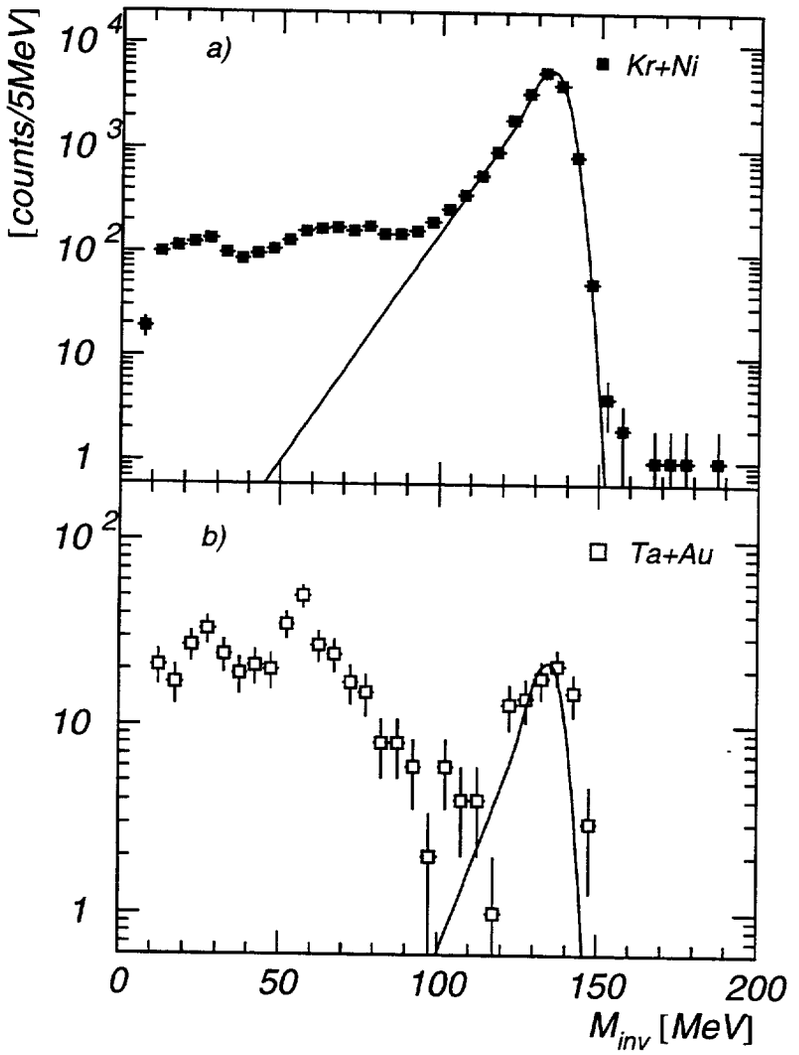

Fig. 26. *Invariant mass spectrum, not corrected for the detection acceptance, measured for the reactions a)* $^{86}Kr + {}^{nat}Ni$ *at 60A MeV and b)* $^{181}Ta + {}^{197}Au$ *at 40A MeV. The solid line describes* π^0 *contribution estimated from GEANT simulations.*

tem. These events were selected with the triggers "2γ" and "$\gamma\gamma$" (see Tab. 3). The cosmic ray events were eliminated by selecting showers according to their profile geometry (see § 4.1.8 and Refs. [22,36]). An optimum shower collection was achieved by reducing the fiducial volume with the surface condition [Eq. (17)] $\mathcal{S} < 0.8$. In order to distinguish real pairs of photons from false ones generated by a single high energy photon whose shower has developed in non–adjacent modules (discontinuous shower) [22], we have required a minimum relative angle of $\theta_{12}^{min} = 8.3°$. The spectrum was not corrected for the momentum acceptance of TAPS.

System	Number of pairs					
	photon	cross section $[\mu b]$	cosmic ray	di-electron	split shower	random
Kr + Ni	1900	6.6 ± 0.8	3	< 5	< 46	6
Ta + Au	370	16 ± 2	5	< 6	< 48	5

Table 10
Bremsstrahlung photon and π^0 contribution measured in the systems $^{86}Kr + {}^{nat}Ni$ at 60A MeV, $^{181}Ta + {}^{197}Au$ at 40A MeV and $^{208}Pb + {}^{197}Au$ at 30A MeV. The contribution of false pairs generated by known sources is also reported.

The invariant mass distribution of π^0 was deduced from GEANT simulations including the detector and the analysis algorithm response. Below 80 MeV the π^0 contribution is negligible. The resulting number of photon pairs are reported in Tab. 10 together with the corresponding cross sections. We find that the estimate obtained from Eq. (49) agrees with the measured cross sections. Other sources of photon pairs could still contaminate the spectrum. A first source of false pairs is provided by random coincidences when two photons emitted in two distinct reactions occurring in the same beam pulse are detected simultaneously. Their production is estimated by:

$$N_{\gamma\gamma}^{\text{random}} = n_{\text{pulses}} P_{RR} M_\gamma^2 \epsilon_{\gamma\gamma}, \tag{50}$$

where $P_{RR} = 4 \cdot 10^{-4}$ is the probability to have two reactions per beam pulse, n_{pulses} the total number of beam pulses accumulated during the experiment, and $\epsilon_{\gamma\gamma}$ the probability to detect two photons. Other sources of false pairs like di-electrons, discontinuous showers, and cosmic muons are mostly eliminated by the shower reconstruction algorithm. The numbers of false pairs which might still be present in the set of photon pair data have been estimated for each source and are reported in Tab. 10. Details on how these estimations were obtained can be found in Ref. [22].

The correlation is experimentally defined as:

$$C_{12}(k_1, k_2) = \frac{P_2(k_1, k_2)}{P_1(k_1) \times P_1(k_2)}, \tag{51}$$

where $P_{1(2)}$ is the probability to detect one (two) photon and k the four-momentum. The correlation function is thus defined as the ratio between two-photon events and one-photon events. It is a function of the relative four-momentum and can be evaluated in the four-dimensional space. However, because of the usually limited statistics available for the construction of the numerator, the correlation function is represented in one dimension only.

For photons, the most convenient variable is the invariant four-momentum, Q, defined by Eq. (13). This choice is guided by the fact that this variable, which for photons is also the invariant mass, allows an unambiguous identification of neutral pions. Relying on GEANT Monte-Carlo simulations, we have demonstrated [60] that, owing to the photon kinematics, the projection from the four- to the one-dimensional space only slightly distorts the correlation function.

The construction of the denominator has generated in the past many discussions [61–63] and in particular the question of the distortions in the presence of a resonance like π^0. We have chosen to construct the denominator from the set of singles data by associating photons from distinct events. The advantages of selecting single photon events are twofold: first, they provide extremely good statistics and thus a well defined uncorrelated spectrum, and second, at the bombarding energies under consideration the neutral pion contribution can be neglected. This method must of course include exactly the bias of true photon pairs in the numerator and must represent the same class of reactions. The first condition is achieved by submitting the mixed pair events to the same analysis as true pair events. The second condition is fulfilled since triggers "γ" and "2γ" or "$\gamma\gamma$" contain the same condition on FW multiplicity.

Theoretically, the correlation function of photons emitted from an incoherent source is related to the Fourier transform, $\varrho(k)$, of the source density distribution [58], $\rho(r)$:

$$C_{12}(k_1, k_2) = 1 + \lambda \left|\varrho(k_1, k_2)\right|^2 , \tag{52}$$

where λ is a parameter added *ad hoc* to take into account various effects like partial coherence of the source, dynamics of the photon emission [64,65], and left-over false pairs. However it is necessary, to know *a priori* the shape of ρ, usually postulated to be Gaussian:

$$\rho(r,t) = \rho_0 \exp\left(-\frac{r^2}{2R_G^2}\right) \exp\left(-\frac{t^2}{2\tau^2}\right), \tag{53}$$

where R_G is the spatial Gaussian radius of the source and τ its lifetime. The Fourier transform takes the form ($\hbar = c = 1$):

$$\varrho(q, q_0) = \exp\left(-\frac{q^2 R_G^2 + q_0^2 \tau^2}{2}\right), \tag{54}$$

where q and q_0 are respectively the relative momentum and energy. As mentioned earlier, because of technical difficulties the experimental correlation

function can only be calculated with the present data in a one-dimensional space like Q. The projection of Eq. (52) writes:

$$C_{12}(Q) = 1 + \lambda \left|\varrho(Q)\right|^2 = 1 + \lambda \exp\left(-\frac{Q^2R^2}{2}\right). \tag{55}$$

Comparing Eqs. (54) and (55) and using the definition of the relative four-momentum given in Eq. (13), one can relate [66] the parameter R to the spatial and temporal extent of the source:

$$Q^2R^2 = q^2R_G^2 + q_0^2\tau^2, \qquad R = R_G \times \sqrt{\frac{1 + (\tau/R_G)^2(q_0/q)^2}{1 - (q_0/q)^2}}. \tag{56}$$

We have checked [22,60] with the help of GEANT Monte-Carlo simulations that for photons, where $q_0 \ll q$, R is a good approximation of the spatial radius R_G. The value of λ is, however, modified but this has no influence on the interpretation of the correlation.

The simple source distribution of Eq.(53) does not represent the more complex source distribution predicted by BUU calculations (§ 2) and observed experimentally in the energy spectra and angular distributions of bremsstrahlung photons. We therefore considered the existence of two sources, which we assumed as a first guess to be identical in shape but separated in space and time by Δr and Δt respectively:

$$\rho(r,t) = I_d\rho_d(r,t) + I_t\rho_t(r - \Delta r, t - \Delta t), \tag{57}$$

where the $d(t)$ indice refers to direct (thermal). The corresponding correlation function writes:

$$C_{12}(Q) = 1 + \lambda \left|\varrho(Q)\right|^2 \times \left\{I_d^2 + I_t^2 + 2I_dI_t\cos\left(q_0\Delta t - q_z\Delta z\right)\right\}, \tag{58}$$

where we have further assumed that the relative momentum between the two sources is parallel to the beam direction. Eq. (58) is equivalent to Eq. (55) multiplied by a factor due to the interference between two photons stemming each from one of the two sources. The projection on Q is not straight forward and does not lead to a simple analytical form. To avoid the analytical derivation, we have chosen the mathematical solution of generating the photon source distribution and performing the Fourier transform event-by-event.

7.2 BUU simulations of correlation functions

BUU simulations do not directly provide for each *pn* collision a photon with a certain energy, but rather determine a probability distribution. We have thus stored for each ith *pn* collision its position, r_i, and the associated probability distribution $P_1(k)$. We then analyzed the output by constructing, at r_i, plane waves with four-momentum k and calculated for $i \neq j$ the two-photon probability:

$$\begin{aligned} P_2(k_i, k_j) &= P_{i\otimes j} \times |A \exp i\,(k_i r_i + k_j r_j) + B \exp i\,(k_i r_j + k_j r_i)\,|^2 \\ &= P_{i\otimes j} \times \{1 + 2AB \cos\left[q\,(r_i - r_j)\right]\}\,, \end{aligned} \tag{59}$$

where A and B take into account the eventually different probabilities of the direct and cross terms:

$$A = \sqrt{\frac{P_{i\otimes j}}{P_{i\otimes j} + P_{j\otimes i}}} \quad \text{and} \quad B = \sqrt{\frac{P_{j\otimes i}}{P_{i\otimes j} + P_{j\otimes i}}}. \tag{60}$$

$P_{i\otimes j} = P_1(k_i) \times P_1(k_j)$ and $P_{j\otimes i} = P_1(k_j) \times P_1(k_i)$ are the probabilities to produce the pair without correlation. Q is then calculated and its spectrum incremented. Similar calculations were performed elsewhere [67] and compared to our data.

The experimental correlation functions (Fig. 27) for photons having passed the TAPS filter (energy and angular resolution, momentum acceptance and analysis filter) for the two systems Kr+Ni and Ta+Au are compared to the calculations considering two scenarios described below. In the first scenario we have considered photons emitted only during the first 60 and 80 fm/c of the collision for the systems Kr+Ni at $60A$ MeV and Ta+Au and $40A$ MeV, respectively, i.e., we considered only direct photons. The impact parameter was $b = 3$ fm for the first system and $b = 4$ fm for the second. The value of the parameter λ in the correlation function was fixed to be 0.75 to take into account [65] the dipole component established in the angular distribution (§ 6.2.2). We find that the correlation (Fig. 27) is too strong when compared to the data thus indicating that additional factors must be taken into account to reduce it. One way would consist in arbitrarily decreasing the value of λ. It would indeed take on a smaller value if the photon emission is not fully incoherent. Alternatively, taking into account the second photon source will reduce the correlation function as indicated by Eq. (58). This was done by extending the BUU calculations up to 180 and 240 fm/c, respectively, for the two systems, thus including the thermal photons. In this second scenario we obtain a satisfactory description of the data (Fig. 27). These comparisons demonstrate the necessity to take into account the full dynamics of the photon

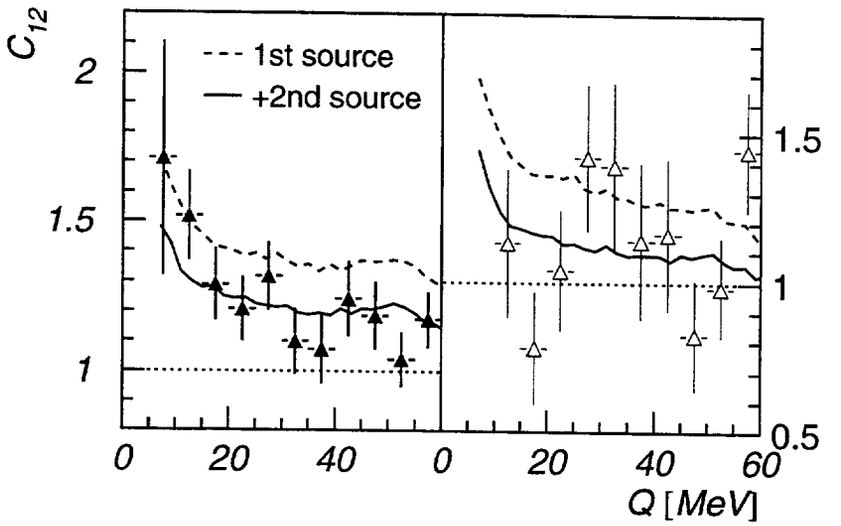

Fig. 27. *Experimental correlation functions compared to BUU calculations. Dashed lines correspond to photons produced during the first t=60 and t=80 fm/c of the collision. Solid lines correspond to photons produced up to t=180 and t=240 fm/c. Left-hand side corresponds to* ^{86}Kr + ^{nat}Ni *at 60A MeV and the right-hand side to* ^{181}Ta + ^{197}Au *at 40A MeV.*

emission calculated by BUU to obtain a correlation function with a strength and width comparable to the experimental one. Nevertheless for the heavier system the calculations do not predict the modulation for which there is an indication in the experimental correlation function. This modulation could be a result of the collision dynamics which is not perfectly treated by BUU after the expansion phase of the system (§ 2). Data with better statistics are needed to unambiguously establish this modulation.

7.3 Monte-Carlo simulations of correlation functions

To study the influence of the full dynamics and to take into account the two-body mechanism observed for heavy systems around the Fermi energy [68] and predicted by BUU (see Fig. 4), we performed additional calculations. The space-time coordinate $r_{1,2}$ of the origin of the photons is sampled via a Monte-Carlo technique according to various source distributions: i) a single source described by Eq. (53), ii) two sources separated in space and time described by Eq. (57), and iii) two sources as previously but with the second one split into two fragments described by ρ_{t1} and ρ_{t2}:

$$\rho(r) = I_d\rho_d(r) + I_t\left\{\rho_{t1}(r - [\Delta z - \Delta z'/2]) + \rho_{t2}(r - [\Delta z + \Delta z'/2])\right\}, \quad (61)$$

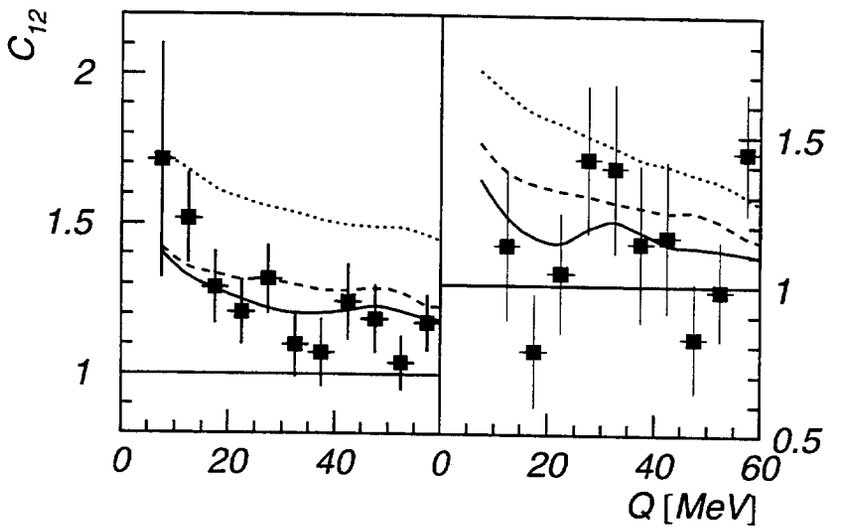

Fig. 28. *Experimental correlation functions compared to calculations based on Monte-Carlo sampling. The different lines correspond to one source, two sources, and two sources of which the second one is fragmented (dotted, dashed and solid respectively). Left-hand side spectrum corresponds to* $^{86}Kr + {}^{nat}Ni$ *at 60A MeV and the right-hand side to* $^{181}Ta + {}^{197}Au$ *at 40A MeV.*

where $\Delta z'$ is the separation between the two fragments. For this last case the thermal source is split in space into two fragments presumably experiencing each the density oscillation at the origin of thermal photons. The two photons are correlated in the same way as previously [Eq. (59)] and the correlation function is projected on Q after passing the photons through the experimental filter.

The two measured correlation functions have been compared to the results of this calculation (Fig. 28) where in Eq.(61) ρ was described by a Gaussian distribution [Eq. (53)] of width R equal to the size of the overlap zone of projectile and target, and of lifetime equal to $\tau = 3R$. The distance between the two sources was taken to be $\Delta z = \beta_{AA}\Delta t$. The separation between fragments $\Delta z'$, the time Δt separating the two sources and the intensity I_d were taken as free parameters. As it was the case for the BUU calculations considering only one photon source, the calculation largely overpredicts the data. By introducing the second source a better agreement is achieved which can be further improved by considering that the second source is fragmented. In addition the calculation assuming fragmentation predicts the experimentally observed modulation in the correlation function of the heavier system.

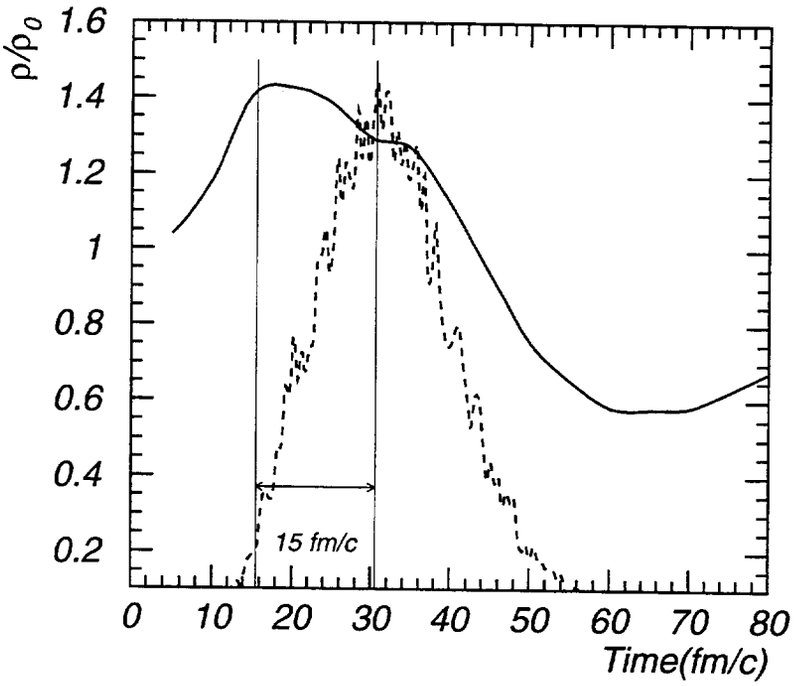

Fig. 29. *Time evolution of the maximum density (solid line) and of the bremsstrahlung photon emission (dashed line) calculated with BUU for the system* $^{86}Kr + {}^{nat}Ni$ *at 60A MeV at b=0 fm.*

8 COLLECTIVE PROPERTIES OF NUCLEAR MATTER

In the light of the BUU calculations, the whole set of data we have collected on hard photons can be consistently interpreted in terms of the emission from two distinct sources emitting at different instants of the heavy-ion collision. The first one is associated with a dense state of nuclear matter, the second one to the thermalizing phase. The relative intensity of the two sources reflects the strength of the density oscillations characteristic of heavy-ion collisions at intermediate energies. We shall now express the collective character of nuclear matter in terms of thermodynamical quantities (see § 2): density, temperature, and incompressibility modulus.

- **Density:**
  Direct bremsstrahlung-photons are emitted during the first compression phase in the heavy-ion reaction. As a matter of fact, according to the calculations, most of these photons are emitted only after the maximum density has been reached (Fig. 29). The delay is long enough so that nucleons can be accelerated by the potential gradient which depends on the density [Eq. (70)] and nucleons acquire extra intrinsic momentum. Since the compression is less important in peripheral collisions than in central ones, the

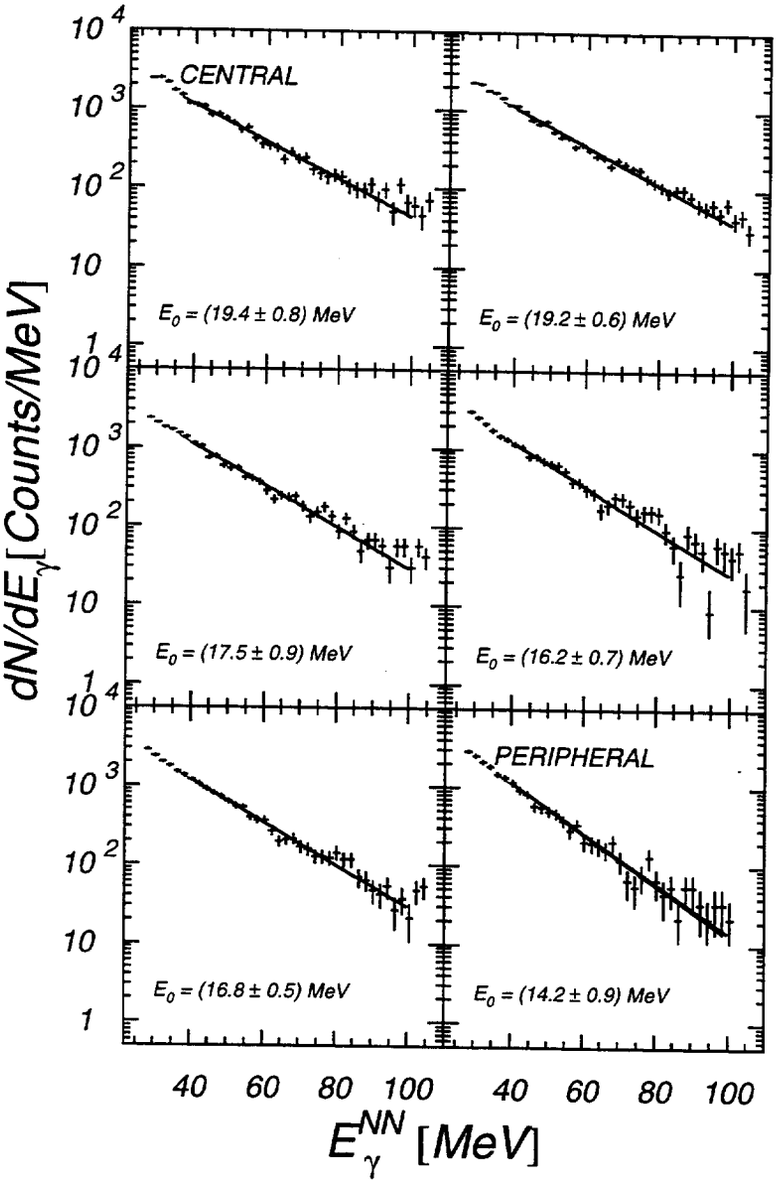

Fig. 30. *Photon spectra measured for the system ^{86}Kr + ^{nat}Ni at 60A MeV for various impact parameters selected from the associated charged particle multiplicity and PLF mass, from central (upper left panel) to peripheral (lower right panel) collisions. The photon energy is calculated in the NN center-of-mass.*

acceleration and thus the extra intrinsic momentum are also less important. Consequently the average energy available in an individual *pn* collision is larger in central than in peripheral collisions. This is reflected in the photon energy and can be visualized in a change of the slope of the spectrum. The hardest spectrum is measured for the most central collisions (Fig. 30).

Using Eq. (4) we calculate the change in the average intrinsic momentum which corresponds also to a change of the slope with the impact parameter. The intrinsic momentum variation is then converted into a density varia-

tion following Eq. (??). This method does not lead to absolute values of the density but to values relative to a reference value which we have selected as the density calculated by BUU at $b = 8$ fm, the largest impact parameter for which the photon slope parameter could be measured. In the resulting variation of the density with decreasing impact parameter (Fig. 31), one observes a sharp and continuous increase when going from peripheral to central collisions until projectile and target overlap by one radius. At

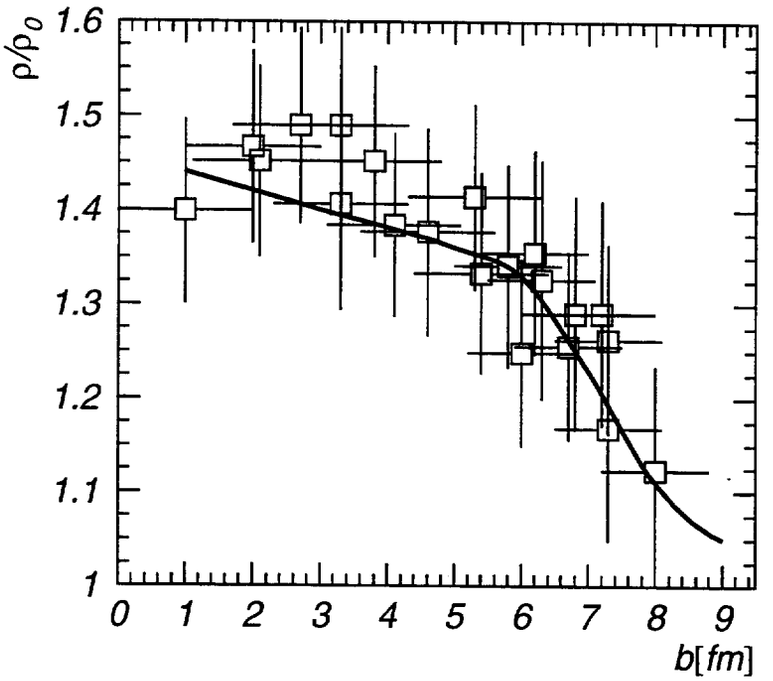

Fig. 31. *Average density reached in the heavy-ion collision* $^{86}Kr + {}^{nat}Ni$ *at 60A MeV calculated from the slope parameters of direct bremsstrahlung-photon spectra measured as a function of impact parameter. The density is normalized to the value calculated with BUU at* $b = 8$ *fm. The solid line represents the maximum density calculated by BUU.*

smaller impact parameters the density only slightly increases to its maximum value of $\rho = 1.5\rho_0$. The experimental trend follows exactly the trend of the maximum density calculated by BUU (Fig. 31).

Although the absolute value of the density deduced from the measured direct bremsstrahlung-photon spectrum relies on the model calculations, the variation with impact parameter is an experimental observation. The only hypothesis thus made is that a change in the slope parameter reflects a change in intrinsic momentum of the colliding nucleons. We therefore consider the experimentally observed impact parameter dependence as additional evidence that the BUU model provides a good description of the collision dynamics at least for the first instance of the collision when direct bremsstrahlung photons are emitted.

System	Impact parameter	Temperature [MeV]	E_{CM} [MeV]
Kr+Ni 60A MeV	inclusive	6.3 ± 1.0	14.4
	$b < 5$ fm	7.5 ± 1.0	
	$b > 5$ fm	5.0 ± 1.5	
Ta+Au 40A MeV	inclusive	5.0 ± 1.0	10.0
Pb+Au 30A MeV	inclusive	3.0 ± 1.0	7.5

Table 11
Temperatures reached in specified heavy-ion collisions and deduced from the slope of thermal bremsstrahlung-photon spectrum and calculations of Fig. 6.

- **Temperature:**
  The interpretation of the data emphasizing that a second source of thermal photons is created can be exploited to deduce from the slope of the thermal-photon spectrum a local temperature of the system (Fig. 6) since the photon emission is short on the reaction time scale. One reaches slightly higher temperatures (Tab. 11) in the system Kr+Ni at 60A MeV than in the system Ta+Au at 40A MeV, 7.0 ± 0.5 MeV compared to 5.5 ± 0.5 MeV and the temperature is very sensitive to the impact parameter. In central collisions ($b < 5$ fm) the system reaches T= 8.0 ± 0.6 MeV and only T= 5.6 ± 0.4 MeV for peripheral collisions.

- **Incompressibility modulus:**
  From the calculations it is found that the relative intensity between the direct and the thermal bremsstrahlung-photons depends strongly on the Equation-of-State of nuclear matter via the incompressibility modulus K_∞ (Fig. 7). Experimentally we found the predicted behavior of the relative intensity with bombarding energy and impact parameter. The corresponding incompressibility modules K_∞ deduced from a comparison between experimental and calculated relative intensities of the two sources are reported in Tab. 12. Taking the average value of the incompressibility modulus deduced in the three systems we find $K_\infty = 290 \pm 50$ MeV. This value fits within the range of values deduced from the energy of the Giant Monopole Resonance [69]. The incompressibility modulus is certainly the most model dependent parameter we have extracted from the hard-photon data and it should therefore be taken with caution. However, it provides a new quantitative information on the Equation-of-State of nuclear matter independently of all other known methods which are all as well model dependent (see for example Ref. [1]).

We can now attempt to evaluate how the longitutinal kinetic energy of the projectile is dissipated. We first can evaluate the energy E_{comp} stored in compres-

System	Relative intensity I_d/I_t	Incompressibility modulus K_∞ [MeV]
Kr+Ni 60A MeV	3.0 ± 0.5	310 ± 50
Ta+Au 40A MeV	2.0 ± 0.6	290 ± 80
Pb+Au 30A MeV	1.6 ± 0.5	270 ± 80

Table 12
Incompressibility modulus deduced from comparison of the experimental relative intensity of direct and thermal bremsstrahlung-photon and of theoretical values predicted by BUU calculations.

sion energy to reach the density of $1.5\rho_0$ measured in the Kr+Ni system. We use the value of the incompressibility modulus and the potential of Eq. (70):

$$E_{\text{comp}} = E(1.5\rho_0) - E(\rho_0), \tag{62}$$

$$E(\rho) = \int_0^\rho \left[\frac{p^2(\rho')}{2M_N} + U(\rho')\right] d\rho'. \tag{63}$$

We find $E_{\text{comp}} = (2.9 \pm 1)A$ MeV.

To evaluate the amount of energy converted into excitation energy E^*, we can construct a caloric curve $E^* = f(T)$ and set:

$$E_{CM} = E_{\text{coll}} + E^*, \tag{64}$$

where E_{CM} is the energy available in the system calculated in the AA center-of-mass and E_{coll} any kind of collective energy including the compression energy. The correlation between the temperature and E_{CM} (Fig. 32) can be described by a $E_{CM} = 3/2T$ dependence (Boltzmann relation) with $E_{\text{coll}} = 3.4A$ MeV rather than by a aT^2 dependence (Fermi liquid relation). The meaning of this correlation remains an open question. Further and detailed investigations are needed, namely by measuring the excitation energy through the complete detection in coincidence with photons of light charged particles and fragments.

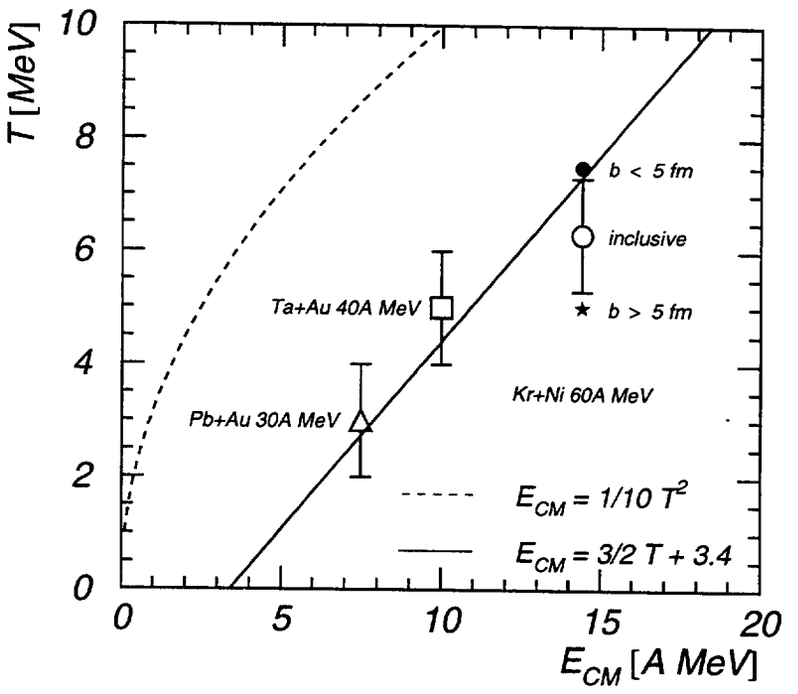

Fig. 32. *Correlation between the temperature deduced from the slope of thermal photons energy spectra and the total energy available in the system and calculated in the AA center-of-mass. The data points for the systems Kr+Ni at 60A MeV, Ta+AU at 40A MeV, and Pb+Au at 30A MeV are reported in Tab. 11. The Fermi liquid relation (dashed line) is plotted with a level density parameter A/10. The Boltzmann relation (solid line) has been fitted to the inclusive data (open symbols) with the offset as a free parameter.*

9 NEUTRAL PIONS

We discuss in this section the production of sub-threshold neutral pions. The π^0 detection requires the coincident registration of the two decay-photons and the identification by invariant mass analysis. For each photon pair identified with the shower reconstruction algorithm, the invariant mass is calculated using Eq. (13).

The experimental π^0 invariant mass distribution (Fig. 26) can be described by:

$$g_{\pi^0}(X) = g(X) + \theta(X - X_0)\exp\left(-\frac{(X - X_0)}{\Gamma}\right)(1 - g(X)), \tag{65}$$
$$g(X) = \exp\left(-\frac{(X - X_0)^2}{2\Delta^2}\right).$$

where the parameters have been fixed from the analysis of the invariant mass spectrum calculated by GEANT, and θ is the step function. Owing to the 9.6% resolution, most of the detected π^0 events are contained in the analysis cut 100 MeV$< M_{\rm inv} <$ 150 MeV. In contrast to measurements performed at energies above the free NN π^0 threshold (280A MeV), the number of π^0's in one event in our experiment is at most unity so that the invariant mass analysis does not generate a combinatorial background by pairing photons from different π^0's. Experimental parameters characterizing the π^0 production measured in the three systems we have studied [70] are summarized in Tab. 13. For the Pb+Au system we can only give an upper limit of the cross section because of the low statistics. The probability to produce a π^0 is calculated following Eq. (27) but by replacing the average number of pn collisions by the average number of NN collisions.

9.1 Energy and momentum distributions

Information on the pion dynamics can be obtained from the total energy and the transverse momentum spectra. The total energy is calculated as:

$$E^2_{\pi^0} = \frac{2M^2_{\pi^0}}{(1 - \cos\theta_{\gamma_1\gamma_2})\left[1 - \left(\frac{E_{\gamma_1} - E_{\gamma_2}}{E_{\gamma_1} + E_{\gamma_2}}\right)^2\right]}. \tag{66}$$

In the π^0 total energy spectrum measured for the Kr+Ni system (Fig. 33), very energetic pions are produced, similarly to the photon spectrum, above the

	system		
parameter	Kr+Ni	Ta+Au	Pb+Au
	60A MeV	40A MeV	30A MeV
σ_R [b]	4.37	7.11	7.21
$\langle N_{NN} \rangle_b$	14.02	37.77	40.50
E_0 [MeV]	17.6 ± 0.9	16 ± 4	-
σ_{π^0} [μb]	42 ± 4	2.2 ± 0.3	< 0.9
$P_{\pi^0}(\times 10^8)$	69 ± 7	0.8 ± 0.1	< 0.14
T_0 [MeV]	15.8 ± 0.2	16 ± 4	-

Table 13
Parameters characterizing the π^0 production.

kinematic limit defined in analogy to Eq. (35). The data are compared to DCM calculations (Fig. 33). In these calculations, pions are produced in inelastic NN collisions (see Appendix) and the primordial pion yield is subsequently modified by both absorption and rescattering processes in the nuclear medium. To compare the calculations with our data, the calculated energy spectra were folded with the TAPS response and geometric acceptance. While for the Ta+Au system the small number of detected pions renders the comparison difficult, we find for the Kr+Ni system that the calculated energy spectrum is softer than the experimental one. As a consequence the calculated cross section, 28 μb, is also smaller than the experimental one. This difference can be explained by the fact that the popular Ver West-Arndt approximation of the pion production cross section [71] used in DCM might fail near the threshold. This is plausible in light of recent measurements [72]. Another possible origin of energetic pions could also be found in three-body collisions and dynamical fluctuations not present in the DCM model.

The transverse momentum, $p_T = p \cos\theta$, is a particularly interesting observable. Since it is Lorentz invariant, it is free of kinematic effects and determined only by the internal characteristics of the pion source. Assuming a source in thermal equilibrium, the transverse momentum should exhibit a Boltzmann distribution with a slope parameter related to an apparent temperature of the source:

$$\frac{d\sigma}{dp_T} \propto p_T \sqrt{m_T} \exp\left(-\frac{m_T}{T_0}\right), \qquad (67)$$
$$m_T = \sqrt{M_{\pi^0}^2 + p_T^2}.$$

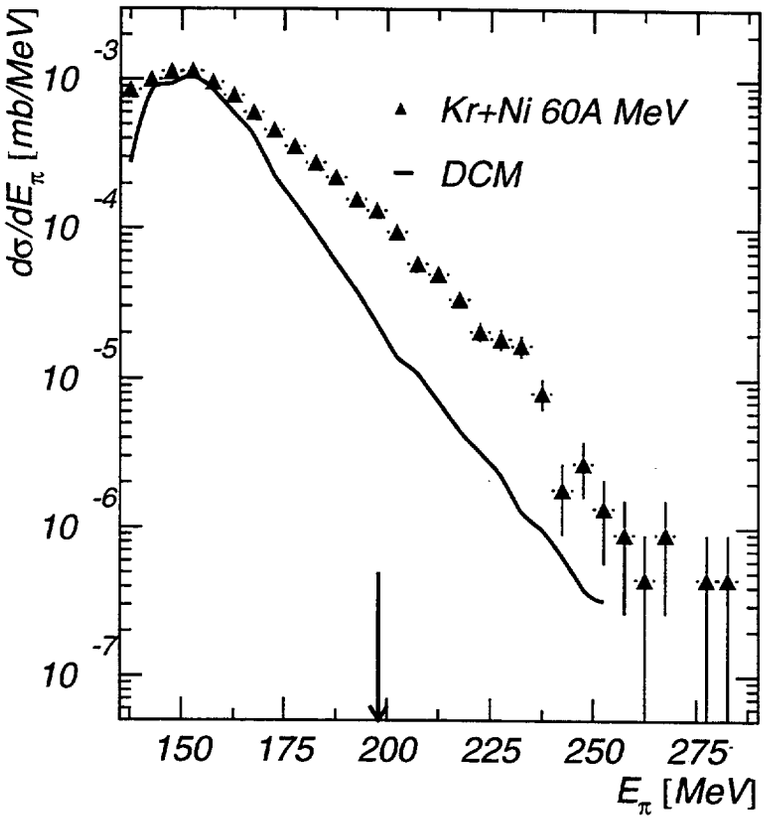

Fig. 33. π^0 *total energy measured for the reaction* $^{86}Kr + {}^{nat}Ni$ *at 60A MeV. The solid line represents a DCM calculation corrected for the detector response and acceptance. The arrow indicates the kinematic limit.*

Fitting Eq. (67) to the data corrected for the detector response and acceptance (Fig. 34) we find an apparent pion temperature $T_0 = 15.8 \pm 0.2$ MeV for the system Kr+Ni and $T_0 = 16 \pm 4$ MeV for the system Ta+Au. In spite of the difference in bombarding energy we find the same temperature for the two systems . We thus confirm the finding of previous measurements [73–75] that the transverse momentum distribution of pions is independent of the bombarding energy as long as its value stays well below the pion creation threshold energy. While the temperature stays almost constant, the pion production probability per participant nucleon increases by a factor 8.5 when the bombarding energy increases from 40 to 60A MeV. This could indicate that the additional translational energy is not used to increase the kinetic energy of the emitted pions but rather to increase the number of pions with no change in their average kinetic energy. In the picture in which pions originate from the decay of the Δ resonance, this would mean that the additional energy available in individual NN collisions with increasing bombarding energy is not converted into heat but rather into mass by exciting nucleons to the Δ resonance.

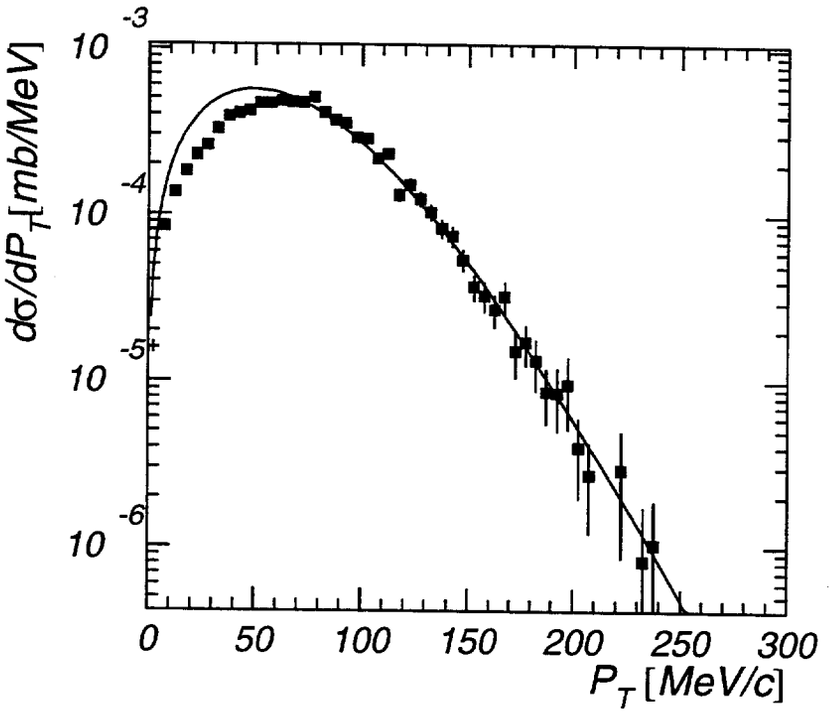

Fig. 34. π^0 *transverse momentum measured in the system* $^{86}Kr + ^{nat}Ni$ *at 60A MeV and corrected for the detector acceptance. The solid line is a fit to the data with Eq. (67).*

There exists a depletion for the π^0 transverse momentum at low transverse momentum when compared to the Boltzmann distribution (Fig. 34). The same effect was observed in other measurements [75,76] and was interpreted in terms of final state interactions of π^0 in nuclear matter. However, absorption can be best observed in rapidity distributions.

9.2 Rapidity distribution

It is advantageous to analyze the shape of the rapidity distribution rather than the angular distribution to get information on both source velocity and location. If pions are emitted from a single moving source, the rapidity will be distributed symmetrically about the source velocity (rapidity). The total rapidity distribution integrated over p_T (Fig. 35) measured for the system Kr+Ni is distributed about a centroid at $\bar{Y} = 0.00 \pm 0.01$. This could indicate that the pion source is nearly at rest in the laboratory frame and clearly slower than the NN center-of-mass system ($Y_{NN} = 0.17$) and the AA center of mass system ($Y_{AA} = 0.21$). The same behavior was observed in previous measurements [73]. However this apparent shift of the rapidity distribution can be explained by pion absorption in nuclear matter. To demonstrate such

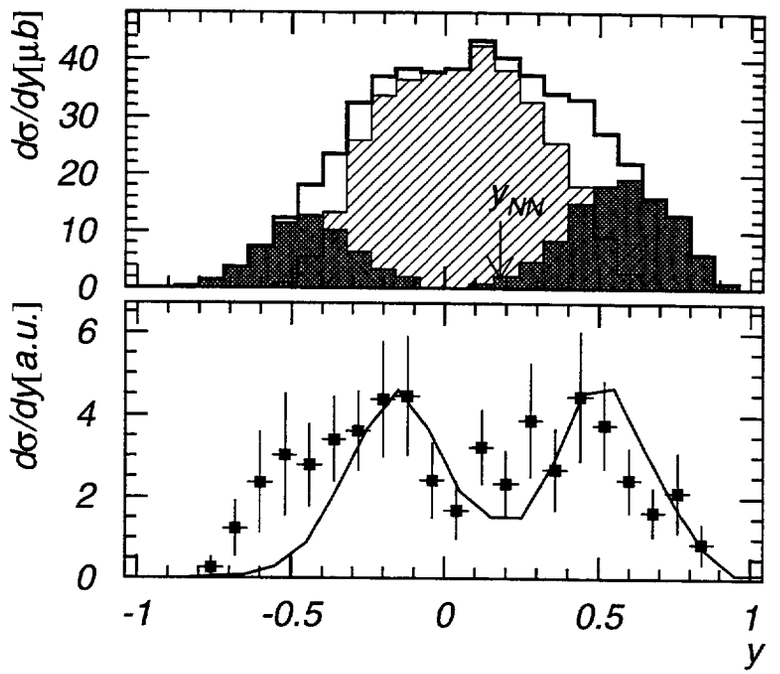

Fig. 35. π^0 *rapidity distributions measured for the reaction* $^{86}Kr + {}^{nat}Ni$ *at 60A MeV. Upper panel: the thick solid line represents the rapidity integrated over* p_T. *The thin solid lines represent pions emitted along the beam direction (dark shaded) and perpendicular to the beam direction (light shaded). Lower panel: data points represent the rapidity distribution for* $p_T \leq 30$ *MeV/c and for central collisions; the solid line represents the corresponding distribution calculated with DCM.*

absorption we have selected pions emitted (i) preferentially along the beam direction ($|p_t/p_{||}| < 1$) and (ii) preferentially perpendicular to the beam direction ($|p_t/p_{||}| > 1$). The corresponding rapidity distributions (Fig. 35) exhibit a forward-backward asymmetry reflecting the asymmetry of the entrance channel. Pions emitted backwards through the Kr projectile are more strongly absorbed than pions emitted forwards through the Ni target. Pions emitted perpendicular to the beam direction do not see this asymmetry as confirmed by the data. From this observation one can conclude that pions are produced in central collisions when projectile and target start to overlap, i.e., only in the early phase of the heavy-ion collision.

The rapidity distribution (Fig. 35) yields more precise information on the origin of the π^0 transverse momentum at low p_T values. A minimum in the rapidity distribution is observed around the NN rapidity. DCM calculations reproduce this distribution. The explanation is straightforward. Since pions with small p_T are selected, pions with the NN rapidity will have a small kinetic energy and thus will be preferably absorbed. The energy dependence of the pion absorption was established in Ref. [75,76].

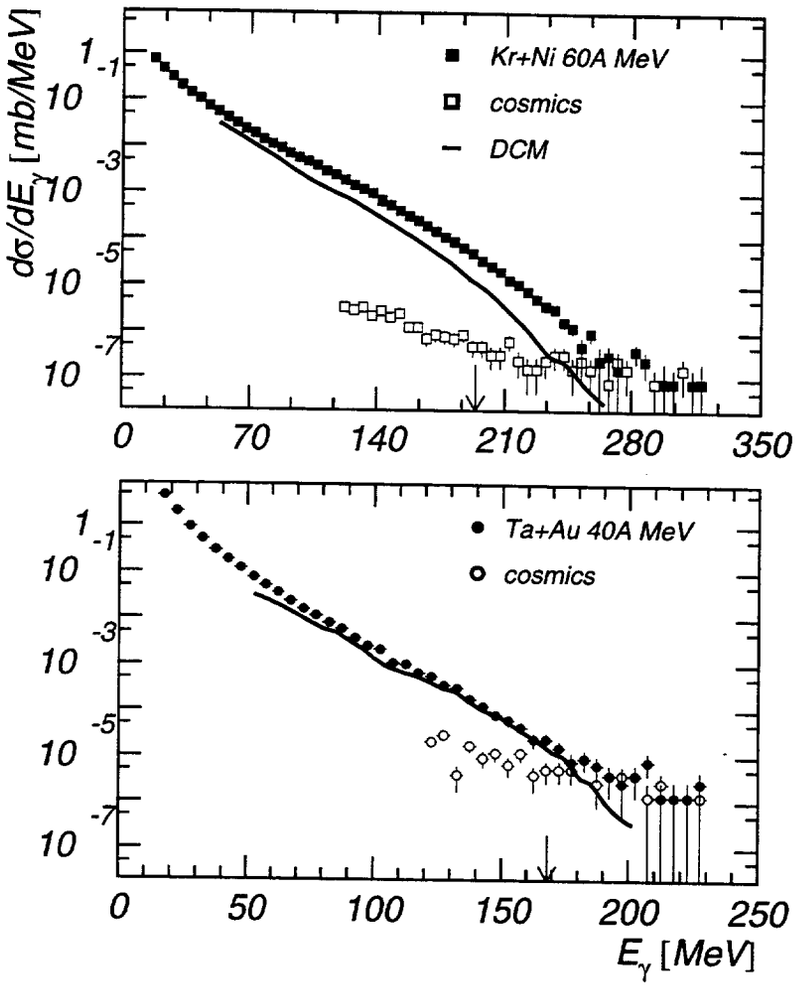

Fig. 36. *Photon spectra measured at* $\theta = 90^0$ *for the reactions* $^{86}Kr + {}^{nat}Ni$ *at 60A MeV (upper panel) and* $^{181}Ta + {}^{nat}Au$ *at 40A MeV (lower panel). The solid lines represent the sum of all known contributions calculated with DCM. The arrow indicates the kinematic limit [Eq. (35)].*

10 VERY ENERGETIC PHOTONS

The commonly used models for the production of hard photons cannot reproduce the most energetic photons (Fig. 36) beyond the kinematic limit [Eq. (35)]. Indeed the *pn* bremsstrahlung spectrum (Fig. 36) calculated either with BUU or DCM stays well below the data at photon energies near and above the kinematic limit where the cross section falls to zero. To overcome the kinematic limit in individual *pn* collisions, nucleons must acquire more intrinsic momentum than available at saturation density: $p_F^{max} = \hbar\,(3\pi^2\rho_0/2)^{1/3}$. Several mechanisms supplying the extra energy may be considered:

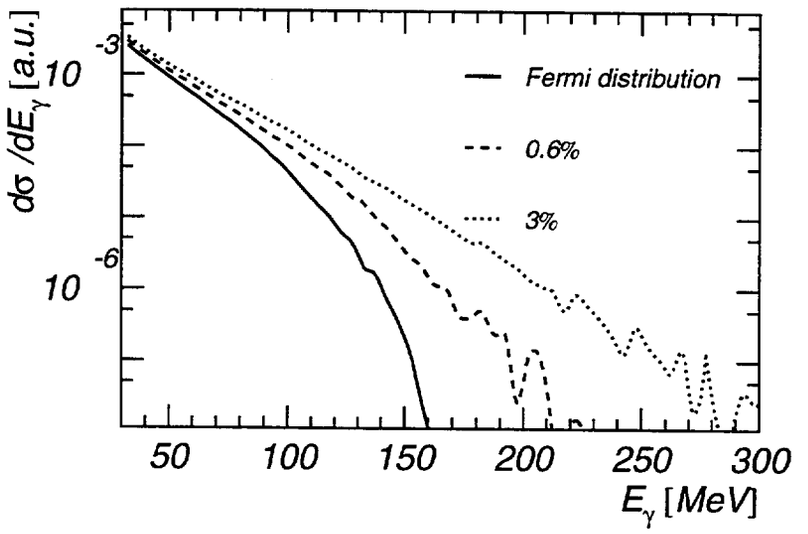

Fig. 37. *Photon spectra calculated assuming intrinsic momentum distributions in the nuclear ground state such that (i) 0.6% of the nucleons have momenta between 300 MeV and 500 MeV/c (dashed line) and (ii) 3% of the nucleons have momenta between the same limits (dotted line). The system considered was* ^{86}Kr + ^{nat}Ni *at 60A MeV.*

- *nucleon off-shell effects*
  During their propagation through nuclear matter nucleons can go off-shell ($E^2 > p^2 + M_N^2$) and collide with other nucleons. Extra energy is thus brought into the system and energetic photons can be produced. These effects can of course not be taken into account by semi-classical calculations as BUU or DCM. They can be mimicked by artificially changing the intrinsic momentum distribution in the nuclear ground state but that would lead to an incorrect description of the collision dynamics. We therefore did not follow this path but calculated the expected photon distribution by folding a given intrinsic momentum distribution with the elementary $pn \rightarrow pn\gamma$ cross section (Fig. 37). We considered two cases. First we assumed that 0.6% of the nucleons have intrinsic momenta between 300 and 500 MeV/c as was recently measured via electron scattering [77] for ^{208}Pb. Within this assumption the calculation still largely underpredicts the data. Second, to get a good description, we considered that 3% of the nucleons have intrinsic momenta within the above defined range in disagreement with the electron scattering data.

- *three-body collisions*
  In the BUU and DCM model calculations the collision integral [Eq. (71)] of the transport equation is approximated by two-body collisions, neglecting higher order collisions. This approximation is certainly not justified when high densities are reached. In such circumstances three-body colli-

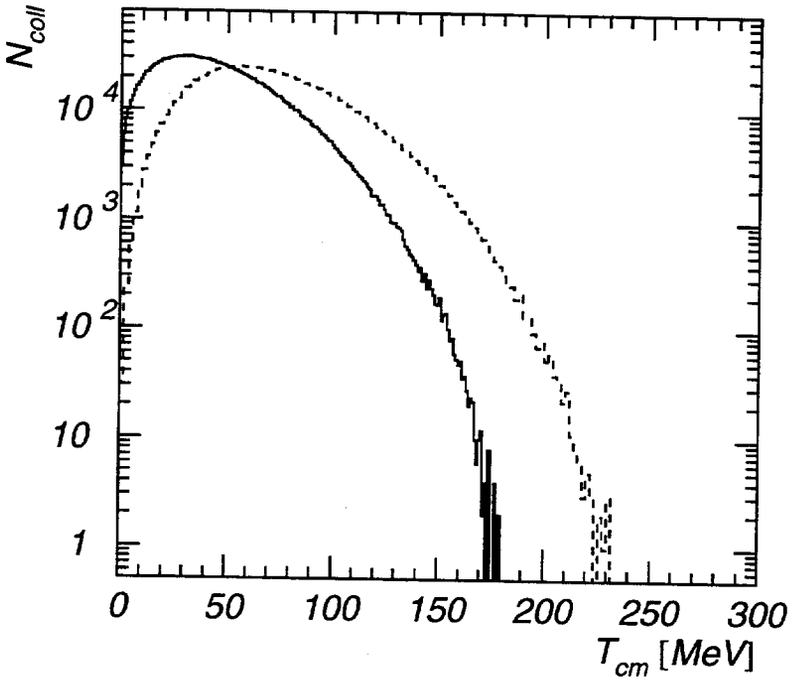

Fig. 38. *Two-body (solid line) and three-body collisions (dashed line) distribution as a function of the energy available in the collisions, calculated for the system* ^{86}Kr + ^{nat}Ni *at 60A MeV.*

sions become important [2]. Additional elementary bremsstrahlung-photon production processes must therefore be considered, among which reactions involving deuteron-like correlated nucleon pairs play the leading role [78]. Presently such mechanisms are to the best of our knowledge not yet systematically included in the collision integral. We have therefore only calculated the energy available in three body collisions occurring during a heavy-ion collision (Fig. 38). Even if all this available energy would be converted into the production of a single photon, it could not explain the experimental spectrum. Again we find that the additional energy brought in by three-body collisions is by far not sufficient to explain the experimental photon spectrum.

- *dynamical fluctuations*
  Dynamical fluctuations are a very general phenomenon occurring in any random medium, e.g., the Brownian motion of molecules. Similarly the random propagation of nucleons through the randomly changing mean field generates stochastic and large fluctuations in the intrinsic momenta. Collisions can thus occur in which nucleons have an unusually large intrinsic momentum. Several approaches have been considered to treat dynamical fluctuations [79–81] but none has dealt with the very energetic photons that we have measured.

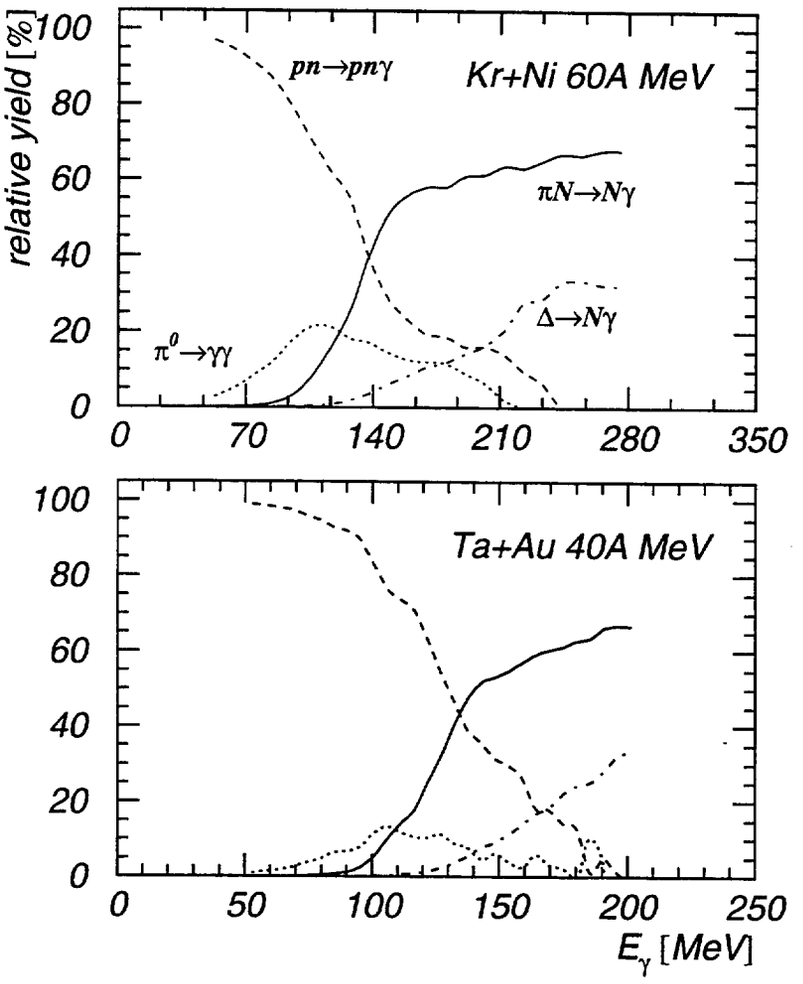

Fig. 39. *Relative intensity distribution of the mechanisms:* $p+n \rightarrow p+n+\gamma$ *(dashed line),* $\pi + N \rightarrow N + \gamma$ *(solid line),* $\pi^0 \rightarrow \gamma\gamma$ *(dotted line) and* $\Delta \rightarrow N\gamma$ *(dot-dashed line) calculated with DCM for the systems* $^{86}Kr + {}^{\text{nat}}Ni$ *at 60A MeV (upper panel) and* $^{181}Ta + {}^{\text{nat}}Au$ *at 40A MeV (lower panel).*

Although bremsstrahlung photons have not yet been calculated including in the heavy-ion dynamics the three effects we have just discussed, it is very unlikely that the experimental hard photon spectrum can be described only by bremsstrahlung photons. We have therefore considered other processes that produce hard photons and which are usually neglected because of their small cross sections. We considered three processes whose relative intensities vary with the photon energy (Fig. 39). Together with the bremsstrahlung the sum of the three additional contributions provides a satisfactory description of the data (Fig. 36).

– $\pi^0 \rightarrow \gamma\gamma$

The energy distribution of photons from the decay of neutral pions has been

determined experimentally and was found similar to the calculated one. The neutral pion decay yields a maximum in the photon spectrum at $M_\pi/2$ which is however significantly lower than the bremsstrahlung contribution. At higher photon energies ($E_\gamma > 150$ MeV) these two contributions come close to each other. The role of π^0 decay as photon source increases rapidly with bombarding energy and already at $E > 100A$ MeV this decay is the main source of hard photons with $E_\gamma > M_\pi/2$.

- $\Delta \rightarrow N\gamma$
  The Δ isobars are exclusively excited in inelastic NN scattering (see appendix). The photon decay occurs with a weak branching of 6×10^{-3}. The calculated distribution (Fig. 39) does not correspond to the shape of the Δ resonance but to the convolution of the shape with the resonance excitation probability. At the bombarding energies under consideration, only the low-energy tail of the resonance is excited, the mass of the resonance at the peak being $M_0 = 1232$ MeV.

- $\pi + N \rightarrow N\gamma$
  The pion absorption off a nucleon followed by emission of a hard photon (radiative capture) is the dominant mechanism for hard photon production above the pion mass and at bombarding energies below $100A$ MeV. The energy spectrum of subthreshold pions is essential for calculations of photons in the extreme high energy tail of the spectrum. For the Kr+Ni system DCM predicts a too soft pion-energy spectrum (Fig. 33) and consequently the calculated photon spectrum falls off too steeply (Fig. 36).

From the analysis of photon spectra above the kinematic limit we found that this part of the spectrum cannot be described in the standard approach based only on incoherent *pn* bremsstrahlung. As suggested by DCM, the radiative capture $\pi + N \rightarrow N + \gamma$ involving pions produced in the nuclear medium dominates the production of very energetic photons. An improved quantitative description of photon production by this additional mechanism however requires a deeper understanding of subthreshold pion production itself as well as of pion dynamics in the nuclear medium.

11 CONCLUSION

The aim of the research program presented here is to establish the Equation-of-State of nuclear matter. We have made some progress in this direction by solving two major problems encountered in this field. The first problem was an experimental one, linked with the difficulty to isolate photons among the overwhelming hadronic radiation generated in heavy-ion collisions. We have succeeded to solve it by exploiting the performance of the TAPS detection system. The second problem, linked with the difficulty to disentangle effects due to nuclear matter properties from collision dynamics effects, has been solved by choosing hard photons as a probe. The data were then analyzed considering collective properties of hot and dense nuclear matter.

The hard-photon emission pattern is characterized by the energy spectrum and angular distribution, and the space-time distribution of the source was extracted from the two-photon interference. All experimental observations converge towards the conclusion that for the systems studied bremsstrahlung photons are not emitted from a single source but from two sources instead with different characteristics. The more intense source produces the harder spectrum and travels with the NN center-of-mass velocity. The second and softer source moves with the center-of-mass velocity of the combined system. The relative intensity of the two sources changes with impact parameter so that more soft photons are produced in central collisions. Finally the source distribution extracted from the two-photon correlation function is compatible with two sources separated in space and time with the possibility that the latter is split into two or more fragments. From these purely experimental observations we conclude that hard photons are emitted at two different instants of the heavy-ion collision: first at the very beginning of the collision in first chance *pn* collisions and second in a later phase of the collision through secondary *pn* collisions.

For comparison with our data BUU calculations were performed for heavy-ion reactions at intermediate bombarding energies. These calculations reveal that at low enough bombarding energies the collision proceeds via density oscillations of a monopole type. Knowing that BUU calculations cannot really be trusted over a too long time, we considered only two of these oscillations no matter how the system evolves later on. During the first oscillation, dense nuclear matter is formed over a volume corresponding to the overlap volume between projectile and target. During the second oscillation, a new dense state is formed but this time the system is thermalizing. The calculations further predict that a bremsstrahlung-photon flash accompanies each oscillation and each flash has exactly the emission pattern established experimentally. We thus identified the two experimentally observed photon sources with the two calculated sources resulting from density oscillations. Based on these experimental

observations we have proposed methods to evaluate density, temperature and incompressibility modulus characteristic of nuclear matter compressed and heated in heavy-ion collisions.

Besides bremsstrahlung photons, the photon spectrum measured for the first time over such a wide dynamical range reveals new aspects. On the low energy side the weak cross section for GDR photon decay suggests that reaction fragments are produced with a broad mass distribution and that a possible quenching sets in at high excitation energies. Having data of better quality in this photon energy range will be extremely attractive since it will provide the means to follow the reaction dynamics from the very beginning probed by bremsstrahlung photons to the last evaporative stage probed by statistical photons.

On the high energy side of the spectrum we found that photons are produced well above the kinematic limit, and that they cannot be interpreted as bremsstrahlung photons even when considering the dynamics of the intrinsic momentum distribution. With the help of DCM (comparable to BUU except for the computation technique which in DCM allows to produce real particles) we found that pion radiative capture is by far the dominant process to produce very energetic photons besides the better known π^0 and Δ decay. This interpretation makes very hard photons a new and interesting probe of pion production and of their propagation through nuclear matter.

Acknowledgement

We thank the members of the technical staff of the Grand Accélérateur National d'Ions Lourds (GANIL) for their help and delivery of high quality beams required for our measurements. This work was in part supported by IN2P3 and CEA (France), FOM (The Netherlands), BMFT and DFG (Germany), the CICYT Research project N0. PB90-091 (Spain) and the European Union HCM Network Contract ERBCHRXCT94066.

12 APPENDIX: MODELS FOR HEAVY-ION COLLISIONS AND PARTICLE PRODUCTION

12.1 Boltzmann transport equation

The semiclassical Boltzmann transport equation describes the time evolution of the one-body phase-space distribution $f(\vec{r},\vec{p},t) \equiv f$. This distribution, describing a nuclear many body ensemble, represents the probability to find a nucleon with momentum $\vec{p}$ at spatial coordinate $\vec{r}$ and at time t. In this formalism, during the evolution of the system nucleons collide with other nucleons while moving through a time dependent mean-field potential. The introduction of the Pauli exclusion principle in the collision term and the Fermi motion of nucleons in the initial state preserve the quantal nature of nucleons inside the nucleus. The Boltzmann equation takes the following form:

$$\frac{d}{dt}f(\vec{r},\vec{p},t) = I\left[f(\vec{r},\vec{p},t)\right]. \tag{68}$$

The left-hand side of Eq. (68) represents the equation of motion for the one-body distribution. It develops as:

$$\frac{d}{dt}f = \left\{\frac{\partial}{\partial t} + \frac{\vec{p}}{m}\frac{\partial}{\partial \vec{r}} - \vec{\nabla}_r U(\vec{r},t)\frac{\partial}{\partial \vec{p}}\right\} f, \tag{69}$$

where $U(\vec{r},t)$ represents the time dependent mean-field potential. A phenomenologic potential can be adopted. According to a Skyrme parameterization depending on the local baryonic density, $\rho(\vec{r})$, this approximated potential reads [82]:

$$U(\vec{r}) = a\rho(\vec{r}) + b\rho(\vec{r})^n + U_{\mathrm{C}}. \tag{70}$$

In this equation U_{C} contains the Coulomb interaction. The momentum dependence of the potential is neglected. The three parameters a, b, n are fixed by the properties of infinite nuclear matter at zero temperature and pressure: the saturation density $\rho_0 = 0.17$ fm^{-3}, the binding energy $E_B = -16$ MeV, and the incompressibility modulus K_∞. The latter will be a free parameter in the calculation. A large value (> 250 MeV) for K_∞ defines a stiff Equation-of-State and a smaller value (< 250 MeV) for this parameter a soft Equation-of-State. The frontier between these two regimes is of course not strictly defined.

The right-hand side of Eq. (68) represents the collision integral which can be approximated by the expression for two-body collisions, $\vec{p} + \vec{p}_1 \rightarrow \vec{p}_2 + \vec{p}_3$, integrated over the available phase space:

$$I[f] \approx I_2[f] = \frac{1}{2m} \int d\vec{p}_1 d\vec{p}_2 d\Omega |\vec{v}| \frac{d\sigma}{d\Omega} \left\{ f_2 f_3 \bar{f} \bar{f}_1 - f f_1 \bar{f}_2 \bar{f}_3 \right\} \delta(\vec{p} + \vec{p}_1 - \vec{p}_2 - \vec{p}_3) \delta(E + E_1 - E_2 - E_3). \quad (71)$$

In Eq. (71) the collision rate $|\vec{v}| d\sigma/d\Omega$ is integrated over all the available phase space. The δ-functions ensure energy and momentum conservation in the NN collision. The factor in curled brackets contains the *loss* and *gain* terms weighted by factors describing the Pauli exclusion principle. These factors are obtained from the probability that there is no nucleon with momentum $\vec{p}_i$ at spatial coordinate $\vec{r}$ and at time t, i.e., $\bar{f}_i \equiv 1 - f_i$. The differential NN cross-section, $d\sigma/d\Omega$, is taken from the experimental free NN cross section as an approximation to the unknown in-medium NN cross section. Alternatively the parameterization proposed by J. Cugnon [83] can be used.

12.2 BUU model

Several varieties of the transport equation labeled with names like for the most popular ones Boltzmann-Uehling-Ulenbeck (BUU) [4], Landau-Vlasov (LV) [84], Boltzmann-Nordheim-Vlasov (BNV) [2] have been developped. Among the different varieties the recipe to solve the equation might also change. Obviously Eq. (68) cannot be solved analytically. A numerical solution is derived instead applying the test-particle technique [85]. The continuous one-body distribution $f(\vec{r}, \vec{p}, t)$ is discretized by associating to each of the $A = A_t + A_p$ nucleons $\mathcal{N}$ elementary functions, commonly called test or pseudo particles:

$$f(\vec{r}, \vec{p}, t) = \frac{1}{\mathcal{N}} \sum_{i=1}^{\mathcal{N}A} \delta\left(\vec{r} - \vec{r}_i(t)\right) \delta\left(\vec{p} - \vec{p}_i(t)\right). \quad (72)$$

Within this form f_i is a solution of the equation of motion (left-hand side of Eq. (68)) if each test particle with momentum $\vec{p}_i$ and at location $\vec{r}_i$ is a solution of the classical Hamilton equations:

$$\frac{d\vec{p}_i}{dt} = -\vec{\nabla}_r U(\vec{r}_i, t), \quad \frac{d\vec{r}_i}{dt} = \frac{1}{m} \vec{p}_i. \quad (73)$$

With the introduction of test particles, the nuclear system is approximated by a classical ensemble with a finite number of particles and $\mathcal{N}$ parallel ensembles. A technical remark must be added here. The original symmetry in the entrance channel might be lost during the collision. This is an artifact of the numerical method based on a finite number of parallel ensembles (100 test particles per nucleon were used for our calculations). It does not lead to the numerical convergence of the Boltzmann-equation solution. Increasing this number would lead to a better convergence and restore the symmetry [2]. However using only

a limited number of test particles is a technique which can be used to study statistical fluctuations in the collision dynamics.

For the initial conditions the system must be prepared in its ground state, $E_B = -16$ MeV and $\rho_0 = 0.17$ fm^{-3}. Therefore test particles are randomly distributed in configuration space according to a Woods-Saxon distribution [4] which gives the correct value for the binding energy. The test-particle momentum is also chosen randomly according to a uniform distribution between 0 and the local Fermi momentum, $p_F(r) = \hbar(3/2\pi^2\rho(r))^{1/3}$, where $\rho(r)$ is the local density.

The temporal evolution of the system is performed by discretizing the time in steps of typically $\delta t = 0.5$ fm/c. At each time step the solution of the Hamilton equations [Eq. (73)] are:

$$\vec{p}_i(t+\delta t) = \vec{p}_i(t) - \vec{\nabla}_r U(\vec{r}_i, t)\delta t, \tag{74}$$

$$\vec{r}_i(t+\delta t) = \vec{r}_i(t) + \frac{1}{m}\vec{p}_i(t)\delta t. \tag{75}$$

The local density $\rho(\vec{r}_i)$ is calculated as the ensemble average over a volume of typically 1 fm^3:

$$\rho(\vec{r}_i, t) = \int_{\Omega} f(\vec{r}, \vec{p}_i, t)d\vec{r}, \tag{76}$$

where $f(\vec{r}_i, \vec{p}_i, t)$ is given by Eq. (72). The local potential appearing in Eq. (74) is then calculated using Eq. (70). To achieve a better numerical convergence, Gaussian test particles [85] are preferred to the point test particles of Eq. (72). Although the two representations are approximately equivalent, the latter one has the advantage that less test particles per nucleon are needed which as a consequence reduces the computation time.

Finally the collision term of the transport equation is evaluated by calculating at $t+\delta t/2$ the distance between all test particles belonging to a same ensemble. By definition a collision occurs when the impact parameter is smaller than $b_{\max} = \sqrt{\sigma_{NN}/\pi}$. Scattering kinematics are then calculated following Eq. (71) and the blocking factors $\bar{f}$ are computed as ensemble average values. A uniform random number is then compared to $\bar{f}_i\bar{f}_j$ to decide if the collision is allowed.

Because of the ensemble averaging technique, this method to solve the Boltzmann equation only provides average quantities. This approach is somewhat inconvenient, especially in the case of rare events, like deep-subthreshold particle (DSP) production. They cannot be calculated with a reasonable number of test particles and therefore a reasonable amount of computation time. This

limitation of the Boltzmann equation can be overcome by developing more sophisticated models which can provide more than an average behavior. Two directions are presently pursued. The first one considers the classical molecular dynamics extended to include the quantum features of heavy-ion collisions [86,87]. The second approach is based on stochastic methods in which an average dissipative pattern is introduced on the one-body distribution f through the collision integral. The transport equation transforms then into the Boltzmann-Langevin equation. To our knowledge none of these two approaches have yet systematically included photon and particle production. Only an attempt has been made [79] to calculate the deep-subthreshold production of kaons.

12.3 Dubna-Cascade-Model DCM

To calculate DSP production we have adopted the intra-nuclear cascade model to simulate the heavy-ion collision dynamics. This model was developed by the Dubna group [13,10]. The Dubna Cascade Model (DCM) is also based on the Boltzmann equation [Eq. (68)] with the difference that the mean field temporal evolution is treated in a simplified way. The scalar nuclear potential of the initial state is kept constant during the collision and only the potential depth is changed according to the number of knock-out nucleons. This *frozen* mean field approximation should not bias too much the DSP production since they are mainly produced during the early stage of the collision. Since the exact mean field does not need to be recalculated at each time step as it is done in the BUU model, it is not necessary anymore to resort to the test-particle technique. The DCM model therefore regards the collisions as full ensembles in contrast to the BUU models which regards the collisions as parallel ensembles.

The ground state of the initial system is prepared as in BUU by calculating the intrinsic momentum distribution and the parameters of the Woods-Saxon distribution are extracted from electron-nucleus elastic scattering data [88].

The collision between nucleons is treated in a similar way as in BUU. Since DCM does not resort to the test-particle technique which gives access as we have seen only to the average properties of the heavy-ion collision dynamics, the dynamics of each NN collision can be followed. Consequently also very weak channels, like the production of very energetic photon or DSP can be calculated. But as soon as the dynamics of the mean field prevail, DCM is not relevant anymore.

The spectrum of energetic photons emitted in a heavy-ion collision is calculated as the incoherent superposition of bremsstrahlung produced in individual NN collisions:

$$\frac{d\sigma_\gamma}{d\vec{k}} = 2\pi \int_0^{b_{\max}} bdb \sum_{NN} \int \frac{d\Omega'}{4\pi} \frac{k}{k'} \frac{dP_\gamma^{NN}(\sqrt{s})}{d\vec{k}'} \bar{f}_2 \bar{f}_3. \tag{77}$$

In Eq. (77), k is the photon energy Doppler shifted to the frame moving with the NN center-of-mass velocity, the factor k/k' the Jacobian of the Lorentz transformation, and Ω' the phase space available in the final state of the collision $\vec{p} + \vec{p}_1 \rightarrow \vec{p}_2 + \vec{p}_3 + \vec{k}$ weighted by the Pauli blocking factor $\bar{f}_2 \bar{f}_3$. The final photon spectrum is obtained by integrating the photon production probability over the available phase-space, then by summing over all NN collisions and finally by taking the average over the impact parameter b. In Eq. (77) $dP_\gamma^{NN}(\sqrt{s})/dk'$ represents the probability to produce a photon with center-of-mass energy k' in a NN collision in which the available energy is $\sqrt{s}$. The value for this cross section is again not known when the NN collision occurs in the nuclear medium. Therefore as a first guess the known value from free NN collisions is adopted. However, since data are scarce specially in the intermediate energy domain, the photon production is calculated instead. Indeed only *pn* collisions will be considered since the intensity of bremsstrahlung emitted in proton-proton collisions is, because of its quadrupole character, strongly reduced with respect to the dipole radiation emitted in *pn* collisions. In a quantal description of the photon production, the cross-section is calculated as [89]:

$$\frac{dP_\gamma}{dk d\Omega_\gamma d\Omega_q} = \frac{M_N^4}{4|\vec{p}_p|(2\pi)^5 E_p} \cdot \frac{k|\vec{q}|^2 |T_\gamma|^2}{2\left[E_n'(q - k\cos\theta) + E_p'(q - k\cos\theta)\right)\right]}, \tag{78}$$

where E_p, E_p', and E_n' are the initial and final energies of the proton and the final energy of the neutron, $\vec{q}$ is the relative momentum between the proton and the neutron, and $|T_\gamma|$ is the transition amplitude, calculated from the One Boson Exchange amplitude [90]. In the NN scattering, photons are produced through external bremsstrahlung by the in- and out-going proton as well as through internal bremsstrahlung in the exchange of charged mesons. While solving numerically the Boltzmann equation, each time two nucleons collide the spectrum of Eq. (78) is evaluated and the result is put into Eq. (77). In doing so the photon production is treated perturbatively, i.e., photons do not participate to the dynamics of the collision. This approximation is justified by the weak production probability of a photon in a single NN collision; of

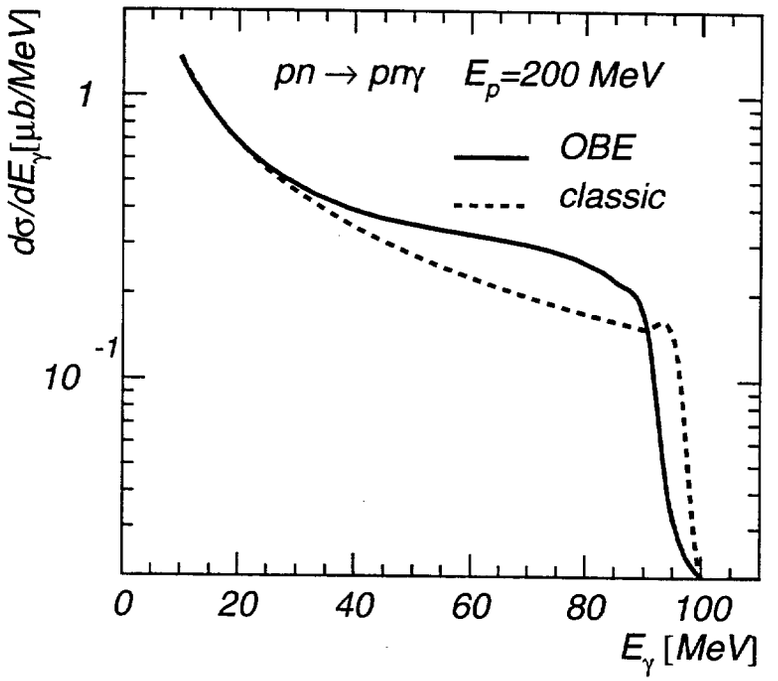

Fig. 40. *Bremsstrahlung photon spectrum calculated for a pn collision at 200 MeV using the Schäfer parameterization [90] and using classical electrodynamics.*

the order of 10^{-4} at $100A$ MeV, it decreases for lower bombarding energies (Fig. 41).

The photon spectrum of Eq. (78) is very similar to the classical bremsstrahlung radiation emitted by an accelerating charge (Fig. 40). It has a $1/k$ dependence and drops abruptly to zero at a maximum photon energy equal to the energy available in the NN center-of-mass system, i.e., approximately half the projectile kinetic energy. As illustrated by the calculated photon spectrum for a *pn* collision at 200 MeV (Fig. 40), the cross section goes, as expected, to zero for photons with energy close to 100 MeV when the available energy in the NN center-of-mass is exhausted. The evolution of this cross section is represented (Fig. 41) by the photon production probability [90] as a function of the Coulomb corrected beam energy, $E_{cc} = E_L - V_c/A_p$, where E_L is the kinetic energy per nucleon of the projectile, V_c the Coulomb barrier and A_p the mass number of the projectile. A minimum photon energy of 30 MeV is required, which implies the existence of a 60 MeV threshold on the beam energy below which photons with energy larger than 30 MeV cannot be produced. The situation is radically different when the *pn* collision occurs in the nuclear medium during heavy-ion collisions, as illustrated by the bremsstrahlung photon production probability scaled by the number of participants and calculated for the heavy-ion collision ^{40}Ca+^{40}Ca at $b = 0$ (Fig. 41). The number of participants is calculated as the number of *pn* pairs present in the geometric overlap

between projectile and target (see Sec. 5). The photon production probability at a given bombarding energy is much larger than what is expected from the calculation for a free NN collision. Moreover the probability remains large even at the $60A$ MeV threshold and down to bombarding energy as low as $20A$ MeV. At $60A$ MeV bombarding energy for example, bremsstrahlung photons with energy above 30 MeV can thus be considered as subthreshold photons. Both BUU and DCM calculations give similar results. The strong deviation from the free NN case evidences the major role played by the intrinsic momentum due to the Fermi motion ($E_F \sim 40$ MeV) of nucleons in the nucleus. This coupling provides the additional energy needed to overcome the threshold. The energy of the subthreshold photon, which can be best studied at beam energies per nucleon close to the Fermi energy, thus reflects the intrinsic momentum of colliding nucleons, and the photon spectrum can be viewed as an image of the phase-space occupancy of participating nucleons. In that sense the bremsstrahlung-photon production acts as a collective probe (the Fermi motion is a mean-field effect) of nuclear matter (the participant zone) and of its dynamics.

12.5 Inelastic NN collisions in DCM

Only pions, the lightest mesons, will be considered since the bombarding energies under consideration in this article are already well below the threshold of 280 MeV at which pions are produced in free NN collisions. Therefore in heavy-ion collisions at, for example, $50A$ MeV the pion production probability is only of the order of 10^{-8} per NN collision. As emphasized, such weak channels cannot be studied with the BUU model within reasonable computation time (except if fluctuations are considered [79]). To the contrary the DCM approach allows to investigate the collisions in an event-by-event mode with much less computation time. Therefore weak NN inelastic channels can be simulated and the dynamics of produced particles followed. Pions in DCM are produced either directly via $N + N \rightarrow N + N + \pi$, or in two steps through the Δ resonance formation and decay: $N + N \rightarrow \Delta + N$ and $\Delta \rightarrow N + \pi$. For in-medium inelastic cross section, the experimental free cross section modified by the Pauli blocking is adopted. The formation of the Δ isobars is calculated so that the effective mass of the πN system follows the Δ mass, M, distribution:

$$F(M, \sqrt{s}) = \frac{\Gamma(p)}{(M - M_0)^2 + \frac{1}{4}\Gamma^2(p)} \theta\left(\sqrt{s} - M - M_N\right), \tag{79}$$

where $M_0 = 1232$ MeV is the mass at the peak of the resonance, M_N the nucleon mass and $\sqrt{s}$ the NN center-of-mass energy. The θ function ensures energy conservation.The momentum dependent width, $\Gamma(p)$, is parametrized

as [82]:

$$\Gamma(p) = \frac{0.47p^3}{\left[1 + 0.6\frac{p^2}{M_\pi^2}\right] M_\pi^2}, \tag{80}$$

where p is the center-of-mass momentum in the $N\Delta$ channel. We checked that the calculated π spectra and the Δ production reproduce closely the experimental data for free NN collisions [91].

The production of π and Δ gives rise to an additional source of photons. Neutral pions decay before they reach the detector and emit two correlated photons with a branching ratio of 99%. Δ isobars decay through the emission of one photon, the branching ratio being 0.6%. These two sources of photons contribute to the total photon spectrum in an energy range depending on the beam energy.

The yields of primordial pions and Δ's are subsequently modified by absorption and rescattering processes in nuclear matter. Pions can be absorbed either in two-step processes: $\pi + N \rightarrow \Delta$ and $\Delta + N \rightarrow N + N$, or directly by nucleons or correlated nucleons, $(NN)_c$, in the processes: $\pi + N \rightarrow N + \gamma$ and $\pi + (NN)_c \rightarrow N + N$. The modified treatment of the inverse channel for short-lived resonances [92] is used to estimate the isospin averaged cross section of the $\Delta + N \rightarrow N + N$ process:

$$\sigma_{\Delta+N\rightarrow N+N} = \frac{1}{8}\frac{Mp^2}{p'^2}\sigma_{N+N\rightarrow N+\Delta} \Big/ \int_{(M_N+M_\pi)^2}^{(\sqrt{s}-M_N)^2} \frac{1}{2\pi} M'' F(M'') p'' dM'', \tag{81}$$

where p' is the center-of-mass momentum in the NN channel, and $F(M'')$ represents the Δ mass distribution [Eq. (79)]. The probability of the pion absorption on a correlated $(\mathrm{NN})_c$ pair was derived from the inverse cross section for the reaction $p + p \rightarrow d + \pi^+$. This cross section could be enhanced by a factor 3 in the nuclear medium [93]. However the probability to find a deuteron-like pair has a relative weight of about 1/4 [94]. Since these two factors are not precisely known and have the tendency to cancel each other, the free cross section for the pion absorption [95] is used instead.

Pions can also be absorbed in the process $\pi + N \rightarrow N + \gamma$. The cross section for this process is calculated using the detailed balance principle:

$$\sigma_{\pi+N\rightarrow N+\gamma} = \frac{1}{8}\frac{p^2}{p'^2}\sigma_{N+\gamma\rightarrow N+\pi}, \tag{82}$$

and the Lorentzian parametrization of Prakash et al. [96]:

$$\sigma_{N+\gamma\to N+\pi} = 0.4\frac{(300E_\gamma)^2}{(300E_\gamma)^2 + \left(E_\gamma^2 - (2.1M_\pi + 30)^2\right)^2} \text{ mb.} \tag{83}$$

To avoid double counting, the Δ-isobars γ-decay in the intermediate state of the reaction $\pi + N \to N + \gamma$ is ignored since it is included implicitly in the inverse reaction parameterization.

For higher bombarding energies the production of heavier mesons can be calculated in this model similarly to pions and by considering the proper inelastic channels.

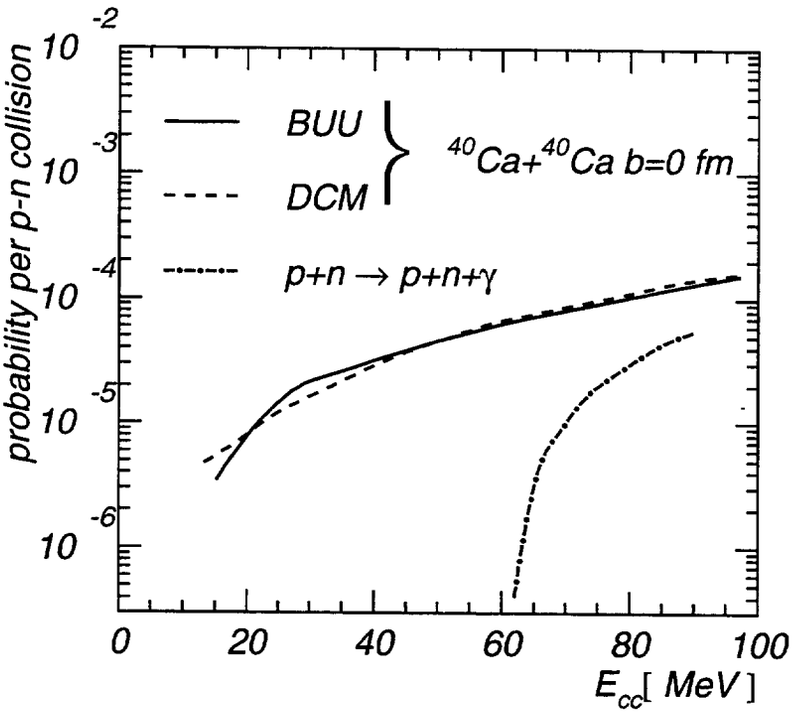

Fig. 41. *Photon ($E_\gamma > 30$ MeV) production probability per pn collision as a function of the bombarding energy per nucleon corrected for the Coulomb barrier. The solid (dashed) line represents the BUU (DCM) prediction calculated in the heavy-ion collisions $^{40}Ca+^{40}Ca$ at b=0. The dotted-dashed line is a calculation for a free pn collision following Eq. (78).*

References

[1] E. Suraud in *Gamma Ray and Particle Production in Heavy Ion Reactions*, Proc. II TAPS Workshop, Guardamar, Spain (1993), eds. J. Díaz, G. Martínez and Y. Schutz, World Scientific Publ. Co., 187 (1994).

[2] A. Bonasera, F. Gulminelli, J. Molitoris, Phys. Rep. **243**, (1994) 1, and references therein.

[3] H. Nifenecker and J.A. Pinston, Prog. Part. Nucl. Phys. **23** (1989) 71.

[4] W. Cassing, V. Metag, U. Mosel and K. Niita, Phys. Rep. **188** (1990) 364.

[5] H. Ströher, Nucl. Phys. News International **6** (1996) 7.

[6] F.M. Marqués, J. Díaz, M. Franke, S. Hlaváč, R. Holzmann, P. Lautridou, F. Lefèvre, H. Löhner, A. Marín, G. Martínez, T. Matulewicz, W. Mittig, R.W. Ostendorf, J.H.G. van Pol, J. Québert, P. Roussel-Chomaz, Y. Schutz, A. Schubert, R.H. Siemssen, R.S. Simon, Z. Sujkowski, V. Wagner, and H.W. Wilschut, Phys. Rev. Lett. **73** (1994) 34.

[7] G. Martínez, J. Díaz, M. Franke, S. Hlaváč, R. Holzmann, P. Lautridou, F. Lefèvre, H. Löhner, A. Marín, F.M. Marqués, T. Matulewicż, W. Mittig, R.W. Ostendorf, J.H.G. van Pol, J. Québert, P. Roussel-Chomaz, Y. Schutz, A. Schubert, R.H. Siemssen, R.S. Simon, Z. Sujkowski, V. Wagner, and H.W. Wilschut, Phys. Lett. **B334** (1994) 23.

[8] G. Martínez, F.M. Marqués, Y. Schutz, J. Díaz, M. Franke, S. Hlaváč, R. Holzmann, P. Lautridou, F. Lefèvre, H. Löhner, A. Marín, T. Matulewicz, W. Mittig, R.W. Ostendorf, J.H.G. van Pol, J. Québert, P. Roussel-Chomaz, A. Schubert, R.H. Siemssen, R.S. Simon, Z. Sujkowski, V. Wagner, H.W. Wilschut, and Gy. Wolf, Phys. Lett. **B349** (1995) 23.

[9] F.M. Marqués, G. Martínez, Y. Schutz, J. Díaz, M. Franke, S. Hlaváč, R. Holzmann, P. Lautridou, F. Lefèvre, H. Löhner, A. Marín, T. Matulewicz, W. Mittig, R.W. Ostendorf, J.H.G. van Pol, J. Québert, P. Roussel-Chomaz, A. Schubert, R.H. Siemssen, R.S. Simon, Z. Sujkowski, V. Wagner, H.W. Wilschut, and Gy. Wolf, Phys. Lett. **B349** (1995) 30.

[10] K.K. Gudima, T. Matulewicz, H. Delagrange, F.M. Marqués, G. Martínez, R.W. Ostendorf, P. Bożek, M. Płoszajczak, Y. Schutz, V.D. Toneev,, J. Diaz, A. Marín, S. Hlaváč, R. Holzmann, A. Schubert, R.S. Simon, V. Wagner, H. Löhner, J.H.G. van Pol, R.H. Siemssen, and H.W. Wilschut, Phys. Rev. Lett. **76** (1996) 2412.

[11] F.M. Marqués, G. Martínez, T. Matulewicz, R.W. Ostendorf, and Y. Schutz, Phys. Rev. **C54** (1996) 2783.

[12] F.M. Marqués, G. Martínez, T. Matulewicz, R.W. Ostendorf, and Y. Schutz, Phys. Lett., in press.

[13] V.D. Toneev and K.K. Gudima, Nucl. Phys. **A400** (1983) 173c.

[14] Gy. Wolf, G. Batko, W. Cassing, U. Mosel, K. Niita, and M. Schäfer, Nucl. Phys. **A517** (1990) 615.

[15] Gy. Wolf, W. Cassing, and U. Mosel, Nucl. Phys. **A552**, (1993) 549.

[16] G. Martínez, *Dépendance de la production de photons durs avec le paramètre d'impact dans les collisions entre ions lourds aux énergies intermédiaires*, Thèse Université de Valencia (Spain), GANIL T94-06.

[17] A. Bonasera, G.F. Burgio, F. Gulminelli, and H.H. Wolter, Nuovo Cimento **A103** (1990) 309.

[18] D. Neuhauser and S.E. Koonin, Nucl. Phys. **A462**, (1987) 163.

[19] R. Novotny, IEEE Trans. Nucl. Sc. **38-2** (1991) 379.

[20] H.K.W. Leegte, E.E. Koldenhof, A.L. Boonstra, and H.W. Wilschut, Nucl. Inst. and Meth. **A313** (1992) 26.

[21] L. Bianchi, B. Fernandez, J. Gastebois, A. Gillibert, W. Mittig, and J. Barrette, Nucl. Inst. and Meth. **A276** (1989) 509.

[22] F.M. Marqués, F. Lefèvre, G. Martínez, T. Matulewicz, R. Ostendorf, and Y. Schutz, Nucl. Inst. and Meth. **A365** (1995) 392.

[23] A. Raschke, *Entwicklung eines Vetodetektors für den Photonendetektor TAPS*, Diplomarbeit, Universität Münster (Germany), 1992.

[24] F.M. Marqués *Estudio y desarrollo del detector CPV para experimentos en GANIL con el multidetector de fotones TAPS*, Tesis de licenciatura, Universitat de València (Spain), 1992.

[25] H.G. Essel, J. Hoffman, and D. Schall *GOOSY data acquisition and analysis system* GSI Scientific Report 1991.

[26] F. Lefèvre, *Développements logiciels autour du multidétecteur TAPS: gestion en ligne des données au GANIL; reconnaissance de mésons neutres à l'aide des réseaux connexionistes*, Thèse, Université de Caen (France), 1993, GANIL T 93-01.

[27] R. Brun, O. Couet, C.E. Vandoni, P. Zanarini in *New computing techniques in physics research* p. 219, edited by Editions du CNRS, Paris, 1990.

[28] F.M. Marqués, A. Marín, G. Martínez, T. Matulewicz, R.W. Ostendorf, and Y. Schutz, Nouvelles du GANIL **57** (1996) 11.

[29] from PANTECHNIK SA, 4, rue Alfred Kastler, 14000 Caen, France.

[30] L.B. Venema *The study of hadron dynamics in relativistic heavy ion collisions* Doctoraat Proefschrift, Rijksuniversiteit Groningen (The Netherlands), 1994.

[31] S. Kubota, M. Suzuki, J. Ruan, F. Shiraishi, and Y. Takami, Nucl. Inst. and Meth. **A242** (1986) 265.

[32] R. Averbeck, *Untersuchungen zur Spektroskopie positiv geladener Pionen mit Bariumfluorid-Detektoren*, Diplomarbeit, Universität Münster (Germany), 1992.

[33] T. Matulewicz, Nucl. Inst. and Meth. **A325** (1993) 365.

[34] GEANT3 user's guide Technical Report.

[35] T.C. Awes, F.E. Obenshain, F. Plasil, S. Saini, S.P. Sorensen, and G.R. Young, Nucl. Inst. and Meth. **311** (1992) 130.

[36] T. Matulewicz in *Gamma Ray and Particle Production in Heavy Ion Reactions*, Proc. II TAPS Workshop, Guardamar, Spain (1993), eds. J. Díaz, G. Martínez and Y. Schutz, World Scientific Publ. Co., 559 (1994).

[37] S. Riess, G. Enders, A. Hoffmann, W. Kühn, V. Metag, R. Novotny, W. Mittig, Y. Schutz, A.C.C. Villari, H. Emling, H. Grein, E. Grosse, W. Henning, R. Holzmann, R. Kulessa, and T. Matulewicz, Phys. Rev. Lett. **69** (1992) 1504.

[38] H. Nifenecker and J.P. Bondorf, Nucl. Phys. **A442** (1985) 478.

[39] M. Kwato Njock, M. Maurel, E. Monnand, H. Nifenecker, P. Perrin, J.A. Pinston, F. Schussler, and Y. Schutz, Nucl. Phys. **A489** (1988) 368.

[40] L.G. Sobotka, L. Gallamore, A. Chbihi, D.G. Sarantites, D.W. Stracener, W. Bauer, D.R. Bowman, N. Carlin, R.T. DeSouza, C.K. Gelbke, W.G. Wong, J.R. Beene, M.L. Halbert, and M. Thoennessen, Phys. Rev. **C44** (1991) 2257 & Phys. Rev. **C46** (1992) 819E.

[41] T. Reposeur, J. Clayton, W. Benenson, M. Cronqvist, S. Hannuschke, S. Howden, J. Karn, D. Krofcheck, A. Nadasen, C. Ogilvie, R. Pfaff, J.D. Stevenson, A. Vander Molen, G.D. Westfall, K. Wilson, J.S. Winfield, B. Young, M.F. Mohar, and J.D. Morissey, Phys. Lett. **B276** (1992) 418.

[42] E. Migneco, C. Agodi, G. Bellia, R. Coniglione, A. Del Zoppo, P. Finocchiaro, C. Maiolino, P. Piattelli, G. Russo, P. Sapienza, A. Badalá, R. Barbera, A. Palmeri, G.S. Pappalardo, F. Riggi, A.C. Russo, A. Peghaire, and A. Bonasera, Phys. Lett. **B298** (1993) 46.

[43] G. Martínez, F. Ballester, J. Díaz, J.L. Ferrero, A. Marín, F.M. Marqués, Y. Schutz, and J.P. Wieleczko, Nouvelles du GANIL **44** (1993) 43.

[44] H.J. Hofmann, J.C. Bacelar, M.N. Harakeh, T.D. Poelhekken, and A. van der Woude, Nucl. Phys. **A571** (1994) 301.

[45] F. Pühlhofer, Nucl. Phys. **A280** (1977) 267.

[46] R. Hingmann, W. Kühn, V. Metag, R. Muhlhans, R. Novotny, A. Ruckelshausen, W. Cassing, H. Emling, R. Kulessa, H.J. Wollersheim, B. Haas, J.P. Vivien, A. Boullay, H. Delagrange, H. Doubre, C. Grégoire, and Y. Schutz, Phys. Rev. Lett. **58** (1987) 59.

[47] T. Suomijärvi, Y. Blumenfeld, P. Piatelli, J.H. Le Faou, C. Agodi, N. Alamanos, R. Alba, F. Auger, G. Bellia, Ph. Chomaz, R. Coniglione, A. Del Zoppo, P. Finocchiaro, N. Frascaria, J.J. Gaardhoje, J.P. Garron, A. Gillibert, M. Lamehi-Rachti, R. Liguori-Neto, C. Maiolino, E. Migneco, G. Russo, J.C. Roynette, D. Santonocito, P. Sapienza, J.A. Scarpaci, and A. Smerzi, Phys. Rev. **C53** (1996) 53.

[48] J. Stevenson, K.B. Beard, W. Benenson, J. Clayton, E. Kashy, A. Lampis, D.J. Morrissey, M. Samuel, R.J. Smith, C.L. Tam, and J.S. Winfield, Phys. Rev. Lett. **57** (1986) 555.

[49] S.J. Luke, R. Vandenbosch, W. Benenson, J. Clayton, K. Joh, D. Krofcheck, T.K. Murakami, and J.D. Stevenson, Phys. Rev. **C47** (1993) 1211.

[50] J. Randrup and R. Vandenbosch, Nucl. Phys. **A490** (1988) 418.

[51] R. Bertholet, M. Kwato Njock, M. Maurel, E. Monnand, H. Nifenecker, P. Perrin, J.A. Pinston, F. Schussler, D. Barneoud, C. Guet and Y. Schutz, Nucl. Phys. **A474** (1987) 541.

[52] J.H.G. van Pol, H.W. Wilschut, H. Löhner, R.H. Siemssen, P. Lautridou, F. Lefèvre, F.M. Marqués, T. Matulewicz, W. Mittig, R.W. Ostendorf, P. Roussel-Chomaz, Y. Schutz, S. Hlaváč, R. Holzmann, A. Schubert, R.S. Simon, V. Wagner, M. Franke, W. Kühn, M. Notheisen, R. Novotny, F. Ballester, J. Díaz, A. Marín, G. Martínez, and A. Kugler, Phys. Rev. Lett. **76** (1996) 1425.

[53] J.H.G. van Pol, *Dissipation mechanisms studied with nuclear bremsstrahlung*, Doctoraat Proefschrift, Rijksuniversiteit Groningen (The Netherlands), 1995.

[54] A. Schubert, R. Holzmann, S. Hlaváč, R. Kulessa, W. Niebur, R.S. Simon, P. Lautridou, F. Lefèvre, F.M. Marqués, T. Matulewicz, W. Mittig, R.W. Ostendorf, P. Roussel-Chomaz, Y. Schutz, H. Löhner, J.H.G. van Pol, R.H. Siemssen, H.W. Wilschut, F. Ballester, J. Díaz, A. Marín, G. Martínez, V. Metag, R. Novotny, V. Wagner, and J. Québert, Phys. Rev. Lett. **72** (1994) 1608.

[55] R. Hanbury-Brown and R. Q. Twiss, Philos. Mag. **45** (1954) 663.

[56] M. Gyulassy, S.K. Kauffman, and L.W. Wilson, Phys. Rev. **C20** (1979) 2267.

[57] D. H. Boal, C.K. Gelbke, B.K. Jennings, Rev. Mod. Phys. **62** (1990) 553.

[58] B. Lörstad, Int. J. Mod. Phys. **A4** (1989) 2861.

[59] Y. Schutz, Acta Physica Polonica **B25** (1994) 485.

[60] F.M. Marqués, G. Martínez, T. Matulewicz, R. Ostendorf and Y. Schutz, Phys. Rep. in press.

[61] G.I. Kopylov, Phys. Lett. **B50** (1974) 472.

[62] W.A. Zajc, J.A. Bistirlich, R.R. Bossingham, H.R. Bowman, C.W. Clawson, K.M. Crowe, K.A. Frankel, J.G. Ingersoll, J.M. Kurck, C.J. Martoff, D.L. Murphy, J.O. Rasmussen, J.P. Sullivan, and E. Yoo, Phys. Rev. **C29** (1984) 2173.

[63] R.W. Ostendorf, *Interférométrie de photons durs dans les collisions entre ions lourds*, Thèse de l'Université de Caen, GANIL T 94 02.

[64] D. Neuhauser, Phys. Lett. **B182** (1986) 478.

[65] L.V. Razumov and R.M. Weiner, Phys. Lett. **B319** (1993) 431.

[66] Y. Akiba, D. Beavis, P. Beery, H.C. Britt, B. Budick, C. Chasman, Z. Chen, C.Y. Chi, Y.Y. Chu, V. Cianciolo, B.A. Cole, J.B. Costales, H.J. Crawford, J.B. Cumming, R. Debbe, J. Engelage, S.Y. Fung, M. Gonin, S. Gushue, H. Hamagaki, O. Hansen, R.S. Hayano, D. Hayashi, S. Homma, H. Kaneko, J. Kang, S. Kaufman, W.L. Kehoe, K. Kurita, R.J. Ledoux, M.J. Levine, Y. Miake, D.P. Morrison, R.J. Morse, B. Moskowitz, D. Nagamiya, M.N. Namboodiri, T.K. Nayak, J. Olness, C.G. Parsons, L.P. Remsberg, D. Roehrich, P. Rotschild, H. Sakurai, T.C. Sangster, R. Seto, R. Soltz, P. Stankus, S.G. Steadman, G.S.F. Stephans, T. Sung, Y. Tanaka, M.J. Tannenbaum, J. Thomas, S. Tonse, J.H. Van Dijk, F. Videbaek, O. Vossnack, V. Vutsadakis, F.Q. Wang, Y. Wang, H.E. Wegner, D.S. Woodruff, Y.D. Wu, X. Yang, D. Zachary, and W.A. Zajc, Phys. Rev. Lett. **70** (1993) 1057.

[67] H.W. Barz, B. Kämpfer, Gy. Wolf, and W. Bauer, Phys. Rev. **C53** (1996) R553.

[68] J.F. Lecolley, L. Stuggé, M. Aboufirassi, A. Badala, B. Bilwes, R. Bougault, R. Brou, F. Cosmo, J. Colin, D. Durand, J. Galin, A. Genoux-Lubain, D. Guerreau, D. Horn, D. Jacquet, J.L. Laville, F. Lefebvres, C. Le Brun, J. Lemière, O. Lopez, M. Louvel, M. Mahi, M. Morjean, C. Paulot, A. Péghaire, N. Prot, G. Rudolf, F. Scheibling, J.C. Steckmeyer, B. Tamain, and S. Tomasevic, Phys. Lett. **B325** (1994) 317.

[69] J. Blocki, J. Skalski, Z. Sujkowski, and W.J. Swiatecki, Acta Phys. Pol. **B27** (1996) 555.
S. Schlomo and D.H. Youngblood, Nucl. Phys. **A569** (1994) 303c.

[70] F.M. Marqués, *Corrélations Bose-Einstein entre photons durs produits dans les collisions d'ions lourds*, Thèse Université de Valencia (Spain), GANIL T94-05.

[71] B.J. Ver West and R.A. Arndt, Phys. Rev. **C25** (1982) 1979.

[72] W.W. Doehnick, S.A. Dytman, J.G. Hardie, W.K. Brooks, and R.W. Flammang, Phys. Rev. Lett. **74** (1995) 2913.

[73] J. Stachel, P. Braun-Munziger, R.H. Freifelder, P. Paul, S. Sen, P. DeYoung, P.H. Zhang, T.C. Awes, F.E. Obenshain, F. Plasil, G.R. Young, R. Fox, and R. Ronningen, Phys. Rev. **C33** (1986) 33.

[74] T. Suzuki, M. Fukuda, T. Ichihara, N. Inabe, T. Kubo, T. Nagawa, K. Yoshida, I. Tanihata, T. Koboyashi, T. Suda, S. Schimona, and M. Fujiwara, Phys. Lett. **B257** (1991) 27.

[75] R. S. Mayer, W. Henning, R. Holzmann, R.S. Simon, H. Delagrange, F. Lefèvre, T. Matulewicz, R. Merrouch, W. Mittig, R.W. Ostendorf, Y. Schutz, F.D. Berg, W. Kühn, V. Metag, R. Novotny, M. Pfeiffer, A.L. Boonstra, H. Löhner, L.B. Venema, H.W. Wilschut, D. Ardouin, H. Dabrowski, B. Erazmus, C. Lebrun, L. Sézac, F. Ballester, E. Casal, J. Díaz, J.L. Ferrero, F.M. Marqués, G. Martínez, H. Nifenecker, B. Fornal, L. Freindl and Z. Sujkowski, Phys. Rev. Lett. **70** (1993) 904.

[76] R. Holzmann, A. Schubert, S. Hlaváč, R. Kulessa, W. Niebur, R.S. Simon, P. Lautridou, F. Lefèvre, F.M. Marqués, T. Matulewicz, W. Mittig, R.W. Ostendorf, P. Roussel-Chomaz, Y. Schutz, H. Löhner, J.H.G. van Pol, R.H. Siemssen, H.W. Wilschut, F. Ballester, J. Díaz, A. Marín, G. Martínez, V. Metag, R. Novotny, V. Wagner, and J. Québert, Phys. Lett. **B366** (1996) 63.

[77] I. Bobeldijk, M. Bouwhuis, D.G. Ireland, C.W. de Jager, E. Jans, N. de Jong, W-J. Kasdorp, J. Konijn, L. Lapikás, J.J. va Leeuwe, R.L.J. van der Meer, G.J.L. Nooren, E. Passchier, M. Schroevers, G. van der Steenhoven, J.J.M. Steijger, J.A.P. Theunissen, M.A. van Uden, H. de Vries, R. de Vries, and P.K.A. de Witt Huberts, Phys. Rev. Lett. **73** (1994) 2684.

[78] P. Bożek, P. Danielewicz, K.K. Gudima, and M. Płoszajczak, *private communication*, to be published.

[79] M. Belkacem, E. Suraud, and S. Ayik, Phys. Rev. **C47** (1993) R16.

[80] K. Niita, in *II IN2P3-Riken Symposium pn Heavy-Ion Collisions*, Obernai, France (1990), eds. B. Heusch and M. Ishihara, World Scientific Publ. Co., 342 (1990).

[81] P. Bożek and M. Płoszajczak, in *Gamma Ray and Particle Production in Heavy Ion Reactions*, Proc. II TAPS Workshop, Guardamar, Spain (1993), eds. J. Díaz, G. Martínez and Y. Schutz, World Scientific Publ. Co., 559 (1994).

[82] G.F. Bertsch and S. Das Gupta, Phys. Rep. **160** (1988) 189.

[83] J. Cugnon, T. Mizutani, J. Meulen, Nucl. Phys. **A352** (1981) 505.

[84] P. Schuck, R. Hasse, J. Jaenicke, C. Grégoire, B. Remaud, F. Sebille, and E. Suraud, Progr. Part. Nucl. Phys. **22** (1990) 181.

[85] C.Y. Wong Phys. Rev. **C25** (1982) 1460.
C. Grégoire, B. Remaud, F. Sebille, L. Vinet, and Y. Raffray, Nucl. Phys. **A465** (1987) 317.

[86] J. Aichelin, Phys. Rep. **202** (1991) 233.

[87] H. Feldmeier, Nucl. Phys. **A515** (1990) 147.

[88] S. Frullani and J. Moguey, Adv. Nucl. Phys. **14** (1985) 1.

[89] C. Izykson and J.B. Zuber *Quantum field theory*, New York, Mc Graw Hill (1985).

[90] M. Schäfer, T.S. Biro, W. Cassing, U. Mosel, H. Nifenecker, and J.A. Pinston, Z. Phys. **A339** (1991) 391.

[91] V.D. Toneev in *Gamma Ray and Particle Production in Heavy Ion Reactions*, Proc. II TAPS Workshop, Guardamar, Spain (1993), eds. J. Díaz, G. Martínez and Y. Schutz, World Scientific Publ. Co., 350 (1994).

[92] P. Danielewicz and G.F. Bertsch, Nucl. Phys. **A533** (1991) 712.

[93] J. Hüfner, Phys. Rep. **C21** (1975) 1.

[94] I.N. Mishutin, L.M. Satarov, J.A. Mahrun, H. Stöcker and W. Greiner, Phys. Rev. **C51** (1995) 2099.

[95] B.G. Ritchie, Phys. Rev. **C28** (1983) 926.

[96] M. Prakash, P. Braun-Munzinger, J. Stachel, and N. Alamanos, Phys. Rev. **C37** (1988) 1959.